UNIVERSIDADE DO VALE DO PARAÍBA
INSTITUTO DE PESQUISA E DESENVOLVIMENTO

MIRIAN MICHELLE MACHADO DE PAULA

FIBROUS PCL COMPOSITES WITH NANOCERAMICS PRODUCED BY ELECTROSPINNING AND ROTARY JET SPINNING FOR REGENERATIVE BONE APPLICATIONS

COMPÓSITOS FIBROSOS DE PCL COM NANOCERÂMICAS PRODUZIDAS POR ELETROFIAÇÃO E ROTOFIAÇÃO PARA APLICAÇÕES ÓSSEO REGENERATIVA

São José dos Campos, SP
2020

MIRIAN MICHELLE MACHADO DE PAULA

FIBROUS PCL COMPOSITES WITH NANOCERAMICS PRODUCED BY ELECTROSPINNING AND ROTARY JET SPINNING FOR REGENERATIVE BONE APPLICATIONS

A thesis submitted in fulfillment of the requirements for the degree of Doctor of in Biomedical Engineering in the Research & Development Institute of the Universidade do Vale do Paraíba (Univap).

Supervisor: Prof. Dr. Anderson de Oliveira Lobo

São José dos Campos, SP
2020

Fundação Valeparaibana de Ensino

BIBLIOTECA

TERMO DE AUTORIZAÇÃO DE DIVULGAÇÃO DA OBRA

Ficha catalográfica

Paula, Mirian Michelle Machado de

Fibrous PCL composites with nanoceramics produced by electrospinning and rotary jet spinning for regenerative bone applications / Mirian Michelle Machado de Paula; orientador, Anderson de Oliveira Lobo. - São José dos Campos, SP, 2020.

1 CD-ROM, 112 p.

Tese (Doutorado) - Universidade do Vale do Paraíba, São José dos Campos. Programa de Pós-Graduação em Engenharia Biomédica.

Inclui referências

1. Engenharia Biomédica. 2. Electrospinning. 3. Polycaprolactone fibers. 4. Nanohydroxyapatite. 5. Carbon nanotubes. I. Lobo, Anderson de Oliveira, orient. II. Universidade do Vale do Paraíba. Programa de Pós-Graduação em Engenharia Biomédica. III. Título.

Eu, Mirian Michelle Machado de Paula, autor(a) da obra acima referenciada:

Autorizo a divulgação total ou parcial da obra impressa, digital ou fixada em outro tipo de mídia, bem como, a sua reprodução total ou parcial, devendo o usuário da reprodução atribuir os créditos ao autor da obra, citando a fonte.

Declaro, para todos os fins e efeitos de direito, que o Trabalho foi elaborado respeitando os princípios da moral e da ética e não violou qualquer direito de propriedade intelectual sob pena de responder civil, criminal, ética e profissionalmente por meus atos.

São José dos Campos, 24 de Setembro de 2020.

Mirian M M de Paula

Autor(a) da Obra

Data da defesa: 24 / 08 / 2020

Universidade do Vale do Paraíba

Instituto de Pesquisa e Desenvolvimento

MIRIAN MICHELLE MACHADO DE PAULA

"COMPÓSITOS FIBROSOS DE PCL COM NANOCERÂMICAS PRODUZIDAS POR ELETROFIAÇÃO E ROTOFIAÇÃO PARA APLICAÇÕES ÓSSEO REGENERATIVA."

Tese aprovada como requisito parcial à obtenção do grau de Doutor, do Programa de Pós-Graduação em Engenharia Biomédica, do Instituto de Pesquisa e Desenvolvimento da Universidade do Vale do Paraíba – Univap, pela seguinte banca examinadora:

PROF.ª DR.ª JULIANA FERREIRA STRIXINO _____

PROF. DR. ANDERSON DE OLIVEIRA LOBO _____

PROF.ª DR.ª LÚCIA VIEIRA _____

PROF. DR. MARCUS ALEXANDRE FINZI CORAT - Unicamp _____

PROF.ª DR.ª LUANA MAROTTA REIS VASCONCELLOS - UNESP _____

Prof.ª Dr.ª Lúcia Vieira

Diretora do IP&D – Univap

São José dos Campos, 24 de agosto de 2020.

To God, my husband, son, parents, and brothers.

ACKNOWLEDGMENT

First, I thank God for guiding me and giving me the strength to move forward with my dreams and not be discouraged by the difficulties.

For being my strength and always supporting me and not letting me give up, I thank and dedicate this work to my husband, Guilherme. Thank you for the beautiful 14 years we shared, I love you and admire you very much. Thank you for making my world better.

To my son Guilherme who came to enlighten my life and allowed me to know the most beautiful way to love.

I thank my parents, Eliete and Pedro Machado, for their trust, support, and above all, for their love; thank you for the dedication in all the moments of my life, everything I am I owe to them, and to whom I lack words to describe such admiration and love.

To my brothers Milene and Pedro and my heart sister Brenda who supported me and helped me to grow, always believing in me, I love you.

To my advisor, Professor Dr. Anderson de Oliveria Lobo, for his invaluable guidance, support, and encouragement, which has provided lessons that I will take for my entire life, thank you very much.

To Professor Dr. Marcus Corat, who has been there since the beginning of my career, thank you for the teachings, attention, motivation, and dedication, which will be very important for my entire life. Thank you.

I want to thank Professor Thomas Webster for having me in his laboratory and supporting my research, in which he contributed a lot to my research.

Professor Dra. Luana Vasconcelos for the contribution of my work for all the teaching, attention, and dedication. My eternal admiration and thanks.

To the professors who contributed my work, Professor Dra. Fernanda Marciano, Professor Dr. Cristina Pacheco, and Professor Marcelo Lancellotti thank you very much!

For the friendships formed over my Ph.D., I would like to thank all my friends. From the University of Vale do Paraíba, especially to Geisa, Fernanda, Tatiane, Maíra, Ritchele, Patrícia, and Tereza, for their help, support, and good times, mainly for the laughs, thank you so much for making my work more fun. From the University

of Campinas, I also thank you for your support and friendship, Josélia, Robson, Mayara, Natalia, and Bruno, thank you very much. From Northeastern University, I thank everyone immensely for their receptivity and help, especially to Paria, James, Gujie, Nicole, Brian, Sidhi, Jazmin, and Okosi for companionship, for the moments of distraction, for the laughter, thank you for being my family for a year.

I want to thank the other professors and Univap employees for their attention and support, Prof Lucia, Prof Sandra, Priscila, Diogo, Maria Alice, Prof. Leandro, and everyone else. Thank you very much.

To São Paulo Research Foundation (Fapesp) (Process number: 2014/16295-2), and Coordination for the Improvement of Higher Education Personnel (CAPES: 88887.116351 / 2016-00) for the scholarships.

I thank everyone who believed in my potential and who contributed to the realization of this work.

“Let us strive for the impossible.
The great achievements throughout history have been
the conquest of what seemed the impossible.”
(Charles Chaplin)

“It was the time you spent with your rose
that made it so important”
(Antononie de Saint-Exupery, The little Prince)

FIBROUS PCL COMPOSITES WITH NANOCERAMICS PRODUCED BY ELECTROSPINNING AND ROTARY JET SPINNING FOR REGENERATIVE BONE APPLICATIONS

ABSTRACT

In clinical practice, bone tissue defects repair remains a significant challenge due to the limitations found in current treatments for bone tissue replacement or repair. Synthetic biomaterials are being explored as a promising alternative to overcome such limitations. New strategies based on well-defined combinations between osteoconductive materials, support, and populations of osteogenic cells are seen as an approach to improve bone regeneration. Here, the efficacy of polycaprolactone (PCL) fibers with carbon nanotube (CNT) and hydroxyapatite (nHap) nanoparticles, using two different methods for fabrication: electrospinning (ES) and rotary jet spinning (RJS), were investigated. Besides, bone marrow mesenchymal stem cells (BMMSCs) were seeded on the scaffolds and implanted in a critical bone defect in the calvary of rats to assess their potential in the bone repair process, compared to acellular scaffolds. Different morphologies were determined through the manufacturing method used. RJS fibers presented a particular topography (rough fibers) compared to ES fibers (smooth fibers). We show that the PCL scaffolds produced by RJS can decrease the colonization of bacteria, which may be related to physical (scaffold morphology) and or biological (bacterial surface) mechanisms. Subsequently, several parameters were analyzed for the scaffolds after the incorporation of the nanoparticles. PCL fibers with nHap:CNT nanoceramics showed the potential to stimulate biological activity in osteoblast cells compared to neat PCL. We also showed that increased bone formation occurred through the combination of three characteristics: the presence of nHap:CNT nanoparticles, rough surface evidenced by the RJS fibers, and scaffolds seeded with BMMSCs. In this study, we show that the choice of biomaterial and surface topography combined with cells of interest are key factors that can favor bone repair.

Keywords: Electrospinning. Rotary jet spinning. Polycaprolactone fibers. Nanohydroxyapatite. Carbon nanotubes. Bone marrow mesenchymal stem cells. Bone repair.

COMPÓSITOS FIBROSOS DE PCL COM NANOCERÂMICAS PRODUZIDAS POR ELETROFIAÇÃO E ROTOFIAÇÃO PARA APLICAÇÕES ÓSSEO REGENERATIVA

RESUMO

Na prática clínica, o reparo de defeitos do tecido ósseo continua sendo um desafio significativo devido às limitações encontradas nos tratamentos atuais para substituição ou reparo de tecido ósseo. Biomateriais sintéticos estão sendo explorados como uma alternativa promissora para suprir tais limitações. Novas estrategias baseadas em combinações bem deliniadas entre materias osteocondutores, suporte e populações de células osteogênicas são vistos como uma abordagem para melhorar a regeneração óssea. Aqui, a eficácia de fibras de policaprolactona (PCL) com nanotubo de carbono (CNT) e nanopartículas de hidroxiapatita (nHap) incorporadas, usando dois métodos diferentes de fabricação: eletrofiação (ES) e rotofiação (RJS), foram investigadas. Além disso, células-tronco mesenquimais da medula ossea (BMMSCs) foram semadas sobre os scaffolds e implantadas em defeito ósseo crítico na calvária de ratos para avaliar seu potencial no processo de reparo ósseo, em comparação com scaffolds acelulares. Diferentes morfologias foram determinadas através do método de fabricação utilizada. Fibras rotofiadas apresentaram uma topografia especial (fibras rugosas) em comparação com fibras eletrofiadas (fibras lisas). Mostramos que os scaffolds de PCL produzidos pela RJS tem um potencial em diminuir a colonização de bactérias, no qual pode estar relacionado a mecanismos físicos (morfologia dos scaffolds) e/ou biológicos (superfície bacteriana). Posteriormente, vários parâmetros foram analisados após a incorporacao das nanoparticulas nos scaffolds. As fibras de PCL com nanoparticulas de nHap:CNT mostraram um potencial em estimular atividade biológica em células de osteoblasto comparado com o PCL puro. Além disso, evidenciamos que aumento da formação óssea ocorreu através da combinação de três características: presença de nanoparticulas de nHap:CNT, superfície rugosa evidenciada pelas fibras RJS e revestimento dos scaffols com BMMSCs. Neste estudo mostramos que a escolha do biomaterial e a topografia de superfície combinados com células de interesse são fatores-chave que podem favorecer a reparacao óssea.

Palavras-chave: Eletrofiação. Rotofiação. Fibras de policaprolactona. Nanohidroxiapatita. Nanotubos de carbono. Células-tronco mesenquimais da medula óssea. Reparo ósseo.

ABBREVIATIONS

ALP: Alkaline phosphatase

BMMSCs: Bone marrow mesenchymal stem

Ca3(PO4)2: Calcium phosphate

CNT: Carbon nanotubes

CT: Stem Cells

ECM: Extracellular matrix

FDA: Food and Drug Administration

HOB: Human osteoblast

IL1: Interleukin-1

IL6: Interleukin-6

MSCs: Mesenchymal stem cells

MWCNT: Multi walled carbon nanotube

NCD: Nano-crystalline diamond

nHap: Nanohydroxypatite

PCL: Polycaprolactone

PLGA: Poly lactic-*co*-glycolic acid

PVA: Poly (vinyl alcohol)

SWCNT: Single walled carbon nanotube

TGFβ: Transforming growth factor beta

TiO_2: Titanium dioxide

TNFα: Tumor necrosis factor

FIGURES

TABLES

EQUATIONS

TABLE OF CONTENTS

1 OVERVIEW

This PhD. thesis approaches the development of polycaprolactone (PCL) fibers with CNT and nHap nanoceramics, using two different methods for fabrication: ES and RJS. First, polymeric PCL fibers were developed (without the incorporation of nanoparticles) under different concentrations of polymer until the material with the best fiber characteristics was obtained. Once standardized, the materials were characterized. The analyses were of morphology, wettability, thermal property, bacteria colonization, and cytotoxicity effect. Subsequently, nHap and CNT nanoparticles were incorporated in the standardized fibers. It was then characterized and analyzed *in vitro* in the human osteoblast (hOB) lineage, evaluating its biological activity (cell morphology, viability and proliferation, alkaline phosphatase (ALP) activity, and calcium deposition). The materials that showed more significant osteoblast functions for both methods were determined and analyzed *in vivo*. The *in vivo* effects of scaffolds without and with bone marrow mesenchymal stem cells (BMMSCs) seeded were evaluated by graft in a critical defect in rat calvaria.

The use of nHap and CNT nanoceramics are attractive for regenerative medicine due to their osteoconductive characteristics and high mechanical properties, respectively. A new composite based on nHap / CNT was patented by Prof. Dr. Anderson Lobo, responsible for this research project (Patent: BR10201300578). Besides, BMMSCs are an excellent source of cells to minimize tissue damage. Therefore, the combination of PCL scaffolds with nHap, CNT, and BMMSCs was a strategy to enhance bone tissue repair.

The production of polymeric fibers using the electrospinning and rotating technique was carried out at the University of Vale do Paraíba (UNIVAP) under the supervision of Professor Dr. Anderson de Oliveira Lobo.

In vitro experiments were performed at Northeastern University under the supervision of Professor Dr. Thomas J. Webster.

Bacteria colonization experiments were carried out at Northeastern University under the supervision of Professor Dr. Thomas J. Webster and the University of Campinas (UNICAMP) under the supervision of Professor Dr. Marcelo Lancellotti.

In vivo analyses were performed at Universidade Estadual Paulista (UNESP) under the supervision of Professor. Drª. Luana Vasconcellos and Prof. Dr. Macus Alexandre Finzi Corat from the University of Campinas (UNICAMP).

The present thesis shows that the choice of biomaterial and the scaffold morphology combined with cells of interest are key factors that can favor bone repair.

2 INTRODUCTION

Although bone tissue has a capacity for regeneration, when critical defects occur due to significant injuries resulting from trauma or pathologies, the patient's endogenous regeneration capacity is limited [1, 2]. Therefore, the repair or replacement of bone tissue represents a significant challenge for medical and dental clinics. Current bone repair treatments are performed using autologous, allogeneic, and xenogenic bone grafts; however, these grafts have substantial limitations, such as limited material, immune rejection, infection, and disease transmission [3-5]. Therefore, synthetic biomaterials are being explored as a promising alternative to overcome the limitations found in current bone tissue replacement or repair treatments. Polymeric fibers have been widely studied as a promising biomaterial for use as scaffolds for bone tissue engineering applications due to their structure similar to the extracellular matrix; in addition, they can be designed according to specific needs [6-8].

Among the most used methods to produce polymeric fibers are electrospinning (ES) and rotary jet spinning (RJS). ES is a widely used and relatively economical method to produce fibers. Es uses an electric field to produce ultrathin fibers. The high voltage is applied between a grounded collector and a polymer solution. Under the applied electrostatic force, the polymer is ejected from the nozzle, forming a jet called a Taylor cone. Lastly, in the path to the collector, the solvent evaporates, producing the fibers. However, the ES requires a high voltage electric field that depends on the solution's conductivity and has imprecise control over fiber orientation and has a low production rate, limiting its wide-spread application [9-11].

In contrast, RJS is a simple method that provides higher production rates. It uses high-speed rotation to manufacture aligned fibers, in which the polymer solution is ejected from the nozzles, and the solvent evaporates, producing the fibers. Therefore, this method requires a highly volatile solution [12, 13]. Despite the differences between the techniques, both show very promising studies, such as supports for biomedical applications [10, 14-16].

Polycaprolactone (PCL) is a biodegradable, biocompatible polymer, and its semi-crystalline nature provides high mechanical properties. Besides, its cost is relatively accessible and can be modified without significant loss properties. This polymer has been widely used to develop scaffolds for regenerative bone applications, drug delivery, and cartilage regeneration [17, 18].

New strategies based on well-defined combinations between osteoconductive materials, support, and osteogenic cells are seen as an approach to improving bone regeneration [19-21]. Incorporating nanoceramics of carbon nanotubes (CNT) and hydroxyapatite (nHap) into the polymeric matrix can be an alternative to enhance the characteristics of PCL fibers, in addition to offering great potential in the tissue regeneration process. CNTs have high mechanical properties and are often used as reinforcement material [22, 23]. nHap has excellent osteoconductive properties and is considered an excellent bioceramic material to produce scaffolds to promote bone repair [24, 25].

Besides, there is a significant interest in using implantable biomaterials in combination with bone marrow mesenchymal stem cells (BMMSCs) to minimize tissue damage. These cells are the most commonly used source in cell therapy; because they have the potential to differentiate into various types of cells of the mesenchymal lineage, immunomodulatory capacity, and paracrine effect [20, 26-28]. Several studies have shown that BMMSCs can be useful in repairing or regenerating myocardial tissues, bone tissue, tendon, cartilage, and meniscus [29-31]. Besides, preclinical trials have demonstrated that scaffolds seeded with BMMSCs increase osteogenic capacity [20, 32-34].

Therefore, the combination of PCL scaffolds with nHap and CNT nanoparticles with BMMSCs can be an advantageous way to improve bone tissue repair.

The main goal of this thesis was to investigate the best technique to produce a polymeric biomaterial (PCL) with the incorporation of nHap and CNT nanoparticles, which result in better biological responses *in vitro* and *in vivo*.

The design, characterization, and some *in vitro* effects of the produced materials were first described by Machado-Paula et al. [35], published in Materials Science and Engineering C (Paper 1). In sequence, it had been demonstrated that the scaffold with nHap and CNT has the potential to stimulate biological activity in osteoblast cells compared to pure PCL. BMMSCs were seeded on the engineered scaffolds and implanted in a rat model to assess their potential in the reconstruction of critical bone defects in the calvaria, compared to acellular scaffolds. Among the results, we observed that the greater bone neoformation occurred through the combination of the three characteristics presented, specifically the presence of nHap and CNT nanoparticles, morphology surfaces produced by RJS fibers, and BMMSCs. These results had been reported in Paper 2.

As such, this study showed the promising potential of a well-defined combination of suitable nanocomposite scaffolds with seeded BMMSCs for improved bone tissue engineering applications. These findings contribute to the manufacture of intelligent structures that can modulate cellular behavior, mediating biological signals to conduct tissue formation properly.

3 LITERATURE REVIEW

Bones have the function of supporting and protecting the organism, besides providing locomotion and functioning as a deposit of calcium, phosphorus, and ions. The bone matrix is made up of organic and inorganic parts. The organic matrix's main element is collagen fibers, mainly type I, proteoglycans, adhesive glycoproteins, and non-collagenous proteins such as (osteocalcin, osteopontin, and osteonectin). Besides, it has cellular components constituted by osteoblasts responsible for the deposition of the bone matrix, osteocytes accountable for bone maintenance, osteoclasts are responsible for bone resorption, and the osteogenic cell that is a stem cell that is the precursor of an osteoblast, see details in **Fig. 1** [1, 36]. The inorganic matrix is composed mainly of calcium and phosphate, and fewer of magnesium ions, sodium, potassium, and carbonate. The combination of phosphate and calcium forms crystals of hydroxyapatite, $Ca_3(PO_4)2$, constituting approximately 60 to 70% of the bone's weight, which is associated with collagen fibers, which provides the strength and hardness, characteristics of bone tissue [1, 36].

Figure 1: Bone cell types and function.

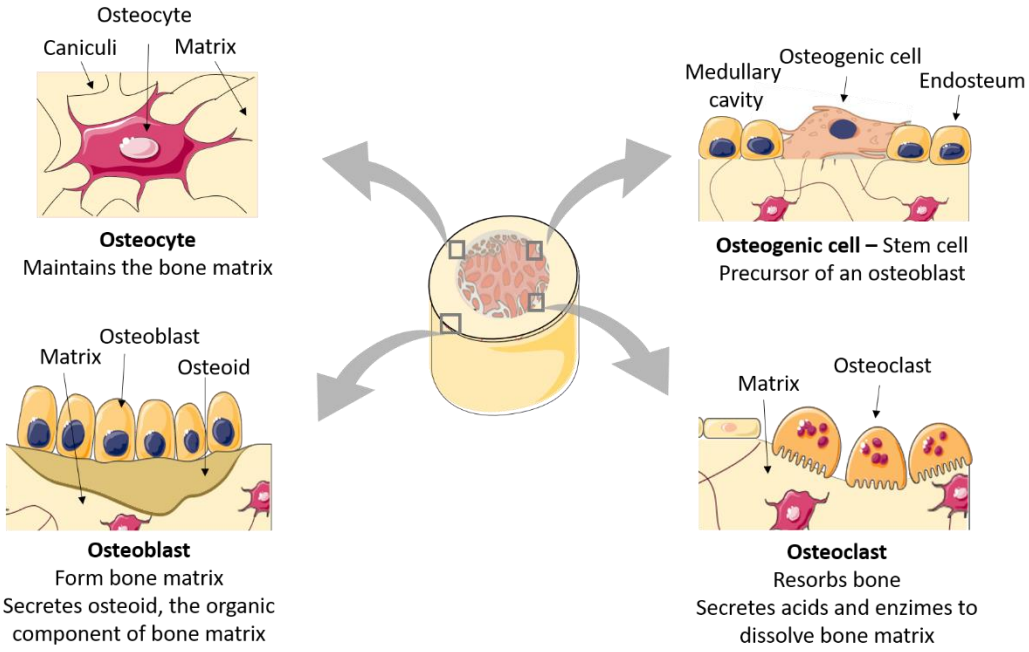

Source: Adapted from [37-39].

Macroscopically, bone tissue is classified as compact bone or cortical bone (outer layer of bones) and spongy bone (inner layer of bones) **(Fig. 2).** Compact bone provides protection and strength as well as surrounds the medullary cavity. It consists of units called osteons or Haversian systems that contain osteocytes connected by canaliculi, which consists of a set of lamellae surround a central canal (bone's blood vessels and nerve fibers). Osteons are aligned parallel to the bone's long axis, helping the bone resist bending or fracturing. The spongy bone corresponds to a network of trabeculae inserted in small spaces in the medullary compartment. It is highly vascular, which delivers nutrients to osteocytes and removes waste. Red-bone marrow is found between the trabeculae where the production of blood cells occurs (hematopoiesis)[40, 41].

Figure 2: Bone tissue structure.

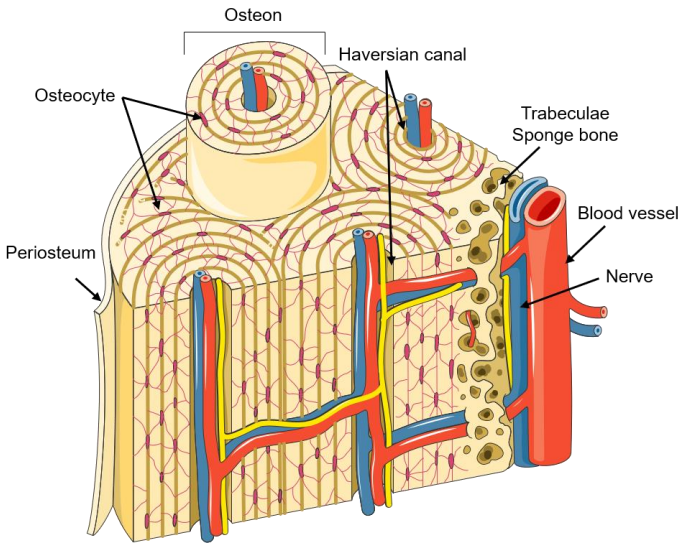

Source: Adapted from [39]

The bones are highly dynamic structures; it is a tissue that undergoes a continuous process of renewal and remodeling through resorption and deposition of bone matrix. Remodeling allows tissues already worn out or those who have suffered injuries such as microfractures replaced by new tissues [42, 43].

The natural process of fracture regeneration occurs in three main stages: the inflammatory phase, repair, and remodeling **(Fig. 3A)**. The inflammatory phase occurs at the beginning of the fracture due to the hematoma caused. There is an

extended-release of cytokines specialized in bone repair (TGFβ, IL1 and 6, PGE2, TNFα). Besides, stem cells (CT) and osteoprogenitor cells express bone morphogenetic proteins (BMP) indispensable in the pre-osteoblast maturation path in osteoblasts and, consequently, bone formation.

In the repair process, there is the formation of a collagenous matrix called bone callus and the formation of blood vessels in which they develop from the blood support. Healing does not occur without angiogenesis, which is an essential step in bone formation. The bone callus provides the necessary protection and stability for bone remodeling to occur [44, 45]. In the remodeling phase, the bone callus is reabsorbed and remodeled; in this process, the osteoclasts and osteoblasts act, reabsorbing and depositing bone, respectively. This process can take from months to years to complete and form a tissue closer to natural [1, 46]. Bone remodeling, e.g., of old tissue, involves detecting multiple signaling molecules for remodeling **(Fig. 3B)**. Signals generated by osteocytes or through direct endocrine activation are detected by osteoblasts, which recruiting osteoclast precursors, and from there, the same process of resorption and remodeling occurs [47-49].

However, when referring to extensive injuries called critical defects, in this case, regeneration does not occur spontaneously [1, 2, 45]. Therefore, bone tissue replacement represents an essential challenge for medical and dental clinics [50-52].

Figure 3: Bone repair and remodeling cycle.

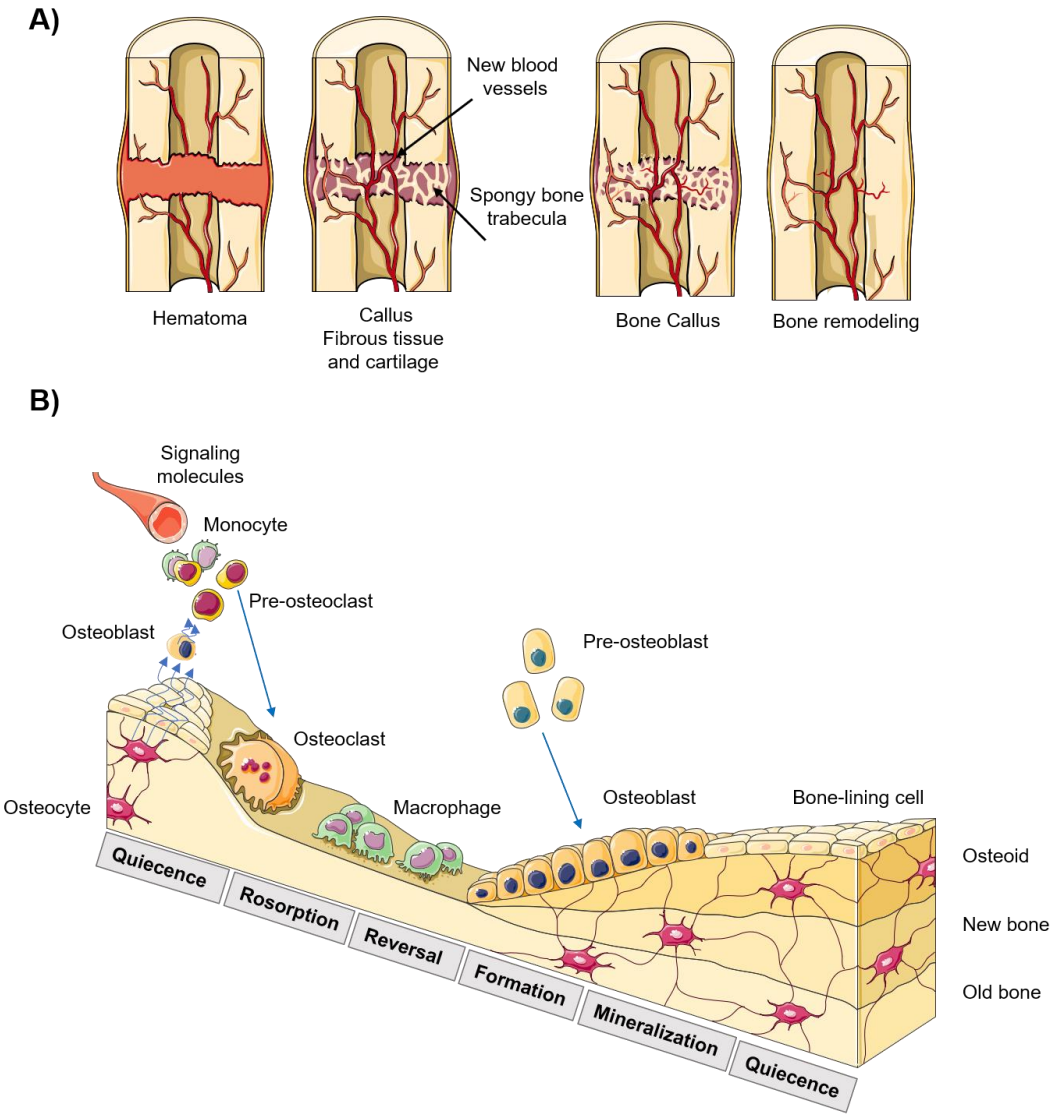

Source: Adapted from [37, 39].

Among current treatments, bone grafting with autograft is still considered a standard gold method due to its greater osteogenic capacity. Nonetheless, this approach is limited due to the amount and morbidity from bone graft harvested [3, 4, 53, 54]. An alternative treatment is allografts and xenografts. Allografts are the second option in orthopedic surgery, and Xenografts are biological apatite derived from animal bone, available in large quantities. However, they also have limitations: lower osteogenic capacity, the potential for infections, immune rejection, and disease transmission [3-5, 55, 56].

The bone repair and remodeling process involve a complex cascade of biological responses, and the interaction between cell-cell and cell-environment

becomes significant to restore tissue function. Besides, the cell adhesion process is an essential requirement for successful graft incorporation for tissue repair [43, 51].

Faced with a sensitive biological system, the materials used as scaffolds in tissue engineering have been diverse and often challenging [57-59]. One of the significant challenges of regenerative medicine is to design and manufacture a suitable scaffold that allows cells to multiply, differentiate, and originate in a new tissue similar to natural [58, 60, 61]. One of the crucial components in tissue engineering is support, providing a model for fixing cells and tissues, growth and formation of the extracellular matrix (ECM) [58, 60]. Thus, the choice of the biomaterial used is fundamental to allow the cells to form an adequate tissue [61, 62]. Therefore, it is important to manufacture new materials with better physical and chemical characteristics than those currently used [63, 64].

Another essential factor is the mechanical properties of the material that provides tissue support, in which it must be resistant enough to withstand physiological stress. Besides, to achieve isomorphic tissue replacement, the support must biodegrade at a rate corresponding to ECM's deposition [52, 62].

Therefore, the desirable conditions for the production of scaffolds involve three-dimensional (3D) structures that can mimic the environment *in vivo*, favorable mechanical property, biodegradable, biocompatible, and osteoconductive [51, 65].

In general, biomaterials are structures that can be used as scaffolds for studies of tissue regeneration *in vitro* or *in vivo* [58, 66]. Some examples of these biomaterials include TiO2 nanoparticles [67], nHap [68], Nano-crystalline diamond (NCD) [69], polymer fibers [14], CNT [70], and other diverse substrates (polymeric, ceramic, or metallic) in order to increase mechanical stability and improve interaction with the fabric [62, 71].

Polymeric fibers are one of the materials that most resemble the fibrous structures of native MEC. They can be synthesized from various types of natural polymers such as MEC proteins (collagen, elastin, and fibronectin) and synthetic polymers such as poly ε-caprolactone (PCL), poly lactic-glycolic acid (PLGA), and poly polyvinyl acetate (PVA). Polymeric fibers have been used to support the engineering of tissues such as cartilage, bones, blood vessels, and other structures [7, 8].

The PCL has the linear formula $(C_6H_{10}O_2)_n$ **(Fig. 4).** This polymer has been widely used in tissue engineering for its biocompatibility and biodegradability. Its

semi-crystalline nature provides superior mechanical properties (high strength and elasticity) at a relatively affordable cost. Besides, they can be modified without significant loss of their properties. PCL reaches a liquid state between 59 and 64 ° C; therefore, they have high elasticity at the physiological temperature as it comes to a rubbery state [17, 18]. For these qualities, the PCL stands out before other polymers. This polymer is using for the development of scaffolds for regenerative bone applications, targeted drug delivery, and cartilage regeneration [12, 18]. The PCL has also been approved by the United States Food and Drug Administration (FDA) [18, 72].

Figure 4: Polycaprolactone structure.

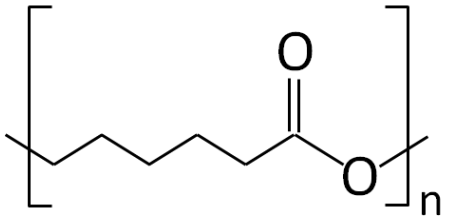

Source: From [73]

Among the various techniques commonly used to generate ultrathin PCL fibers, electrospinning (ES) has been widely studied, and more recently, rotary jet spinning (RJS) was introduced. In comparison, electrospinning is better known and is relatively economical for producing ultrafine fibers. Three-dimensional fibrous structures that mimic natural MEC can be easily manufactured with this process [10, 14]. Several researchers have demonstrated that fibrous scaffolds by ES allow a better and more natural environment for cell attachment and proliferation since they mimic the MEC's topography [10, 74-76].

Electrospinning uses an electric field to create a potential difference between a grounded collector and a polymer solution, in which the liquid is expelled through the capillary of a needle. As the voltage increases, the charged electrostatic force overcomes the liquid's surface tension, causing a jet to form, called the Taylor cone. Finally, on the way to the collector, the solvent evaporates, producing the fiber **(Fig. 5A)** [10, 76, 77]. Despite the popularity and versatility of ES, it requires a high voltage electric field that depends on the solution's conductivity and has imprecise control

over fiber orientation and has a low production rate, limiting its wide-spread application [11, 13].

In contrast, RJS is a simple method as it uses high-speed rotation for producing aligned fibers. This technique does not require a conductive solution, but a solvent with a low boiling point is necessary. The polymer fiber diameter and porosity can be controlled by varying nozzle geometry, rotation speed, and polymer solution properties. Furthermore, RJS provides higher production rates compared to those fabricated via ES, 5 µL of solution per min−2 compared to 1 mL of solution per min−1 per nozzle, respectively [11, 13, 78]. Although this technique is relatively new, there have been several very promising studies on RJS for biomedical applications [11, 13, 15].

The RJS system consists of a reservoir with two opposite poles attached to a motor's shaft with controllable rotation speed. When the reservoir spins on its axis, it ejects a polymeric jet through the centrifugal force's holes. The solvent evaporates while the jet travels in a spiral, forming ultrafine fibers **(Fig. 5B)** [12, 78].

RJS and ES are methodologies that may produce different materials with a particular characteristic in their structure, in what may bring insights to resolve problems found in the biomedical engineering field of implants.

Figure 5: Electrospinning (A) and Rotary jet spinning (B) scheme.

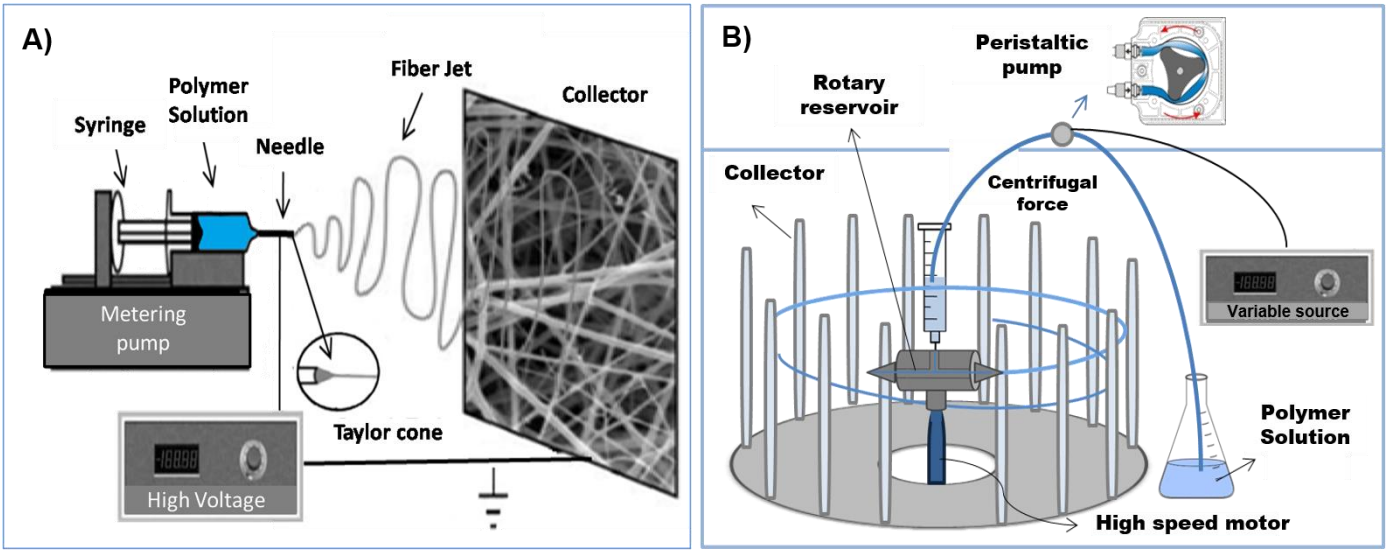

Source: The author.

Besides, to improve the properties of polymeric biomaterials and minimize damage to bone tissue, several studies have been carried out by combining different materials called composite [79-82]. Composites consist of a combination of different types of materials, in which the unique advantage of a given material can be used to supply the defect of the other [71]. Technologies based on well-defined combinations of osteoconductive matrices, osteoinductive factors, and increased mechanical property are desirable for bone reconstructive surgery. They have been showing success in stimulating the regenerative process [83].

The incorporation of nanoceramics of carbon nanotubes (CNT) and nanohydroxyapatite (nHap) in the polymeric matrix can be an alternative to improve PCL's physical-chemical characteristics addition to offering enormous potential in the tissue regeneration process. The physical-chemical characteristics are related to the surface, wettability, thermal and mechanical properties of the materials.

nHap has the chemical formula of $Ca_{10}(OH)_2(PO_4)_6$ **(Fig. 6)** with a Ca/P ratio of 1.67. nHap is a bio-ceramic of the calcium phosphate class commonly used to repair and replace bone tissues due to its similar bone mineral composition properties. Due to this similarity, it has excellent biocompatibility and osteoconduction, which gives you an advantage over other devices used to replace bone tissue. However, nHap has low mechanical properties, which restrict its use in places subject to traction. [25, 81, 84].

Figure 6: Structure of nanohydroxyapatite.

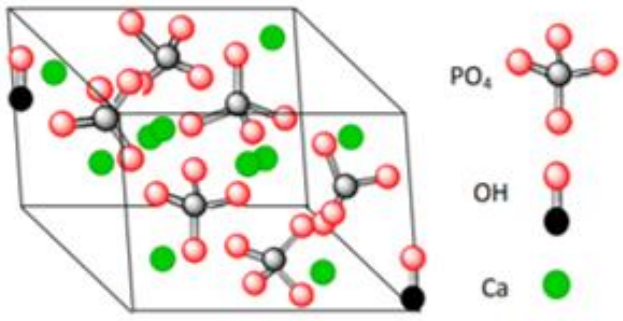

Source: From [85].

CNTs are carbon atoms forming a hexagonal network. There are two types of CNTs: Single-walled (SWCNT) **(Fig. 7A)** with a diameter of 0.4-2 nm and multi-

walled (MWCNT) **(Fig. 7B)**, consisting of two or more simple layers of graphite, with diameters reaching more than 100 nm. CNT's are often used as reinforcement material due to its unique physical, mechanical, and electrical properties. CNTs have high biocompatibility; it behaves like an inert matrix to support the proliferation of cells. The superficial modification of the CNT, changing its wettability, thus presenting a hydrophilic characteristic favors the contact surface with adhesion proteins, essential in adhesion, growth, and extracellular matrix formation [22, 86]. Therefore, CNTs are considered ideal candidates to improve the mechanical properties and biological performance of nHap.

Accordingly, it considers that the combination of PCL scaffold with nHap and CNT nanoceramics may be an approach to improve the potential tissue regeneration.

Figure 7: Structure of CNTs (A) Single-walled carbon nanotube (SWCNT) and (B) Multi-walled carbon nanotube (MWCNT).

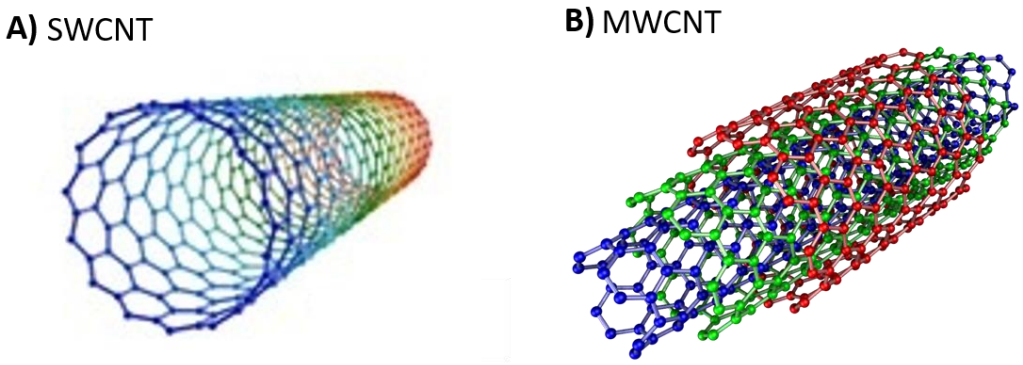

Source: Adapted from [87] and [88].

Further, there is a significant interest in using implantable biomaterials combined with stem cells (SCs) to minimize tissue damage [20, 26, 27]. Stem cells can be isolated from embryos, fetuses, or adults. Using adult stem cells (ASCs) is well accepted by society and does not involve the same ethical and religious considerations as seen using stem cells from embryos or fetuses. Besides, ASCs can be isolated from several organs and tissues [89-91]. Especially, bone marrow stem cells (BMSCs) remain the best source for obtaining these cells and for use in cell therapies. The bone marrow comprises at least two kinds of stem cells, hematopoietic stem cells (HSC), which give rise to blood cells, and mesenchymal

stem cells (MSC), which is the best pluripotent cells among them, but make up a smaller proportion [90, 92, 93].

Although MSCs are easily obtained from many tissues, such as the umbilical cord, placenta, fat, lung, liver, and skin, those derived from adult bone marrow have been more intensively studied. BMMSCs have a self-renewal ability and multi-lineage differentiation potential. They have also been reported to trans-differentiate into not only mesoderm lineages but also ectodermal and endodermal cells, also have the immunomodulatory capacity and paracrine effect [29, 31, 92, 94]. MSCs can repair damaged tissue through cell differentiation or a paracrine effect. The paracrine effect is signaling of MSCs in which it stimulates the cells of the damaged tissue to self-repair, in addition to promoting the migration of cells specialized in the tissue repair process and immunomodulatory effect. This mechanism minimizes damage to the tissue and helps in tissue regeneration [31, 92, 95].

Scaffolds with BMMSCs seeded have been considered as an approach for improving tissue regeneration. Many preclinical trials showed that this strategy enhances osteogenic capacity [20, 32-34]. Therefore, the combination of PCL scaffolds with nHap and CNT nanoparticles with BMMSCs can be an advantageous way to improve bone tissue repair.

These approaches can contribute to the manufacture of intelligent structures that can modulate cellular behavior, mediating biological signals to properly conduct tissue formation, which are significantly attractive in tissue engineering.

4 OBJECTIVE

4.1 General objective

Demonstrate the best technique for producing a polymeric biomaterial (PCL) with the incorporation of nHap and CNT nanoceramics, and which of them result in better biological responses *in vitro* and *in vivo*.

4.2 Specific Objectives

- ✓ .....Produce PCL fibers by electrospinning and rotary jet spinning
- ✓ .....Characterization of biomaterial
- ✓ .....Standardize which fibers are best for each technique
- ✓ .....Incorporate nHap and CNT nanoparticles into standardized fibers and characterize them
- ✓ .....Evaluate fibers *in vitro*, in human osteoblast cells (hOB) by analyzing their biological activity: (cell morphology, viability and proliferation, alkaline phosphatase (ALP) activity, and calcium deposition)
- ✓ .....Standardize which fibers are best for each technique for *in vivo* use
- ✓ .....To evaluate bone neoformation after implantation of biomaterial without and with bone marrow mesenchymal stem cell in rat calvaria defect.

5 METHODOLOGY

5.1 **Production of CNT and nHap nanoparticles**

5.1.1 Synthesis of superhydrophilic MWCNT

Multi-walled carbon nanotubes (MWCNT) were produced by a chemical vapor deposition method by a mixture of camphor ($C_{10}H_{16}O$, 84 wt.%) and ferrocene (Fe $(C_5H_5)_2$, 16%) as a catalyst, and it was vaporized at 220 °C in an antechamber. The vapor was carried by an argon gas flow at atmospheric pressure to the chamber of a CVD furnace (850 °C), allowing for the deposition of MWCNT on the quartz wall tube. The purification process for removing Fe nanoparticles from the produced MWCNT was performed by a high-temperature annealing technique under an oxygen-free atmosphere (N_2)[96]. The functionalization of MWCNT was achieved by incorporating oxygen-containing functional groups to provide them with superhydrophilic character. A direct pulsed current plasma reactor with a 1sccm rate oxygen flow, 85mTorr pressure, under -700 V, and pulse frequency of 20 kHz at 50% of the duty cycle with 5-time intervals of 40 minutes each, were used for this process, as described elsewhere [86, 97, 98].

5.1.2 Synthesis of nHap

The nHap precipitation was completed using the following reagents: calcium nitrate tetrahydrate [Ca $(NO_3)_2.4H_2O$] and ammonium phosphate monobasic [$(NH_4)H_2PO_4$]. These concentrations were chosen so that Ca/P=1.67. Firstly, the solutions were prepared separately in which the powders were dissolved in 90 mL of deionized water. Then, the solutions were mixed simultaneously, and 18 mL of ammonium hydroxide [NH_4OH] was added to the solution to fix the pH. Next, the mixture was sonicated using ultrasound (Ultrasonic Processor 500 W; 20 kHz; 13 mm probe; model: SO-VCX-500, SONICS) for 30 minutes. The resulting suspension was left for 72 hours in a 2,000 mL container and then washed with deionized water until the pH reached a constant value (~ 6). Then, the powder was placed in the oven for 48 h at 60°C and ground using an analytical mill (Model A11, IKA, with an engine speed of 28,000 rpm) to obtain the nHap powder.

5.1.3 Synthesis of CNT:nHap

Initially, the MWCNTs (1% m/v) were diluted in deionized water, and then the salts for Hap: Ca $(NO_3)_2.4H_2O$ and (NH_4) H_2PO_4; (Ca/P=1.67) were added. The pH control was controlled with NH_4OH (pH ~10). The precipitations were subjected to ultrasound (Ultrasonic Processor 500 W; 20 kHz; 13 mm probe; model: SO-VCX-500, SONICS) for 30 minutes. The resulting suspension was left in the oven for 48 h at 60°C and ground using an analytical mill (Model A11, IKA, with an engine speed of 28,000 rpm) to obtain the CNT/nHap powder.

5.2 **Production PCL fibers**

5.2.1 Polymeric fibers groups

Polymeric fibers were produced using Polycaprolactone (PCL – Mw 80,000, Sigma- Aldrich®) by electrospinning (ES) and rotary jet spinning (RJS) techniques. Firstly, different concentrations of PCL were produced. In the ES method, PCL concentrations were: (12%, 15%, 17%, and 20% w/t), and in the RJP method, (15% and 20% w/t). After determining which polymeric concentration presented the best conditions for both techniques, nanoparticles' incorporation was carried out. It was determined that the PCL with 17% (w/t) obtained by ES and PCL at 15% (w/t) for RJS showed the best fiber characteristics. Table 1 shows the groups of materials that were produced, constituting in 4 groups for each technique, with or without the incorporation of nanoceramics (carbon nanotubes - CNT and hydroxyapatite -nHap).

In the other concentrations, the Polymeric solution was too dense (high concentration) or very liquid (low concentration), and they were difficult or not possible electrospun or rotary jet spun.

Table 1. Group of samples

	Polymeric solution
A	PCL
B	PCL + 1% CNT

C	PCL + 1% nHap
D	PCL + 1% nHap:CNT

5.2.2 Polymeric solution for electrospinning and rotary jet spinning

PCL was prepared in different concentrations (w/t). For ES, the PCL polymer was dissolved in acetic acid (CH_3COOH, glacial – Synth), and for RJS, the PCL was dissolved in chloroform (99%, Sigma- Aldrich®).

The solutions were magnetically stirred at 20ºC until completely dissolved. The entire procedure was performed in a closed system to avoid moisture precipitation, thus obtaining a perfect homogenization of the final solution.

To incorporate the nanoparticles, while the PCL was dissolving, 1% of the nanoparticles were mixed in the solvent under ultrasonic agitation for 60 minutes. Then they were mixed to the polymeric solution.

5.2.3 Electrospinning and rotary jet spinning of PCL fibers

For ES the appropriate parameters (applied voltage, working distance, feed rates, and needle diameter) for the electrospinning process were checked. The polymer solutions were placed in a syringe (BD Yale, 5 mL) with a metal needle tip, and it was coupled to an infusion pump to control feed rates of the solution. A voltage was applied between the needle tip and the ground collector (see details in **Fig. 5A**). ES conditions were established as follows: 16 kV, needle tip (gauge 23), 15 cm as needle-collector distance, 0.8 mL h^{-1}, controlled temperature (23 °C), and humidity (~30%). The fibers were randomly oriented and collected on an aluminum foil.

The rotary jet spinning was made in the laboratory (see schematically in **Fig. 5B**). This system was constructed consisting of a mounted rotatable nozzle, with an inner volume of 6 mL with two end holes, where the tip was at 0.9 mm in diameter rotating on its vertical axis coupled to an MR– 115 Mini – Motor (3000 to 30.000 rpm - were used the speed 2 of the motor). The polymer solutions were placed in a syringe (BD Yale, 5 mL) coupled with the constant feed system with a peristaltic pump system installed (controlled by potentiometer). The fibers were collected

through static collectors. Extrusion was conducted at ambient temperature and humidity at 30% – 45%.

5.3 **Characterization**

5.3.1 Scanning electron microscope (SEM)

Scanning Electron Microscopy (Hitachi S-4800) was used to characterize the surface of the samples and the morphology of the cells. The samples or cells were prepared and coated with a thin layer of platinum (~ 10 nm) using a sputter-coat system for 2 minutes. Then the micrographs were obtained, and the voltage was 3.0 kV.

5.3.2 AFM analysis

An Atomic Force Microscope, NTEGRA *Spectra*, was used to obtain AFM images. The different areas were scanned using 0.3 Hz in non-contact mode. In all cases, the image was composed of 512 x 512 pixels.

The *Nova* program of NTMDT was used to perform the analysis. At the first stage, in the original image, a filter was applied to flatten the image. This first correction was necessary due to the piezoelectric that controlled the scanner. The Root Mean Square (σ_{RMS}) Roughness was calculated through the following equation applied throughout the image:

Equation 1. Root Mean Square (σ_{RMS}) Roughness

$$\sigma_{RMS} = \sqrt{\frac{1}{N_y N_x}\left(\sum_{j=1}^{N_y}\sum_{i=1}^{N_x}\left(Z_{ij} - \bar{Z}\right)^2\right)} \quad (1)$$

N_x Is the number of pixels in the x direction and N_y in the y direction; $\bar{Z}$ is the mean height and Z_{ij} is the height at the ij pixel. In a second step, a High-Pass 3x3 filter was applied, allowing one to isolate the fibers from the rest of the image. From this processed image, we obtain the Filtered Root Mean Square $(\sigma_{RMS\,FIL})$ Roughness,

and finally, using the Dangwoo et al. expression [99], we obtained the Effective Root Mean Square $\sigma_{RMS\ EFF}$ Roughness.

5.3.3 Contact angle and surface energy measurement

The characterization of the wettability and surface energy of material allows for a later interpretation of cellular behavior. The wettability of the samples was determined using a goniometer (DSA100, Krüss), and for measuring contact angles, single drops of deionized water and diiodomethane were dropped on the surface of the samples (n= 3).

The measurement was based on the Young-Laplace method (sessile-drop), in which 2µl of deionized water and diiodomethane is deposited on the material surface. Images of the drop in contact with the sample were captured, advanced measurements (5 min) of the angle were taken from 5 to 3000s at room temperature.

The surface energy was calculated, and the work of bacteria adhesion was also inserted. The surface energy composed of polar and dispersive components of the samples was evaluated by measuring the contact angle. The interfacial tension between two condensed phases can be determined by Young' equation [100], according to which

Equation 2. Young' equation

$$\cos\theta\gamma_{LV} = \gamma_{SV} - \gamma_{SL}$$

Where θ is the measured contact angle between the liquid and solid, and γ_{LV}, γ_{SV}, and γ_{SL} are the interfacial energies of the liquid/vapor, solid/vapor, and solid/liquid interfaces, respectively. This equation can be rewritten as the Young-Duprè equation:

Equation 3. Young-Duprè equation

$$W_a = \gamma_{LV}(1+\cos\theta) = \gamma_{SV} - \gamma_{SL}$$

Where W_a is the adhesion energy per unit area of the solid and liquid surfaces. In the general form of equation (1), (2) then can be written:

Equation 4. Young-Duprè equation

$$\gamma_{LV}(1+\cos\theta) = 2\sqrt{\gamma_L^p \gamma_S^p} + 2\sqrt{\gamma_L^D \gamma_S^D}$$

Where γ^p_L and γ^p_S are the polar components of the surface energy of liquid and solid phases, respectively, and γ^D_L and γ^D_S are the dispersive component of the surface energy of the liquid and solid phases, respectively. Because γ^D_L and γ^p_L have been published for many liquids, it is possible to approximate γ^D_S and γ^p_S from a single measurement of θ by with equation (4). Therefore, by measuring the contact angles of two different liquids (distilled water and diiodomethane) with well-known polar and dispersive components of surface energy (Table 1), Eq. (4) can be solved to determine the polar and dispersive components of the surface energy of the materials [101, 102]. The liquid was dropped automatically by a computer-controlled system. All measurements were carried out at room temperature.

Table 2. Test liquids and their surface tension components [101].

Surface tension data (mN/m)	γ^D_L	γ^p_L	γ_{LV}
Water	21.8	51.0	72.8
Diiodomethane	50.8	0.0	50.8

Thermodynamically, the process of adhesion and spreading of cells and bacteria from a liquid suspension onto a solid substrate can be described by the following equation [103]:

Equation 5. The equation for surface thermodynamics of bacterial adhesion

$$\Delta F_{Adh} = \gamma_{BS} - \gamma_{BL} - \gamma_{SL}$$

where ΔF_{Adh} is the interfacial free energy of adhesion, γ_{BS} is the bacteria-solid substratum interfacial free energy, γ_{BL} the bacteria-liquid interfacial free energy, and γ_{SL} is the solid-liquid interfacial free energy, respectively. They can be calculated by using contact angle data and the van Oss acid-base approach [104-106].

The following equation was used to determine the interfacial energy of cell adhesion to a solid surface [104-106]:

Equation 6. Equation of interfacial energy of cell adhesion to a solid surface.

$$\Delta F_{Adh} = 2\begin{pmatrix} \sqrt{\gamma_S^{LW}\gamma_L^{LW}} + \sqrt{\gamma_S^{p}\gamma_L^{D}} + \sqrt{\gamma_S^{D}\gamma_L^{p}} \\ + \sqrt{\gamma_B^{LW}\gamma_L^{LW}} + \sqrt{\gamma_B^{p}\gamma_L^{D}} + \sqrt{\gamma_B^{D}\gamma_L^{p}} \\ - \sqrt{\gamma_S^{LW}\gamma_B^{LW}} - \sqrt{\gamma_S^{p}\gamma_B^{D}} - \sqrt{\gamma_S^{D}\gamma_B^{p}} - \gamma_L \end{pmatrix} . \quad (5)$$

According to thermodynamic theory, if ΔF_{Adh} is negative, bacteria spreading is energetically favorable, while if ΔF_{Adh} is positive, bacteria spreading is thermodynamically unfavorable.

5.3.4 Differential scanning calorimetry (DSC)

Differential scanning calorimetry (DSC, Q10, TA instruments) was used to evaluate the thermal parameters from the produced fibers. For that, the following parameters were used: a heating rate of 10 ºC min^{-1}, the temperature ranged from -150 to 250 ºC, and an atmosphere of N_2 (at a flow rate of 50 mL min^{-1}). The sample weight ranged from 8 to 10 mg. In order to determine the degree of crystallinity (Xc) of the samples, the following equation was used:

Equation 7. Degree of crystallinity (%)

$$X_c = (\Delta H_m / \Delta H^o_m) \times 100\ \%$$

Where ΔH_m corresponded to the heat of fusion of the endothermic peak of fusion, and ΔH^o_m was the heat of fusion for the 100% crystalline raw PCL.

5.3.5 Bacteria colonization

Bacteria colonization within the polymeric scaffolds was assessed by colony-forming units (UFCs) and by micrographs. Responses from gram-positive and gram-negative bacterial strains were observed.

Staphylococcus aureus (ATCC-12600) [American Type Culture Collection, Manassas, VA, USA], Staphylococcus aureus RiB1, Staphylococcus aureus (BEC9393), Staphylococcus epidermidis, Pseudomonas aeruginosa (ATCC 35984), Pseudomonas aeruginosa (ATCC 2785), Pseudomonas aeruginosa 31NM, and Klebsiella pneumoniae KP230 were used in this study. Initially, polymeric scaffolds were cut (1 x 1 cm2) and sterilized under ultraviolet light for 30 min on each side.

A single colony of bacterial strains described above was inoculated in 3% Tryptic soy broth (TSB, 5 ml) under agitation at 120 rpm (Innova 2000 platform shaker) held at 37°C for 14 hours. This bacteria solution was diluted to produce a working solution at concentrations of 104 cells/ml. Afterward, the samples were set into 24-well tissue culture plates and individually inoculated with 1000 µL of a bacteria working solution and incubated for 24 h at 37°C in the presence of 5% CO^2. Afterward, the samples were lightly rinsed with PBS (x2) to remove any non-adherent bacteria; next, the scaffolds were set into individual vials with PBS (1000 µL) then vortexed during 15 min to remove the strongly adherent bacteria. This bacterial solution suspension was diluted serially (10X; 100X; 1000X) and plated on tryptic soy agar plates as 10 µL aliquots, triplicate, and incubated for 14 h at 37 °C. Afterward, the colonies were counted to calculate the colony-forming units (CFUs).

For SEM analysis, the bacteria were fixed using 2.5% glutaraldehyde and 4% paraformaldehyde in PBS for 1h. After, they were dehydrated in a series of acetone solutions until reaching 100%, followed by rinsing with acetone plus HMDS (1: 1) and pure HMDS for 10 min each. The specimens were dried, platinum coated, and analyzed by SEM to observe bacterial morphology.

5.3.6 Fourier transform infrared spectrometry (FTIR)

FTIR measurements were made using a Perkin Elmer FTIR Imaging System, model Spotlight-400. The spectra were collected between 450 – 4000 cm^{-1}. The technique was used to analyze the functional groups on the polymeric fibers.

5.3.7 Mechanical test

Mechanical tensile testing was conducted using TA Instruments RSA-G2. Samples were cut into 10×30x0.5 mm rectangular strips and fixed in the clamps of the machine. The clamps were moved apart at a rate of 0.1 mm/s at room temperature to simulate biological conditions. The displacement rate was set to 10 mm/min at room temperature. From the stress-strain figures, the Young's modulus and the strain at the break were calculated.

5.3.8 Transmission electron microscopy (TEM)

TEM was performed using a JEM-1010, JEOL, Peabody, MA microscope operating at 80 kV. The powder of nanoceramics nHap and CNT was dispersed in 10 mL of ethanol with ultrasound aid, and a few drops were deposited in copper grids (300 mesh). The fibers were collected directly onto copper TEM grids (300 mesh) during the Electrospinning process and used an anti-static tweezer to hold the grid. RJS fibers were collected at the end of the process. The fibers present in the inner edges are more dispersive and are easier to collect in copper TEM grids (300 mesh).

It is worth mentioning that the fibers for RJS are impossible to collect during the process due to the airflow caused by the high motor speed.

6 CELLULAR ASSAYS

6.1 Cell viability, proliferation, and morphology

The biological activity was analyzed using Human dermal fibroblasts (HDF, CC-2509 - Lonza) and Human osteoblast cells (hOB - Promocell C-12720) according to the experimental study.

HDF cells were cultured using Dulbecco's Modified Eagle Medium (DMEM, Sigma Aldrich) supplemented with 10% of fetal bovine serum (FBS, Hyclone, Logan, UT), and 1% of penicillin/streptomycin (P/S, Sigma Aldrich). The growth medium utilized for hOB was Osteoblast Basal Medium (OBM, Promocell GmbH C27015), with 1% P/S, and Supmix/Osteoblast (Promocell GmbH C39615). The cell culture was maintained in a 37°C, humidified, 5% CO_2 at 95% air environment, and the culture medium was changed every 3 days of culture.

MTS (CellTiter 96® AQueous One Solution Cell Proliferation Assay, G3581; Promega Corporation, Fitchburg, WI, USA) assay was used to determine the cell viability and proliferation.

For cell viability analysis, the 20.000 cells/cm^2 were seeded onto the sterilized sample in each well of a 24-tissue culture well-plate and were then incubated under standard cell culture conditions. After 24h, the MTS reagent (1:5 ratio with cell culture media) was added to each well and set for 4h. Absorbance from each well was measured by a SpectraMax M3 (MT05412) at 490 nm, and a color change from pink to dark brown was seen. A standard curve was created with a known number of cells to correlate absorbance to cell numbers.

For cell proliferation assay, the hOB cells were analyzed after 7, 14, and 21 days of culture. For this, the cells were seeded at 5,000 cells/cm^2. The culture medium was changed every two days. The MTS reagent was added to each well and incubated for 4 hours on the measurement day. Absorbance from each well was measured. Results were normalized by subtracting the values measured for the samples from the value of a comparable blank solution.

The geometry of a scaffold can control the cells' behavior and morphology, so an analysis of the cell morphology was performed on the PCL scaffolds. The hOB cells were seeded at 20.000 cells cm^2 onto the sterilized sample for 24h. Cultured hOB cells were fixed using 2.5% glutaraldehyde and 4% paraformaldehyde in PBS for 1 hour. After, they were dehydrated in a series of acetone solutions until reaching 100%, followed by rinsing with acetone plus HMDS (1:1) and pure HMDS for 10 minutes each. The specimens were dried, platinum coated, and analyzed by SEM to observe the cell morphology.

6.2 Alkaline phosphatase assay

Alkaline phosphatase (ALP) is an enzyme produced by osteoblasts (bone-forming cells) to release phosphate groups to form calcium phosphate in the bone. A BioAssay QuantiChrom™ Alkaline Phosphatase Assay Kit (DALP-250) was used to determine serum ALP activity's colorimetric kinetic determination.

The polymeric scaffolds were set into 24-well microplates and seeded with 5,000 cells/cm^2 hOB cells in 1000 µL of growth media per well and were then incubated under standard cell culture conditions. After 7, 14, and 21 days of cell culture, the growth media was removed, and the scaffolds were lightly rinsed with PBS. Afterward, 500 µL of lysis solution (0.2 % Triton X – 100 (w/v) in distilled water) was applied to each scaffold and was agitated at 125 rpm, for 20 min (Innova 2000 platform shaker) at room temperature. The 50µL of lysate was transferred to individual wells of a new 96-well microplate.

The working solution was prepared by mixing 200 µL of the assay buffer, 5 µL of an acetate solution (final 5 mM), and 2 µL of the p-nitrophenyl phosphate liquid substrate (10 mM). An aliquot of 150µL of the alkaline phosphatase reaction solution was administered to the individual lysate solutions and homogenized by pipette. The final reaction volume in the sample wells was 200 µL. 200 µL of distilled water (H2O) and 200 µL of a calibrator solution was applied in a separate well. The optical density was measured at 405 nm (t=0) and again after 4 minutes (t=4 minutes) on a plate reader. Results were normalized by subtracting the absorbance values of blank wells containing samples without any cells from those values measured for the samples.

6.3 Calcium deposition

For calcium deposition assay after 7, 14, and 21 days of cell culture, the cell-seeded scaffolds (5,000 cells/cm2 hOB) were washed three times using deionized water to remove calcium ions in the medium. Cells and the extracellular matrix were demineralized by adding 500 µm of 0.6M hydrochloric acid to each well and agitated at 125 rpm, for 4 h, on an Innova 2000 platform shaker at room temperature. Next, 500 µL of the resultant solution was extracted from each well and centrifuged individually at 12,000 rpm for 3 minutes at 4°C. Afterward, 5µL of the supernatants were collected and transferred to separate wells of a new 96-well microplate.

Enough working reagent by combining equal volumes of Reagent A and Reagent B was prepared, both supplied by the BioAssay Systems Calcium Assay Kit. Results were normalized by subtracting the absorbance values of blank wells containing samples without any cells from those values measured for the samples.

7 *IN VIVO* STUDIES

7.1 Isolation and culture of BMMSCs

MSCs were obtained from the bone marrow of the femurs of 4 male Wistar rats. The tibia and femur bone were extracted and cleaned three times with a PBS solution, 2.5% chlorhexidine, and 70% ethanol. Afterward, the species were rinsed three times during 15 min each with alpha minimum essential medium (a-MEM,

Gibco-Invitrogen) with 1% of P/S. Subsequently, the ends of the bones (epiphyses) were extracted, and the bone marrow was washed with a-MEM with 10% fetal bovine serum (FBS) and 1% P/S. The cells obtained were placed in a culture bottle and kept in an oven at 37ºC and 5% CO2 until confluence. The culture medium was changed after four days of culture and subsequently every three days until 80–90% confluence.

Before the surgery procedure, a part of the scaffolds group was seeded with BMMSCs. The BMMSCs were isolated using a 0.25% trypsin-EDTA solution (Sigma-Aldrich) and seeded onto the sterilized scaffold. Approximately $1x10^5$ cells were pipetted over the scaffold and kept in an oven at 37ºC and 5% CO_2 for 24h before implanted.

7.2 Surgical procedures

Forty-eight male rats (100 days of age, Rattus norvegicus Albinus; Wistar), weighing from 400 to 450g, were used. The experimental procedures were approved by the Animal Ethics Committee (CEUA, Protocol 07/2017) of the Institute of Science and Technology of the Campus of Sao Jose dos Campos/ UNESP. The animals were divided into four groups with six rats in each one: (I) group analyzed after 2 weeks, (II) group analyzed after 6 weeks, (III) the same as the group I but seeded with BMMSCs, and (IV) the same as group II but seeded with BMMSCs. The animals were weighed and anesthetized with an intramuscular injection with a solution of xylazine hydrochloride 5 mg/kg (Anasedan®—Vetbrands, Jacareí—Brazil), and a Ketamine Hydrochloride 75-95 mg/kg (Dopalen®—Vetbrands, Jacaréi—Brazil) solution. After anesthesia, the surgical sites were submitted to trichotomy and antisepsis with an iodized alcohol solution. Access to the calvaria of the animal was made through the incision in the skin. A critical bone defect was made with a steel trephine drill (5 mm in diameter) under abundant and continuous irrigation with a physiological solution, aimed at avoiding overheating due to the friction of the drills with the bone. The bone defect was filled with the PCL and PCL:nHap:CNT material for both techniques without or with BMMSCs. Finally, the skin was sutured with silk thread #4 (Ethicon/Johnson & Johnson). After surgery, an analgesic drug (sodium dipyrone monohydrate 150 mg/kg) was given subcutaneously every 8 h until 48 h

after surgery. Euthanasia was carried out after 2 and 6 weeks using an anesthetic overdose administered intramuscularly.

The surgery procedure can see in **Fig. 8**. The critical bone defect in calvaria was established as an efficient model to assess the potential for healing and new bone formation [107, 108]. Besides, using a 5 mm defect makes it possible to make two surgical areas per animal. Therefore, each animal may have defects resulting from the treatment and defect that will be the control. In this way, the number of animals used in the experiment is minimized, following the 3R's principle [109].

Figure 8: Surgical procedure.

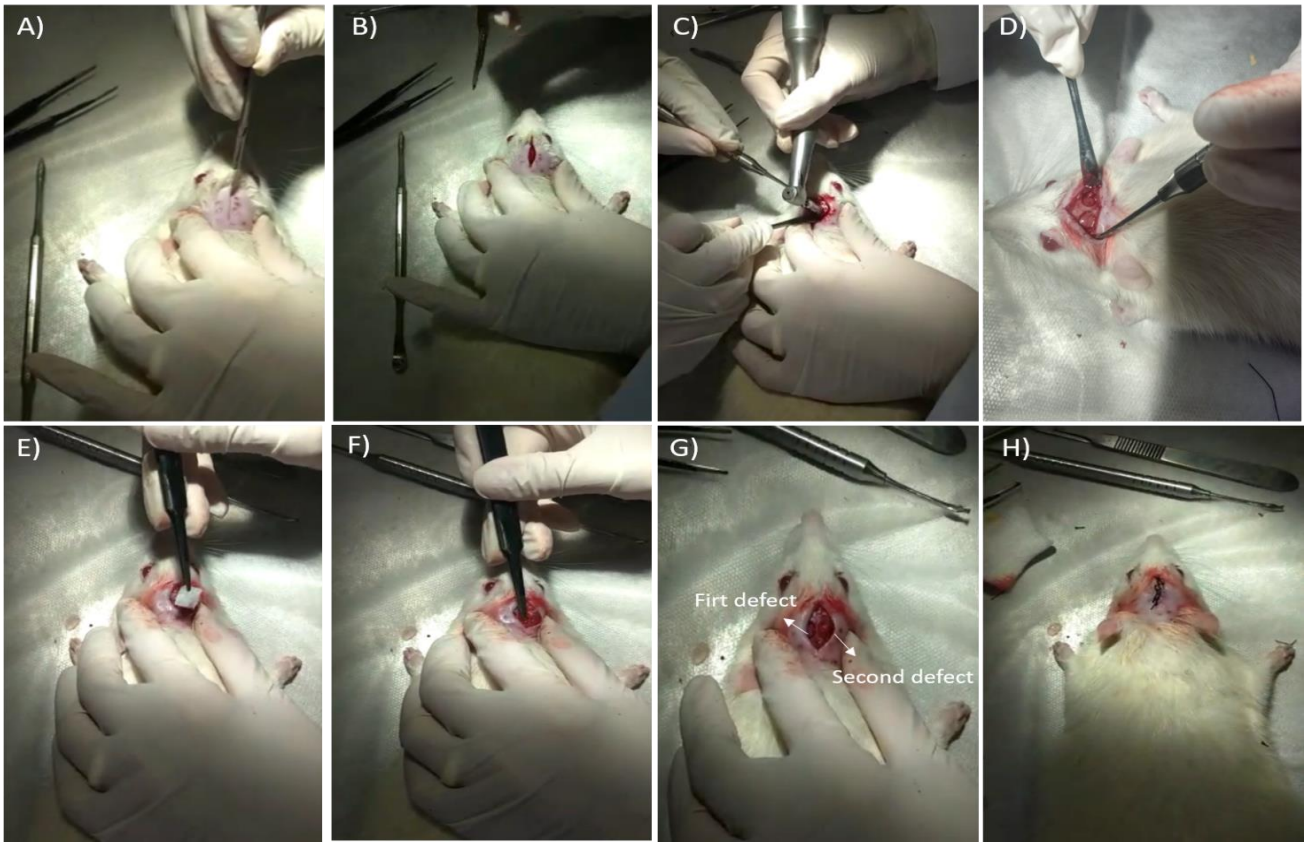

Note: (A-B) an incision with a scalpel blade number 15 to allow access to bone tissue. C) Defect being performed using a trephine. D) Critical defect of 5 mm in diameter. (E-G) filling the defect with the scaffold. (H) suture performed.
Source: The author.

7.3 Microtomography analyses (Micro-Ct)

The rat calvaria fragments were kept in 10% buffered formalin, pH 7.0. Before using microtomography, the fragments were washed and stored in 70% ethanol. The specimens then underwent three-dimensional (3D) microcomputer tomography

analyses using SkyScan 1174 (SkyScan, Kontich, Belgium). Tomographic images were acquired at 70 keV, and 702 μA, 360° rotation, and images were reconstructed using NRecon software (Bruker-Skyscan), and Dataviewer® (Skycan 2011 Version 1.4.4 64 Bit) software was used for the quantification of the bone formation CT-Analyzer® software (2003-11SkyScan, 2012 Bruker MicroCt Version 1.12.4.0) and the reconstruction of images. CT-Vol® software (SkyScan 7.0) was used. Thresholding was performed using a lower grey threshold limit of 50 and an upper grey threshold limit of 150. The following bone structural parameters were thus obtained: bone volume (BV), trabecular thickness (Tb.Th), trabecular number (Tb.N), and trabecular separation (Tb.Sp).

7.4 Histologic analysis

For all histology sections, the specimens were fixed in 10% buffered formaldehyde. Then the pieces were demineralized by immersion in an ethylenediaminetetraacetic acid solution (EDTA Titriplex III, Merck). After demineralization, the blocks were set in paraffin, and serial cross-sections of 5 μm thickness were obtained and stained with hematoxylin-eosin (HE). The histological sections were accessed blindly by a technician. The histomorphometric analysis was performed to quantify the area of new bone formation in three distinct regions of the defect: the lateral border and two in the center of the defect. Five sections containing the materials were digitized (5x) for each group, using Nikon Eclipse Ts2. After that, the new bone formation area was calculated using Image J (NIH) imaging software.

8 STATISTICAL ANALYSIS

All experiments were conducted in triplicate and were repeated at least three different times. The statistical differences between the mean values and for comparison between the samples were determined using one-way ANOVA followed with a Tukey's multiple comparison test. Differences were considered statistically significant at $p < 0.05$.

9 PROJECT PROPOSAL OVERVIEW

Figures 9 and 10 provide the project proposal overview schematic.

The first part of the project **(Fig. 9)** evaluated the two methods for producing PCL fibers, where different polymer concentrations were tested and analyzed before establishing the best material produced for each technique. Biomaterial characterization was evaluated by morphology, cytotoxicity, and its influence on the colonization of bacteria. Afterward, we use standardized materials for the second part of this project.

Fig. 10 represents the second part of the project, in which nHap and CNT nanoceramics were incorporated into the polymeric fibers (previously standardized in the first part of the project). Morphological analyzes and *in vitro* tests were performed. The best materials were established, and they were used in *in vivo* tests, in which scaffolds sown with BMMSCs were compared with acellular scaffolds.

Figure 9: Project proposal overview schematic 1.

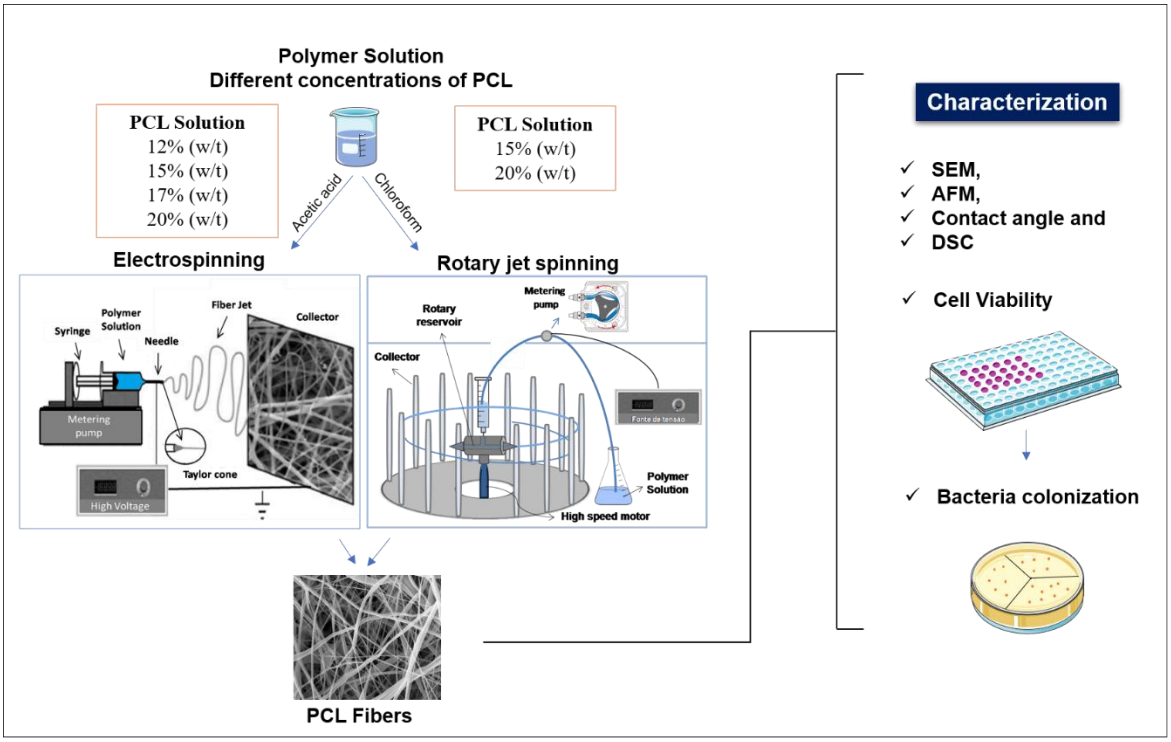

Source: The author.

Figure 10: Project proposal overview schematic 2.

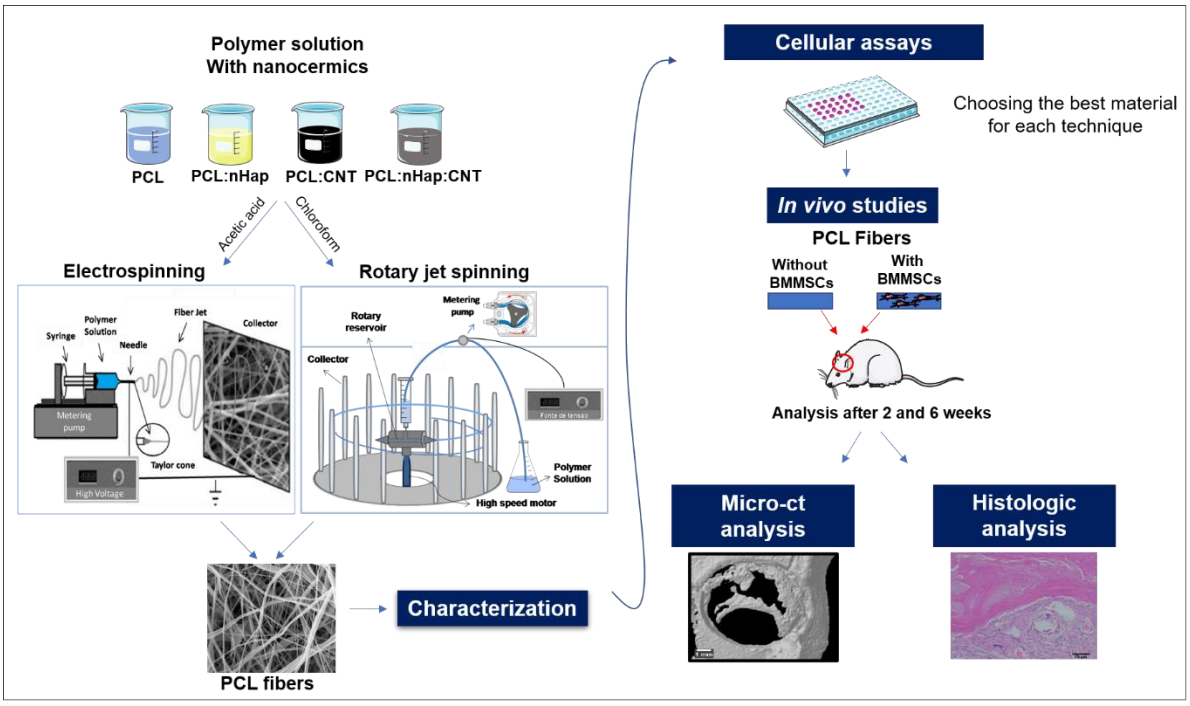

Source: The author.

10 RESULTS AND DISCUSSION

10.1 Paper 1 (Annex A).

M.M. Machado-Paula, M.A.F. Corat, M. Lancellotti, G. Mi, F.R. Marciano, M. L. Vega, A. A. Hidalgo, T.J. Webster, and A.O. Lobo. (2020). **A comparison between electrospinning and rotary-jet spinning to produce PCL fibers with low bacteria colonization. Materials Science and Engineering C**

10.2 Paper 2 (Annex B) (In phase for submission)

Mirian M. Machado-Paula, Marcus A.F. Corat, Luana M.R. Vasconcellos, Juliani C.R. Araújo, Gujie Mi, Paria Ghannadian, Tatiane V. Toniato, Fernanda R. Marciano, Thomas J. Webster and Anderson O. Lobo. **Rotary jet spun polycaprolactone/hydroxyapatite and carbon nanotubes scaffolds seeded with bone marrow mesenchymal stem cells increased bone neoformation.**

11 CONCLUSION

In this work, PCL fibers were produced with nHap and CNT incorporated, using two different manufacturing methods: electrospinning (ES) and rotary jet spinning (RJS). The results of this work suggest the following conclusions regarding the study of the scaffolds produced:

- ✓ Different morphologies were determined through the manufacturing method used, smooth fibers by electrospinning and rough fibers by rotary jet spinning
- ✓ PCL fibers showed good interaction with fibroblast cells
- ✓ The rough surface presented by the RJS fibers decreased the bacteria colonization
- ✓ PCL fibers at 17% obtained by ES and PCL at 15% obtained by RJS showed the best fiber characteristics than the others analyzed.
- ✓ The incorporation of nanoceramics in the polymeric fibers was carried out successfully
- ✓ PCL fibers with nHap: CNT nanoparticles showed the potential to stimulate biological activity in osteoblast cells compared to neat PCL.
- ✓ Two groups of each technique were determined for *in vivo* analysis: pure PCL and PCL: nHap: CNT, as they showed more significant osteoblast functions for both methods
- ✓ Increased bone formation occurred through the combination of three characteristics: the presence of nHap nanoparticles: CNT, morphology presented by the RJS fibers, and scaffold coating with BMMSCs.

This thesis shows that the choice of biomaterial and surface topography combined with cells of interest are key factors that can favor bone repair. These findings suggest that PCL: nHap: CNT scaffolds produced by RJS seeded with BMMSCs is a potentially advantageous material in the field of bone tissue regeneration.

REFERENCES

1. JUNQUEIRA, L. C.; CARNEIRO, J. **Histologia Básica**. 12. ed. Rio de Janeiro: Guanabara Koogan, 2013.

2. HOLLINGER, J. O.; KLEINSCHMIDT, J. C. The critical size defect as an experimental model to test bone repair materials. **Journal of Craniofacial Surgery**, v. 1, p. 60-68, 1990.

3. WANG, W.; YEUNG, K. W. K. Bone grafts and biomaterials substitutes for bone defect repair: A review. **Bioactive Materials**, v. 2, p. 224-247, 2017.

4. LONG JUNIOR, W. G. *et al*. Bone Grafts and Bone Graft Substitutes in Orthopaedic Trauma Surgery: A Critical Analysis. **JBJS**, v. 89, n. 3, p. 649-658, 2007.

5. HSIEH, J.-L. *et al*. Knockdown of toll-like receptor 4 signaling pathways ameliorate bone graft rejection in a mouse model of allograft transplantation. **Scientific Reports**, v. 7, 2017.

6. ZHANG, Y. *et al*. Promoted Proliferation of Hematopoietic Stem Cells Enabled by a Hyaluronic Acid/Carbon Nanotubes Antioxidant Hydrogel. **Macromolecular Materials and Engineering**, v. 304, n. 4, 2019.

7. ZHANG, Y. *et al*. Recent development of polymer nanofibers for biomedical and biotechnological applications. **Journal of Materials Science: Materials in Medicine**, v. 16, p. 933-946, 2005.

8. DHANDAYUTHAPANI, B. *et al*. Polymeric scaffolds in tissue engineering application: a review. ***International journal of polymer science***, v. 2011, 2011.

9. EATEMADI, A. *et al*. Nanofiber: Synthesis and biomedical applications. **Artificial cells, nanomedicine, and biotechnology**, v. 44, p. 111-121, 2016.

10. KHORSHIDI, S. *et al*. A review of key challenges of electrospun scaffolds for tissue-engineering applications. **Journal of tissue engineering and regenerative medicine**, v. 10, p. 715-738, 2016.

11. STOJANOVSKA, E. *et al*. A review on non-electro nanofibre spinning techniques. **RSC Advances,** v. 6, p. 83783-83801, 2016.

12. MELLADO, P. *et al*. A simple model for nanofiber formation by rotary jet-spinning. **Applied Physics Letters**, v. 99, 2011.

13. BADROSSAMAY, M. R. *et al*. Nanofiber Assembly by Rotary Jet-Spinning. **Nano Letters**, v. 10, p. 2257-2261, 2010.

14. HUANG, Z.-M. *et al*. A review on polymer nanofibers by electrospinning and their applications in nanocomposites. **Composites science and technology**, v. 63, p. 2223-2253, 2003.

15. BADROSSAMAY, M. R. *et al*. Engineering hybrid polymer-protein super-aligned nanofibers via rotary jet spinning. **Biomaterials**, v. 35, p. 3188-3197, 2014.

16. ROGALSKI, J. J.; BASTIAANSEN, C. W.; PEIJS, T. Rotary jet spinning review–a potential high yield future for polymer nanofibers. **Nanocomposites**, v. 3, p. 97-121, 2017.

17. ASGHARI, F. *et al*. Biodegradable and biocompatible polymers for tissue engineering application: a review. **Artificial cells, nanomedicine, and biotechnology,** v. 45, p. 185-192, 2017.

18. DWIVEDI, R. *et al*. Polycaprolactone as biomaterial for bone scaffolds: Review of literature. **Journal of Oral Biology and Craniofacial Research**, v. 10, p. 381-388, 2020.

19. TARABALLI, F. *et al*. Concise Review: Biomimetic Functionalization of Biomaterials to Stimulate the Endogenous Healing Process of Cartilage and Bone Tissue. **STEM CELLS Translational Medicine**, v. 6, p. 2186-2196, 2017.

20. YUAN, N.; REZZADEH, K. S.; LEE, J.C. Biomimetic Scaffolds for Osteogenesis. **Receptors Clin Investig**, v. 2, n. 3, p.1-10, 2015.

21. CALDWELL, K.; BERG, J. Nanoparticles as Interphase Modifi ers in Fiber Reinforced Polymeric Composites: A Critical Review. **Reviews of Adhesion and Adhesives**, v. 5, p. 1-54, 2017.

22.HARRISON, B. S.; ATALA, A. Carbon nanotube applications for tissue engineering. **Biomaterials**, v. 28, p. 344-353, 2007.

23. MITTAL, V. **Polymer nanotubes nanocomposites**: synthesis, properties and applications. [*s.l*]: John Wiley & Sons, 2014.

24. TURON, P. *et al.* Biodegradable and biocompatible systems based on hydroxyapatite nanoparticles. **Applied Sciences**, v. 7, 2017.

25. ZAKARIA, S. M. *et al.* Nanophase hydroxyapatite as a biomaterial in advanced hard tissue engineering: a review. **Tissue Engineering Part B: Reviews**, v. 19, p. 431-441, 2013.

26. MAGLIONE, M. *et al*. In vivo evaluation of chitosan-glycerol gel scaffolds seeded with stem cells for full-thickness mandibular bone regeneration. **Journal of oral science**, v. 59, p. 225-232, 2017.

27. Stanovici, J. *et al*. Bone regeneration strategies with bone marrow stromal cells in orthopaedic surgery. **Current Research in Translational Medicine**, v. 64, p. 83-90, 2016.

28. TROUNSON, A. *et al*. Clinical trials for stem cell therapies. **BMC medicine**, v. 9, 2011.

29. CAPLAN, A. I. Adult mesenchymal stem cells for tissue engineering versus regenerative medicine. **Journal of cellular physiology**, v. 213, p. 341-347, 2007.

30. MISTRY, A. S.; MIKOS, A. G. **in Regenerative medicine II 1-22**. [*s.l*]: Springer, 2005.

31. HAN, Y. *et al*. Mesenchymal Stem Cells for Regenerative Medicine. **Cells**, v. 8, 2019.

32. KARGOZAR, S. *et al*. Acceleration of bone regeneration in bioactive glass/gelatin composite scaffolds seeded with bone marrow-derived mesenchymal stem cells over-expressing bone morphogenetic protein-7. **Materials Science and Engineering: C**, v. 75, p. 688-698, 2017.

33. WESTHAUSER, F. *et al*. Three-dimensional polymer coated 45S5-type bioactive glass scaffolds seeded with human mesenchymal stem cells show bone formation in vivo. **Journal of Materials Science: Materials in Medicine**, v. 27, 2016.

34. ZHANG, R. *et al*. Acceleration of bone regeneration in critical-size defect using BMP-9-loaded nHA/ColI/MWCNTs scaffolds seeded with bone marrow mesenchymal stem cells. **BioMed research international**, v. 2019, 2019.

35. MACHADO-PAULA, M. et al. A comparison between electrospinning and rotary-jet spinning to produce PCL fibers with low bacteria colonization. ***Materials Science and Engineering: C***, v. 111, 2020.

36. FloreNCIO-SILVA, R. *et al*. Biology of bone tissue: structure, function, and factors that influence bone cells. **BioMed research international**, v. 2015, 2015.

37. MARIEB, E. N.; ZAO, P. Z. **The skeletal system.** [*s.l.*]: Benjamin/Cummings, 1992.

38. WIKIMEDIA. **Bone cells**. Disponível em: https://upload.wikimedia.org/wikipedia/commons/b/b6/604_Bone_cells.jpg. Acesso em: 27 jan. 2020.

39. ART, S.M. Servier Medical Art by Servier is licensed under a Creative Commons Attribution 3.0 Unported License.

40. Clarke, B. Normal bone anatomy and physiology. **Clinical journal of the American Society of Nephrology**, v. 3, p. S131-S139, 2008.

41. GONG, T. *et al*. Nanomaterials and bone regeneration. **Bone research**, v. 3, 2015.

42. ROBLING, A. G.; CASTILLO, A. B.; TURNER, C. H. Biomechanical and molecular regulation of bone remodeling. **Annu. Rev. Biomed. Eng***.,* v. 8, p. 455-498, 2006.

43. SIMS, N. A.; GOOI, J. H. Bone remodeling: Multiple cellular interactions required for coupling of bone formation and resorption. **Seminars in cell & developmental biology**, v. 19, n. 6, p. 444-451, 2008.

44. GERSTENFELD, L. C. *et al.* Fracture healing as a post-natal developmental process: Molecular, spatial, and temporal aspects of its regulation. **Journal of cellular biochemistry**, v. 88, p. 873-884, 2003.

45. FROST, H. The biology of fracture healing: an overview for clinicians. Part I. **Clinical orthopaedics and related research**, v. 248, p. 283-293, 1989.

46. SCHINDELER, A. *et al.* Bone remodeling during fracture repair: The cellular picture. **Seminars in cell & developmental biology**, v. 19, n. 6,p. 459-466, 2008.

47. TAKAYANAGI, H. Osteoclast biology and bone resorption. **Primer on the Metabolic Bone Diseases and Disorders of Mineral Metabolism**, v. 4, p. 46-53, 2018.

48. RAISZ, L. G. Physiology and pathophysiology of bone remodeling. **Clinical chemistry**, v. 45, p. 1353-1358, 1999.

49. SIDDIQUI, J. A.; PARTRIDGE, N. C. Physiological bone remodeling: systemic regulation and growth factor involvement. **Physiology**, v. 31, p. 233-245, 2016.

50. NAVARRO, M. *et al.* Biomaterials in orthopaedics. **Journal of the Royal Society Interface**, v. 5, p. 1137-1158, 2008.

51. MARQUIS, M.-E. *et al*. Bone cells-biomaterials interactions. **Front Biosci**, v. 14, p. 1023-1067, 2009.

52. BASHA, R.Y.; DOBLE, M. Design of biocomposite materials for bone tissue regeneration. **Materials Science and Engineering: C**, v. 57, p. 452-463, 2015.

53. NANDI, S. *et al*. Orthopaedic applications of bone graft & graft substitutes: a review. **Indian Journal of Medical Reseach**, v. 132, p. 15-30, p. 2010.

54. DAMIEN, C. J.; PARSONS, J. R. Bone graft and bone graft substitutes: a review of current technology and applications. **Journal of applied biomaterials : an official journal of the Society for Biomaterials**, v. 2, p. 187-208, 1991.

55. QIAO, W. *et al*. Contribution of the in situ release of endogenous cations from xenograft bone driven by fluoride incorporation toward enhanced bone regeneration. **Biomaterials Science**, v. 6, p. 2951-2964, 2018.

56. BRACEY, D. N. *et al*. A porcine xenograft-derived bone scaffold is a biocompatible bone graft substitute: An assessment of cytocompatibility and the alpha-Gal epitope. **Xenotransplantation**, v. 26, 2019.

57. CHRISTMAN, K. L. Biomaterials for tissue repair. **Science**, v. 363, p. 340-341, 2019.

58. EVANS, N. D.; GENTLEMAN, E.; POLAK, J. M. Scaffolds for stem cells. **Materials Today**, v. 9, p. 26-33, 2006.

59. SEAL, B.; OTERO, T.; PANITCH, A. Polymeric biomaterials for tissue and organ regeneration. **Materials Science and Engineering: R: Reports**, v. 34, p. 147-230, 2001.

60. CHAN, G.; MOONEY, D.J. New materials for tissue engineering: towards greater control over the biological response. ***Trends in biotechnology***, v. 26, p. 382-392, 2008.

61. VUNJAK-NOVAKOVIC, G.; KAPLAN, D. L. Tissue engineering: the next generation. **Tissue engineering**, v. 12, p. 3261-3263, 2006.

62. REZWAN, K. *et al*. Biodegradable and bioactive porous polymer/inorganic composite scaffolds for bone tissue engineering. **Biomaterials**, v. 27, p. 3413-3431, 2006.

63. BARNES, C.P. *et al*. Nanofiber technology: designing the next generation of tissue engineering scaffolds. **Advanced drug delivery reviews**, v. 59, p. 1413-1433, 2007.

64. DESAI, T. Micro-and nanoscale structures for tissue engineering constructs. **Medical engineering & physics**, v. 22, p. 595-606, 2000.

65. BLACK, C.R.M. *et al*. Bone Tissue Engineering. **Current Molecular Biology Reports**, v. 1, p. 132-140, 2015.

66. FERREIRA, L. *et al*. New opportunities: the use of nanotechnologies to manipulate and track stem cells. **Cell stem cell**, v. 3, p. 136-146, 2008.

67. KANJWAL, M. A. *et al*. Functionalization of electrospun titanium oxide nanofibers with silver nanoparticles: strongly effective photocatalyst. **International Journal of Applied Ceramic Technology**, v. 7, 2010.

68. BALANI, K. *et al*. Plasma-sprayed carbon nanotube reinforced hydroxyapatite coatings and their interaction with human osteoblasts in vitro. **Biomaterials**, v. 28, p. 618-624, 2007.

69. CHOW, E. K. *et al.* Nanodiamond therapeutic delivery agents mediate enhanced chemoresistant tumor treatment. **Science translational medicine**, v. 3, p.73ra21-73ra21, 2011.

70. Aryal, S. *et al.* Multi-walled carbon nanotubes/TiO 2 composite nanofiber by electrospinning. **Materials Science and Engineering: C**, v. 28, p. 75-79, 2008.

71. MATASSI, F. *et al.* New biomaterials for bone regeneration. **Clinical cases in mineral and bone metabolism : the official journal of the Italian Society of Osteoporosis, Mineral Metabolism, and Skeletal Diseases**, v. 8, p. 21-24, 2011.

72. MALIKMAMMADOV, E. *et al*. PCL and PCL-based materials in biomedical applications. **Journal of Biomaterials Science, Polymer Edition**, v. 29, p. 863-893, 2018.

73. SBYRNES321. Polycaprolactone (PCL) repeating unit. **Wikimedia**, 2012. Disponível em: https://commons.wikimedia.org/wiki/File:Polycaprolactone_structure.png. Acesso em: 10 fev. 2020.

74. HOSSEINKHANI, H. *et al*. Development of 3D in vitro platform technology to engineer mesenchymal stem cells. **Int. J. Nanomed**, v. 7, 2012.

75. VALIZADEH, A. *et al*. Preparation and characterization of novel electrospun poly(-caprolactone)-based nanofibrous scaffolds. **Artif Cells Nanomed Biotechnol**, v. 44, p. 504-509, 2016.

76. ASGHARI, F. *et al*. Biodegradable and biocompatible polymers for tissue engineering application: a review. **Artificial cells, nanomedicine, and biotechnology**, v. 45, p. 185-192, 2017.

77. RAY, S. S. *et al.* A comprehensive review: electrospinning technique for fabrication and surface modification of membranes for water treatment application. **RSC Advances**, v. 6, p. 85495-85514, 2016.

78. GONZALEZ, G. M. *et al.* Production of Synthetic, Para-Aramid and Biopolymer Nanofibers by Immersion Rotary Jet-Spinning. **Macromolecular Materials and Engineering**, v. 302, 2017.

79. SAHITHI, K. *et al*. Polymeric composites containing carbon nanotubes for bone tissue engineering. **International Journal of Biological Macromolecules**, v. 46, p. 281-283, 2010.

80. GUTIÉRREZ-HERNÁNDEZ, J. M. *et al*. In vitro evaluation of osteoblastic cells on bacterial cellulose modified with multi-walled carbon nanotubes as scaffold for bone regeneration. **Materials Science and Engineering: C**, v. 75, p. 445-453, 2017.

81. RAMESH, N.; MORATTI, S. C.; DIAS, G. J. Hydroxyapatite–polymer biocomposites for bone regeneration: A review of current trends. **Journal of Biomedical Materials Research Part B: Applied Biomaterials**, v. 106, p. 2046-2057, 2018.

82. MICULESCU, F. *et al*. Progress in hydroxyapatite–starch based sustainable biomaterials for biomedical bone substitution applications. **ACS Sustainable Chemistry & Engineering**, v. 5, p. 8491-8512, 2017.

83. OLIVIER, V.; FAUCHEUX, N.; HARDOUIN, P. Biomaterial challenges and approaches to stem cell use in bone reconstructive surgery. **Drug Discovery Today**, v. 9, p. 803-811, 2004.

84. WEI, G.; MA, P. X. Structure and properties of nano-hydroxyapatite/polymer composite scaffolds for bone tissue engineering. **Biomaterials**, v. 25, p. 4749-4757, 2004.

85. RUJITANAPANICH, S.; KUMPAPAN, P.; WANJANOI, P. Synthesis of Hydroxyapatite from Oyster Shell via Precipitation. **Energy Procedia**, v. 56, p. 112-117, 2014.

86. LOBO, A. O. *et al*. Increasing mouse embryonic fibroblast cells adhesion on superhydrophilic vertically aligned carbon nanotube films. **Materials Science and Engineering: C**, v. 31, p. 1505-1511, 2011.

87. (https://creativecommons.org/licenses/by/4.0), V.N.C.B.

88. (https://creativecommons.org/licenses/by-sa/3.0), E.W.C.B.-S.

89. KHAN, W. S. *et al*. An osteoconductive, osteoinductive, and osteogenic tissue-engineered product for trauma and orthopaedic surgery: how far are we? **Stem cells international**, v. 2012, 2012.

90. CHIU, R. C. J. Bone-Marrow Stem Cells as a Source for Cell Therapy. **Heart Failure Reviews**, v. 8, p. 247-251, 2003.

91. SQUILLARO, T.; PELUSO, G.; GALDERISI, U. Clinical trials with mesenchymal stem cells: an update. **Cell transplantation**, v. 25, p. 829-848, 2016.

92. SALEM, H.K.; THIEMERMANN, C. Mesenchymal stromal cells: current understanding and clinical status. **Stem cells**, v. 28, p. 585-596, 2010.

93. MÉNDEZ-FERRER, S.; SCADDEN, D.T.; SÁNCHEZ-AGUILERA, A. Bone marrow stem cells: current and emerging concepts. **Annals of the New York Academy of Sciences**, v. 1335, p. 32-44, 2015.

94. WEI, X. *et al*. Mesenchymal stem cells: a new trend for cell therapy. **Acta Pharmacologica Sinica**, v. 34, p. 747-754, 2013.

95. CHEN, L. *et al*. Paracrine factors of mesenchymal stem cells recruit macrophages and endothelial lineage cells and enhance wound healing. **PloS one**, v. 3, 2008.

96. ANTUNES, E. *et al*. Thermal annealing and electrochemical purification of multi-walled carbon nanotubes produced by camphor/ferrocene mixtures. **Journal of nanoscience and nanotechnology**, v. 10, p. 1296-1303, 2010.

97. RAMOS, S. *et al*. Influence of polar groups on the wetting properties of vertically aligned multi-walled carbon nanotube surfaces. **Theoretical Chemistry Accounts**, v. 130, p. 1061-1069, 2011.

98. RAMOS, S. C. *et al*. Wettability control on vertically-aligned multi-walled carbon nanotube surfaces with oxygen pulsed DC plasma and CO2 laser treatments. **Diamond and Related Materials**, v. 19, p. 752-755, 2010.

99. KHANG, D. *et al*. Enhanced fibronectin adsorption on carbon nanotube/poly(carbonate) urethane: independent role of surface nano-roughness and associated surface energy. **Biomaterials**, v. 28, p. 4756-4768, 2007.

100. YOUNG, T. III. An essay on the cohesion of fluids. **Philosophical Transactions of the Royal Society of London**, v. 95, p. 65-87, 1805.

101. VAN OSS, C. J.; GOOD, R. J.; CHAUDHURY, M. K. The role of van der Waals forces and hydrogen bonds in “hydrophobic interactions” between biopolymers and low energy surfaces. **Journal of Colloid and Interface Science**, v. 111, p. 378-390, 1986.

102. FLAHAUT, E. *et al.* Investigation of the cytotoxicity of CCVD carbon nanotubes towards human umbilical vein endothelial cells. **Carbon**, v. 44, p. 1093-1099, 2006.

103. SCHAKENRAAD, J. M. *et al.* Thermodynamic aspects of cell spreading on solid substrata. **Cell biophysics**, v. 13, p. 75-91, p. 1988.

104. LIU, C. *et al.* Reduction of bacterial adhesion on modified DLC coatings. **Colloids and Surfaces B: Biointerfaces**, v. 61, p. 182-187, 2008.

105. SCHNEIDER, R. P. Conditioning Film-Induced Modification of Substratum Physicochemistry—Analysis by Contact Angles. **Journal of Colloid and Interface Science**, v. 182, p. 204-213, 1996.

106. WANG, J. *et al*. Bacterial repellence from polyethylene terephthalate surface modified by acetylene plasma immersion ion implantation–deposition. **Surface and Coatings Technology**, v. 186, p. 299-304, 2004.

107. BOSCH, C.; MELSEN, B.; VARGERVIK, K. Importance of the critical-size bone defect in testing bone-regenerating materials. **The Journal of craniofacial surgery**, v. 9, p. 310-316, 1998.

108. VAJGEL, A. *et al*. A systematic review on the critical size defect model. **Clinical oral implants research**, v. 25, p. 879-893, 2014.

109. GUHAD, F. Introduction to the 3Rs (refinement, reduction and replacement). **Journal of the American Association for Laboratory Animal Science**, v. 44, p. 58-59, 2005.

ANNEX A – PAPER 1

Materials Science & Engineering C 111 (2020) 110706

Contents lists available at ScienceDirect

Materials Science & Engineering C

journal homepage: www.elsevier.com/locate/msec

A comparison between electrospinning and rotary-jet spinning to produce PCL fibers with low bacteria colonization

M.M. Machado-Paula[a,b], M.A.F. Corat[c], M. Lancellotti[d], G. Mi[b], F.R. Marciano[b,e], M.L. Vega[f], A.A. Hidalgo[f], T.J. Webster[b,*], A.O. Lobo[b,g,**]

[a] Programa de Pós-graduação em Engenharia Biomédica, Universidade do Vale do Paraíba, São Jose dos Campos, SP 12244 – 000, Brazil
[b] Nanomedicine Laboratories, Department of Chemical Engineering, Northeastern University, Boston, MA 02115, USA
[c] Multidisciplinary Center for Biological Research, Universidade Estadual de Campinas, Campinas, SP 13083-877, Brazil
[d] Laboratory of Biotechnology, Faculty of Pharmaceutic Sciences, Universidade Estadual de Campinas, Campinas, SP 13083-877, Brazil
[e] Department of Physics, UFPI - Federal University of Piaui, 64049-550 Teresina, PI, Brazil
[f] Materials and Bionanotechnology Laboratory, Department of Physics, UFPI - Federal University of Piaui, 64049-550 Teresina, PI, Brazil
[g] LIMAV-Interdisciplinary Laboratory for Advanced Materials, Department of Materials Engineering, UFPI - Federal University of Piaui, 64049-550 Teresina, PI, Brazil

ARTICLE INFO

Keywords:
Poly ε-caprolactone
Electrospinning
Rotary jet spinning
Bacteria colonization
Cytotoxicity
Nanotechnology

ABSTRACT

One of the important components in tissue engineering is material structure, providing a model for fixing and the development of cells and tissues, which allows for the transport of nutrients and regulatory molecules to and from cells. The community claims the need for new materials with better properties for use in the clinic. Poly (ε-caprolactone) (PCL) is a biodegradable polymer, semi crystalline, with superior mechanical properties and has attracted an increasing interest due to its usefulness in various biomedical applications. Herein, two different methods (electrospinning versus rotary jet spinning) with different concentrations of PCL produced ultra thin-fibers each with particular characteristics, verified and analyzed by morphology, wettability, thermal and cytotoxicity features and for bacteria colonization. Different PCL scaffold morphologies were found to be dependent on the fabrication method used. All PCL scaffolds showed greater mammalian cell interactions. Most impressively, rotary-jet spun fibers showed that a special rough surface decreased bacteria colonization, emphasizing that no nanoparticle or antibiotic was used; maybe this effect is related with physical (scaffold) and/or biological mechanisms. Thus, this study showed that rotary jet spun fibers possess a special topography compared to electrospun fibers to reduce bacteria colonization and present no cytotoxicity when in contact with mammalian cells.

1. Introduction

Faced with a sensitive biological system as complex as the human body, materials used as scaffolds in tissue engineering have been diverse and often challenging to create [1–3]. One of the most important components in tissue engineering is scaffold structure, providing a model for supporting cell and tissue attachment, growth, and extracellular matrix formation [2,4]. Thus, the choice of the biomaterial used is fundamental to allow cells to form a suitable tissue [5,6]. It becomes important to manufacture new materials with better physical and chemical features than those currently used [4,7]. Desirable conditions for the production of scaffolds involve topographical features at the micro/nanoscale which allows for the exchange of signals between cell-to-cell and environment interactions in order to restore tissue function [8,9].

Polymeric fibers need to resemble the fibrous structures of the native extracellular matrix (ECM) and, as such, have attracted significant attention in tissue engineering. Poly (ε-caprolactone) (PCL) has been widely used in the tissue engineering field for its biocompatibility and biodegradability, and its semi crystalline nature provides superior mechanical properties compared to other polymers at a relatively inexpensive price. This polymer is commonly used in drug delivery, medical implants, and as dental splints. In additional, PCL has been approved by the United States Food and Drug Administration (FDA) [10,11].

Among the various techniques commonly used to generate ultrathin biologically-inspired PCL fibers, electrospinning (ES) has been widely studied and, more recently, rotary jet spinning (RJS) was

* Corresponding author.
** Correspondence to: A. O. Lobo, Nanomedicine Laboratories, Department of Chemical Engineering, Northeastern University, Boston, MA 02115, USA.
E-mail addresses: th.webster@northeastern.edu (T.J. Webster), lobo@ufpi.edu.br (A.O. Lobo).

https://doi.org/10.1016/j.msec.2020.110706
Received 10 September 2019; Received in revised form 7 January 2020; Accepted 28 January 2020
Available online 16 March 2020
0928-4931/

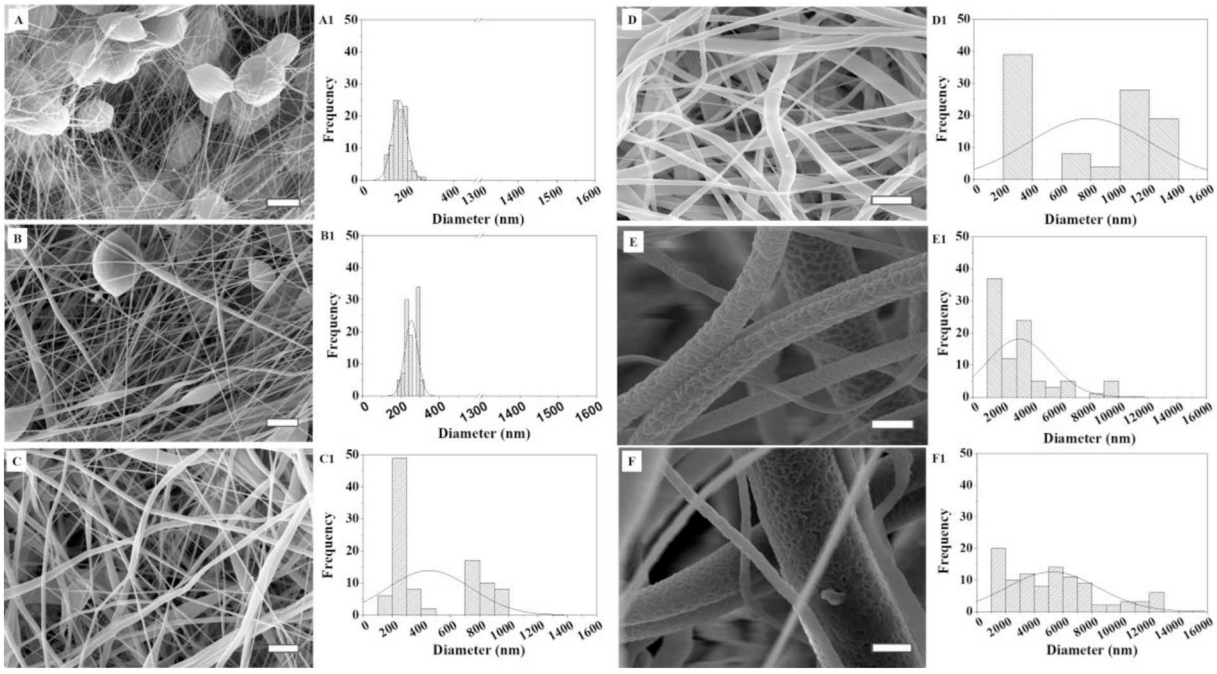

Fig. 1. Micrographs and corresponding histograms of the fiber diameter distribution collected using electrospun (A–D) and rotary jet spun (E–F) PCL fibers. Micrographs obtained by electrospun fibers correspond to PCL at 12% (A), 15% (B), 17% (C) and 20% (D) (*w/v*), and by rotary jet spun fibers at 15% (E) and 20% (F) (w/v). Distribution of PCL diameters calculated by ImageJ respectively is shown (A1-F1). Scale bars = 5 μm.

introduced. Comparing these two methods, ES is more popular and is a relatively cost-effective method to produce ultrathin fibers by electrically charging the polymer. Tri-dimensional biologically-inspired fibrous structures mimicking the natural ECM can be easily fabricated with this process [12,13]. Several researchers have shown that electrospun fibrous scaffolds allow for a better, more natural, environment for cell attachment and proliferation, since they mimic the topography of the ECM [10,13–15].

ES uses an electric field to create a potential difference between a grounded collector and a polymer solution, in which the liquid is forced through a capillary needle. As the voltage increases, the like charged electrostatic force overcomes the surface tension of the liquid causing the formation of a jet, called a Taylor cone. Lastly, in the path to the collector, the solvent evaporates producing the fiber [10,13,16]. Despite the popularity and the versatility of ES, it requires a high voltage electric field which depends on the conductivity of the solution, and also has imprecise control over fiber orientation and has a low production rate, limiting its wide-spread application [17,18].

In contrast, RJS is a simple method as it uses high-speed rotation for producing aligned fibers. This technique does not require a conductive solution but a low boiling point of the solvent is necessary. The polymer fiber diameter and porosity can be controlled by varying nozzle geometry, rotation speed, and polymer solution properties. Furthermore, RJS provides higher production rates compared to those fabricated via ES, 5 μL of solution per min^{-2} compared to 1 mL of solution per min^{-1} per nozzle, respectively [17–19]. Although this technique is a relatively new, there have already been several very promising studies on RJS for biomedical applications [17,18,20].

The RJS system consists of a reservoir with two opposite poles attached to the shaft of a motor with controllable rotation speed. When the reservoir spins on its axis, it ejects a polymeric jet from the holes by centrifugal force. The solvent evaporates while the jet travels in a spiral forming really thin fibers [19,21].

RJS and ES are methodologies that may produce different materials with a particular characteristic in their structure, in what may bring insights to resolve problems found in the biomedical engineering field of implants.

One of the problems found in biomedical engineering is bacterial contamination on materials, what is still an unresolved problem associated with implanted medical implants, especially long-term ones [22–25]. Gram-negative bacteria are naturally resistant to numerous treatments and are difficult to kill due to their robust and hydrophobic outer lipopolysaccharide membrane that helps to prevent the flow of antibiotics or drugs into the cell. Moreover, due to extensive antibiotic use, Gram-positive *Staphylococcus aureus* have evolved into a methicillin-resistant strain, which can overcome other classes of antibiotic treatment [25–29]. In fact, recently, the Centers for Disease Control predicted that deaths caused by the emergence of antibiotic-resistant bacteria will surpass cancer in the coming decades [30].

Furthermore, persistent bacteria colonization of surgical implants is associated with bacteria biofilm formation at the implantation site, which consists of a matrix of proteins, polysaccharides, and DNA. Bacterial adhesion, growth, and subsequent biofilm formation on surfaces are particularly resistant toward the body's defense mechanisms and antibiotic treatments, which can cause implant rejection [31,32].

Reduced contact of microorganisms with an implant might prevent extensive bacteria proliferation on the surface and allow the immune system to clear such bacteria. Nature gives us many examples of micro/nanotopographies that protect surfaces from microorganism colonization, and developing polymers with similar properties to resist bacteria adhesion has been a growing area of research [33–35]. This goal may be reached by modulating polymer processing parameters, such as: hydrophobicity, surface charge, chemical composition, surface roughness, topography, or physical configuration [23,36].

Herein, we performed a clarifying comparison between ES and RJS to produce fibers using different concentrations of PCL, and we provide the first report to compare both the manufacturing process and their influence on bacterial colonization (without using antibiotics or any chemical treatment).

2. Results and discussion

Different morphologies and diameters resulted when different PCL concentrations and PCL spinning techniques were used. ES fibers were

smoother at lower polymer concentrations such as 12% and 15% than 17% and 20% PCL. However, the RJS fibers presented higher roughness independent of concentration (15%, Fig. 1E and 20%, Fig. 1F). Regarding the average thickness, we observed that the ES fibers presented diameters as 102 ± 26 nm with 12% of PCL (Fig. 1A1), 182 ± 30 nm with 15% (Fig. 1B1), 124 ± 50 nm and 700 ± 98 nm with 17% (Fig. 1C1) and 200 to 1390 nm with 20% (Fig. 1D1). Curiously, the fiber diameter increased with higher concentrations of PCL. However, PCL at 20% (Fig. 1D) showed irregular fibers varying from nano to micro scales, but PCL at 17% (Fig. 1C) presented a better morphology with low variation.

Comparatively, RJS fibers at 15% showed thicker fibers at the microscale, and presented more nanocale roughness (porous) than the ES fibers. Regarding roughness, we have seen RJS fibers as a special attractive roughness since they may allow for better cell adhesion due to greater surface area [37]. In addition, PCL at 15% presented more similar fibers with structures at the micro scale than PCL at 20% with an average diameter of around 1 ± 0.99 µm and 1 ± 0.12 µm, respectively. In summary, the PCL fibers at 17% obtained by ES and PCL fibers at 15% obtained by RJS showed the best nano-rough fiber characteristics than the others analyzed.

The morphology of the fibers was investigated using AFM, Fig. 2. Fiber images using PCL 15% ES and RJS, respectively, are shown in Fig. 2(A) and (B) using the same scale. Different fiber conformation was evident when comparing both figures. The ES technique formed several fibers in the same area. When performing statistical analysis of the images, it is important to pay attention to the fact that conventional Root Mean Square σ_{RMS} Roughness does not represent the real value of fiber roughness. This artifact is caused by contributions from fiber roughness, substrate roughness and fibers overlapping [38]. To obtain the roughness of the fibers, it is necessary to calculate the Effective Root Mean Square $\sigma_{RMS\ EFF}$ Roughness [38,39]. This $\sigma_{RMS\ EFF}$ evaluates the fiber roughness eliminating contributions from other image aspects, when possible. Results showed that $\sigma_{RMS\ EFF}$ was 4 times lower than σ_{RMS} in Fig. 2a and b, for both cases. However, $\sigma_{RMS\ EFF}$ values showed a difference of 100 nm, being higher for the ES image. At first sight, the RJS image seems to be more rough, Fig. 2a and b; this is an artifact produced by the impossibility of isolating a single fiber on Fig. 2c and d using image processing and that the calculated $\sigma_{RMS\ EFF}$ was affected by the overlapping of several fibers. For Fig. 2c and d, single fibers are shown for each image. As ES and RJS produces fibers of different sizes, different scales are necessary to isolate the single fibers. A single RJS fiber had a diameter around 9 µm, while a single ES fiber had a diameter around 2 µm. Although using different scales it is possible to get $\sigma_{RMS\ EFF}$ of a single fiber, the results showed that RJS fibers have higher Effective Root Mean Square Roughness.

Furthermore, the influence of wettability and surface energy of the material show important characteristics that control bacterial adhesion [40]. Some researchers have been building natural self-cleaning surfaces which present super-hydrophobic features as lotus leaves [35,41]. Despite those samples displaying better morphology as mentioned above (PCL 17% by ES and PCL 15% by RJS), they had exhibited

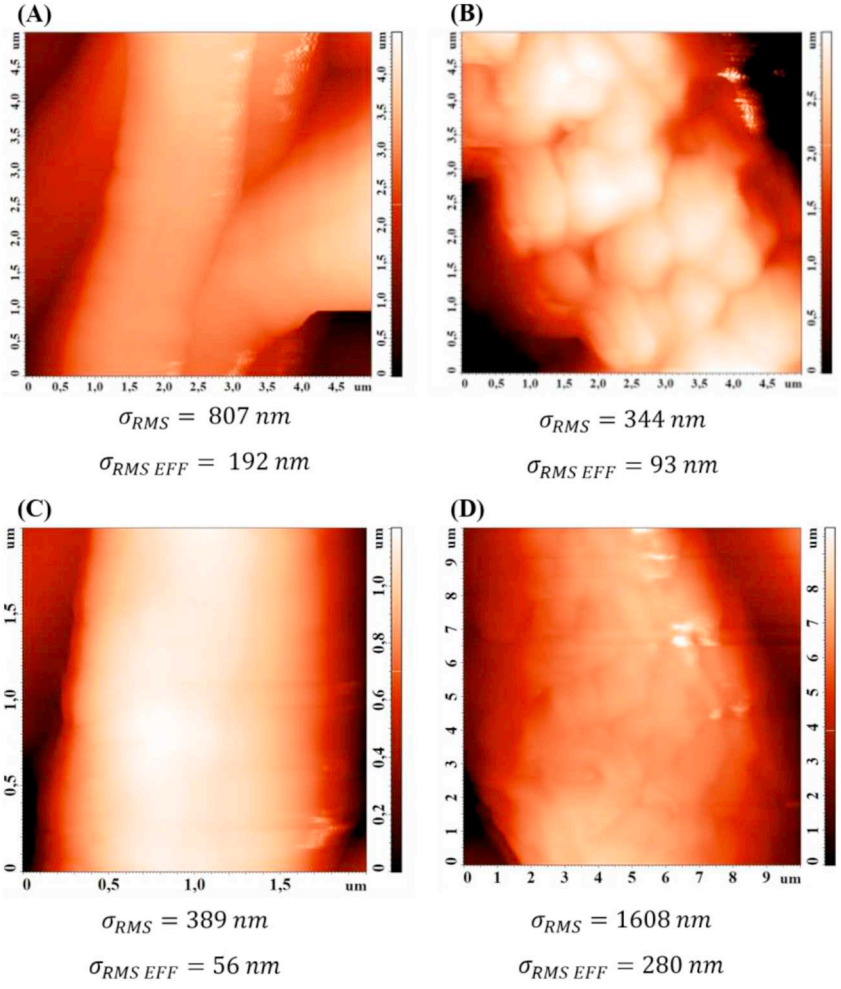

Fig. 2. AFM images of electrospun fibers corresponding to PCL at 15% (A) and rotary jet spun fibers at 15% (B). (C) is a detail of (A) and (D) is a detail of (C); an isolated single fiber is shown for (C) and (D). It is important to note that although (C) is a detail of (A) it continues to look like a smooth surface. This is not the case between (D) and (B), the acorns on (B) are transformed into a cracked surface. This situation is forced due to the different lengths of the fibers.

Table 1
Contact angle and surface energy components of PCL 17% by ES and PCL 15% by RJS. (n = 3).

Sample	Contact angle (°)		Surface free energy (mN/m)			$\frac{\gamma_p}{(\gamma_d+\gamma_p)}$
	Water	Diiodomethane	Dispersive (γ_d)	Polar (γ_p)	Total	
PCL 17% ES	150.5 ± 4.8	9.9 ± 0.0	52.2	19.9	72.1	0.28
PCL 15% RJS	148.7 ± 3.1	9.9 ± 0.0	52.2	19.9	72.1	0.28

Table 2
Thermal parameters obtained from the DSC thermograms of PCL fibers produced by ES and RJS.

wt (%)	T_m (°C)	ΔH_m (J g^{-1})	T_g (°C)	X_c (%)
ES				
12	61.39	72.29	−62.70	53.15
15	60.45	60.70	−58.92	44.63
17	60.49	59.73	−61.05	43.91
20	60.36	64.18	−59.99	47.19
RJS				
15	61.45	66	−56.93	48.52
20	61.47	64.72	−57.44	47.58

initially after an immediate drop of water, low wettability (CA > 150°) with a surface energy of 52 mN/m for both fibers (i.e., no significant difference was observed between them (Table 1)). We assumed that the chemical composition of the material was the same for both samples as they were made using the same material but with different topographies [42]. The average value of the work of adhesion (ΔF_{Adh} = +11.5 mJ/m^2) in both cases, indicated unfavorable conditions for bacteria colonization [43] (Table 2).

The surface free energy and adsorption depends linearly on Effective Root Mean Square Roughness [38,39]. As $\sigma_{RMS\ EFF}$ increases, the higher the adsorption, so RJS fibers had higher adsorption than ES fibers (Fig. 2C and D).

The thermogram analyses of the PCL fibers produced by ES and RJS showed a glass transition temperature (Tg) and a melting temperature (Tm), both close to 60 °C for all samples, irrespective of the processing method (Fig. 3 and Table 2). These results were similar to the data found in the literature, indicating that the method used did not interfere with the results. [15]

The degree of crystallinity of a material suggests the degradation of a material, as the higher the crystallinity, the stronger it will be. This is relevant for an implantable material and it may vary depending on the production process [44–46].

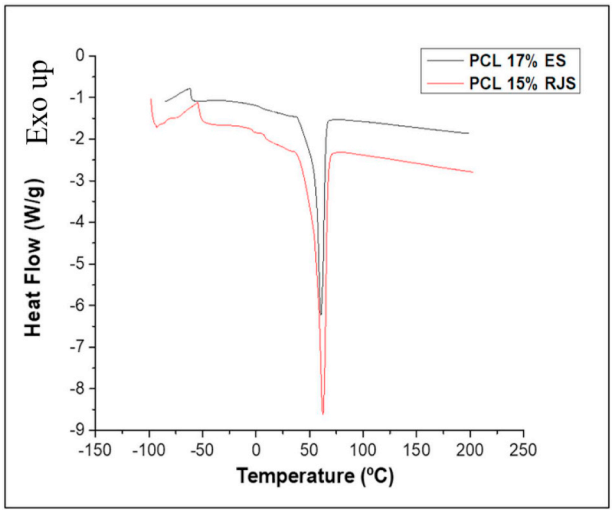

Fig. 3. DSC thermogram from −150 °C to 250 °C performed at a heating rate of 10 °C min^{-1} under a nitrogen atmosphere at a flow rate of 20 mL min^{-1}.

Results of this study showed that the processing technique had a minimal effect on the crystallinity of the fibers. The degree of crystallinity for the samples showed a decreasing trend with increasing PCL concentration for both techniques, as expected, since PCL crystallinity decreases with an increasing molecular weight. [46]

Early interactions between a material surface and biological fluids play a crucial role in determining cellular behavior (such as adhesion, differentiation and tissue formation). Therefore, the wettability of a material allows one to predict the hydrophilicity/hydrophobicity of the material surface and consequently cell susceptibility. [47,48]

The susceptibility of polymeric scaffolds to bacterial infection was determined here through colony forming unit assays (CFUs), and additionally we took SEM micrographs to visualize bacteria colonization on the polymeric scaffolds for both of the samples already mentioned. Fig. 4A shows the CFUs for *S. aureus* (gram positive) and Fig. 4B for *P. aeruginosa* (gram negative). Clearly, the fibers obtained by RJS reduced the colonization from both bacteria strains as compared to those obtained by ES. Fig. 4A1 and A2 shows numerous adherent bacteria covering the fibers produced by ES. In Fig. 4A2, the smooth fibers can be seen in detail. A similar result was observed when *P. aeruginosa* were cultivated on the fibers produced by ES (Fig. 4B1 and B2). Results suggested that the smooth PCL fiber surfaces were favorable to bacterial colonization.

On the other hand, when *S. aureus* were cultivated onto PCL fibers produced by RJS, we observed a decrease in bacteria colonization (Fig. 4A3), and that also was followed by *P. aeruginosa*. Although they presented some bacteria aggregates, the rough surface produced by RJS decreased bacteria colonization compared with ES PCL. Fig. 4A4 and B4 illustrates the rough fibers in detail. Clearly, the RJS fibers possessed a special topography compared to ES fibers to avoid bacteria colonization which requires further research. Besides, we decided to verify the cytotoxicity of our samples via interaction with fibroblasts compared to controls. Fig. 4C shows that no mammalian cytotoxicity was observed for all samples for the ES and RJS fibers. Herein, we propose that the morphology presented by rotary jet spun fibers can reduce bacteria colonization without the use of antibiotics. One of the challenges in tissue engineering is to produce a material with low or null susceptibility for bacteria colonization and at the same time allow or even promote mammalian cell interactions [49,50].

To prove this, the colonization of both gram-positive (+) and gram-negative (−) strains were evaluated. In addition, these bacteria were classified as the classic strains of: *Staphylococcus epidermidis* (+), *Pseudomonas aeruginosa* (−) and Brazilian clinical strains (multi-resistant bacteria): *Staphylococcus aureus* R1B1 (+), *Staphylococcus aureus* BEC9393 (Brazilian epidemic clone) (+), *Pseudomonas aeruginosa* 31NM (−) and *Klebsiella pneumoniae* KP230 (−).

Colony forming unit assays (Fig. 5) showed that the RJS fibers decreased bacteria colonization for both gram-positive and -negative bacteria (*S. epidermidis* and *S. aureus* RiB1) as compared to ES fibers. Unexpectedly, *S. aureus* BEC9393 showed inverse results since they contained the representative BEC strain, i.e. being more resistant than the other bacteria, this bacteria may have changes around the cell that make it oddly resistant and likely to adhere via different mechanisms. Interestingly, RJS fibers showed a significant difference in the reduction of bacterial colonization of a clinical strain of *P. aeruginosa* (31NM) and

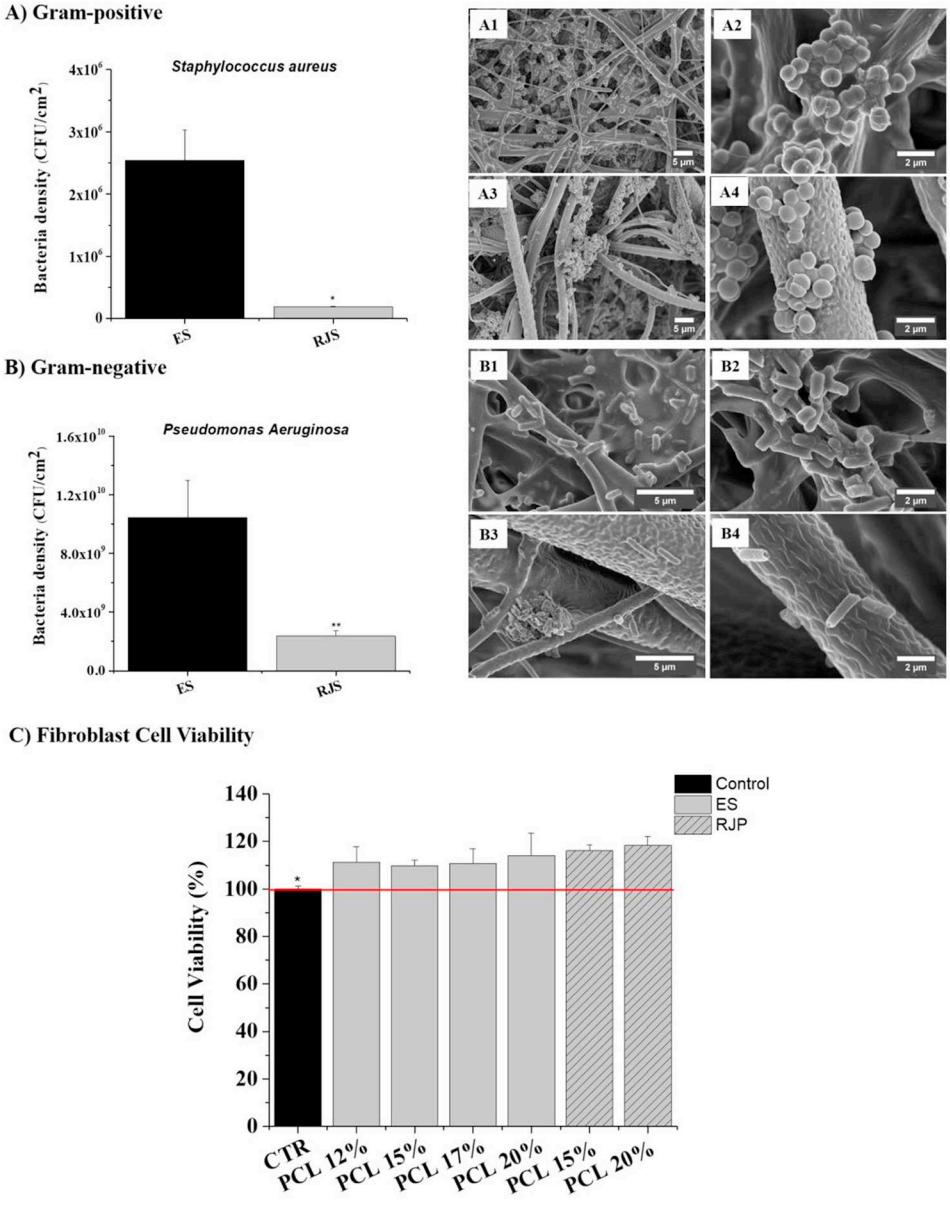

Fig. 4. Colony forming units (CFU) and SEM images of *Staphylococcus aureus* and *Pseudomonas aeruginosa* colonization of electrospun PCL 17% (*w/v*) and rotary jet spun PCL 15% (w/v) for 24 h. CFU of (A) *S. aureus* and (B) *P. aeruginosa*. A1 and A2 show micrographs collected from *S. aureus* cultivated on the electrospun fibers. A3 and A4 illustrate micrographs from *S. aureus* colonized onto the rotary jet spun fibers. B1 and B2 show micrographs collected from *P. aeruginosa* cultivated on electrospun fibers. B3 and B4 show micrographs collected from *P. aeruginosa* cultivated on rotary jet spun fibers. 10,000 cell/ml bacteria were seeded on both PCL fibers. Values represent the mean ± SD, $N = 3$. $^{*}p < 0.001$ compared to all others. (C) Viability of human dermal fibroblasts (HDF) on the different fibers made by electro and rotary jet spinning. Cells were seeded at 20,000 cells/cm^2 for 24 h. Values are mean ± SD, N = 3. $^{*}p < 0.001$ compared to all other fibers. The data are normalized using the cells only as a control.

no difference for classical strains (ATCC) while for *K. pneumoniae*, significant differences between samples were not observed.

RJS fibers are an alternative to ES to obtain ultrafine fibers with nanometer and submicron roughness and their special surface characteristics as an antifouling morphology. Further discussions about the difference in wettability and bacteria properties were considered here highlighting the importance of the physical surface presented on RJS PCL fibers. We propose two hypotheses for preferentially decreasing bacterial colonization on RJS PCL, not applying any antiseptic, one physical and the other biological; both must have concomitantly contributed to our results. In nature, there are several examples of antifouling surfaces such as the cicada wing, shark skin, lotus leaf and butterfly wings. Each one of them presents a superhydrophobic micro/nano hierarchical structure, in which these surfaces present unique topographical features, which contribute to the antifouling effect [33,41,51–53]. Nanopillar arrangements on cicada wings present bactericidal properties due to specific surface geometries, irrespective of surface chemistry. For the cicada wing, the bacteria cell membrane stretches in the regions suspended between nano pillars when the bacteria try to adhere, leading to non-uniform stretching due to the specific surface pattern which causes either no attachment or cell rupture. [54]

The shark skin presents anti-biofouling and self-cleaning properties which is attributed to micro-structured riblets that can vary by species and inhabited places. The material bioinspired by shark skin have been shown to be an effective tool to reduce bacterial binding. The mechanism is similar to that mentioned for circada wings above in which the lack of attachment of bacteria on the bioinspired surface happens due to the dimensions of the grooves between the riblets that are spaced (~2 µm) smaller than the size of bacteria (~1–3 µm), which prefers to settle in areas slightly larger than themselves. [35,55,56].

Impressively, our RJS fibers presented a similar geometry to these characteristics found in nature. Fig. 6 illustrates our polymeric fibers and the suggested mechanisms of bacteria adhesion on the RJS fibers and ES fibers. This figure provides a schematic fiber surface (from ES and RJS) and their likely interaction with a bacteria surface regarding both of these hypotheses.

It is known that bioinspired antifouling materials without any interference of nanoparticles or antibiotics, and only a physical interference, do not kill bacteria, but inhibit their colonization on the surface and may facilitate its disinfection [51–53].

Fig. 6A3 shows details of the space of roughness at 0.4–1.4 µm.

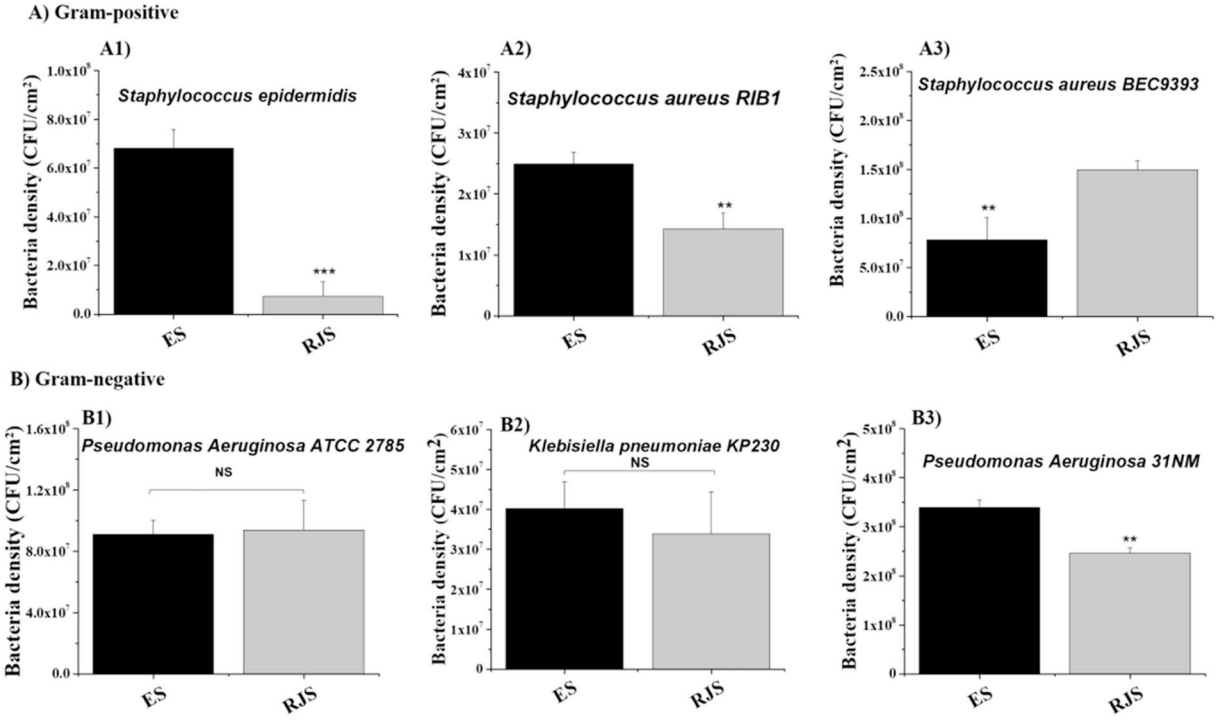

Fig. 5. Colony forming units (CFU) for gram-positive bacteria (A) and gram-negative bacteria (B). (A1) *Staphylococcus epidermidis,* (A2) *Staphylococcus aureus RiB1,* (A3) *Staphylococcus aureus BEC9393*. (B1) *Pseudomonas aeruginosa ATCC 2785,* (B2) *Pseudomonas aeruginosa 31NM* and (B3) *Klebsiella pneumoniae KP230*. Bacteria were seeded on the surface of electrospun (ES) and rotary jet spun (RJS) PCL scaffolds. Values represent the mean ± SD, $N = 3$. $^{**}p < 0.01$ $^{***}p < 0.001$.

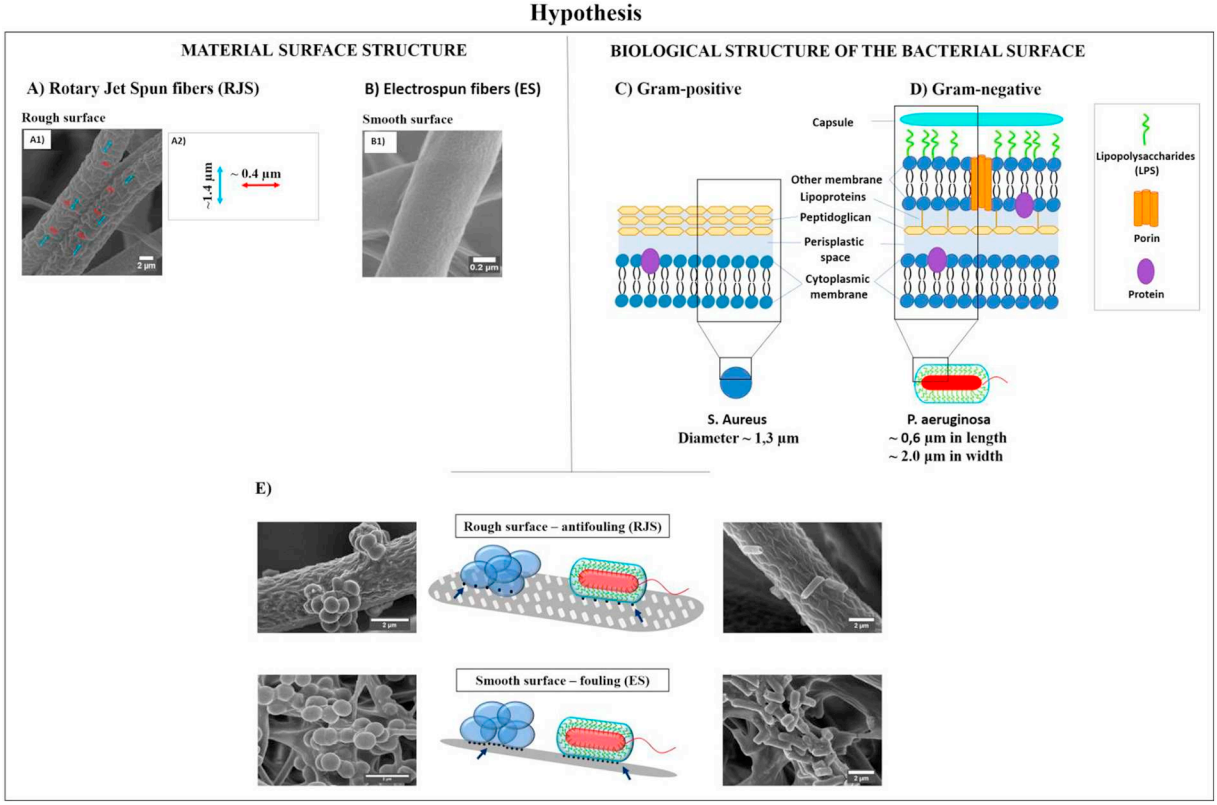

Fig. 6. Hypothesis. (A) Material surface structure. (A1) SEM images of a rotary jet spun fiber. A2 show the details of the rotary jet spun fiber rough structures, identifying spaces between 0.4–1.4 µm. B shows the micrograph from the collected electrospun PCL fibers and illustrates the details of a smooth surface. (C and D) Biological structure of the bacteria surface. (C) Gram-positive bacteria surface and their respective bacteria size. (D) Gram-negative bacteria surface and their respective bacteria size. E illustrates a schematic of bacteria adhesion over the scaffold surface and the arrows indicate the contact points of bacteria adhesion on the material surface.

These spaces were smaller than the size of bacteria, becoming harder for bacteria to settle, and strengthening an antifouling physical mechanism. Contrarily, ES fibers showed a smooth topographical surface allowing for better bacteria wall contact (Fig. 6B1 and B2).

Some research suggests that the type and size of topographies can prevent colonization by micro-organisms, changing cellular morphology, causing phenotypic changes and finally decreasing viability [33,51,57]. It is easier for micro-organisms to attach to areas slightly larger than themselves, due to surface area contact with the substrate. The reduction of contact points between a substrate and microorganism lead to a lower strength, and bacteria in a harmless state [57,58]. Despite the morphology presented by RJS fibers reducing bacteria colonization, they did not seem to inhibit the proliferation of mammalian cells. Likely, the dimensions of mammalian cells would permit several focal adhesion points on fibers through filopodia and lamellipodia formation, allowing for mammalian cell attachment [59,60].

Besides the physical interaction hypothesis, we proposed a biological hypothesis suggesting that the bacterial wall structure inters with adhesion to the fibers, explaining the difference found between gram-positive and –negative cells (Fig. 6C–F). The gram-positive bacteria have a simple surface with a membrane and several layers of peptidoglycan (Fig. 6C) [61,62]. However, the gram-negative bacteria presents a complex surface with a membrane, some layers of peptidoglycans, an outer membrane containing lipopolysaccharides (LPS) and a capsule of polysaccharides (Fig. 6D) [61,62]. This type of bacteria is more resistant to surface geometries since they have a complex surface. Therefore, some antibiotics are less active in gram negative than in gram positive bacteria. In addition, the evidence suggests that the presence of LPS in the membrane of gram-negative bacteria plays an important role in the initial adhesion of bacteria to surfaces. It has been reported that changes in the environment induce modification of the cell surface of some bacteria, indicating that the bacterium is able to alter its cell surface according to the environment, such as hydrophobicity [63–66]. In addition, the capsule is an external barrier that protects the bacteria which provides increased resistance, and it is composed of primarily long chain polysaccharides [67].

The less efficient results of inhibiting bacteria on ES compared to RJS fibers with gram-negative bacteria came comparatively close to characteristics of the bacterial surface, where the gram-negative cells showed better bacterial colonization, suggesting the wall structure of the bacterial could overcome surface ES morphologies yet the RJS fibers presented an anti-fouling surface.

3. Conclusions

Herein, for the first time, we extruded raw PCL structures, and made comparisons between the techniques of electrospinning (ES) and rotary jet spinning (RJS). According to results, we had two different PCL scaffold morphologies: smooth fibers by ES and rough fibers by RJS. The RJS PCL scaffolds showed an interesting way to obtain ultrafine fibers with nanometer and submicron rough fibers with special surface characteristics disturbing bacteria colonization. Although the fibers manufactured in this study were not modified in any way, one may provide an antiseptic property by mixing them with chemicals with anti-bacterial responses widening their biological applications. In the future analyses of these PCL scaffolds with the addition of some nanocomposites or pharmacological components, further impairment of bacterial adhesion and increased biological properties may result. In summary, the RJS showed a promising biomaterial for scaffolds manufacturing, with special topography, susceptible to mammalian cell interactions and tissue growth, and with low bacterial colonization (without resorting to antibiotic use). Features widely chased by the bioengineering field.

4. Experimental section

4.1. Materials

Poly (ε-caprolactone) (PCL – M_w 80,000) was purchased from Sigma- Aldrich®. Chloroform (99%, Sigma- Aldrich®) and acetic acid (CH_3COOH, glacial – Synth) were used as solvents.

4.2. Cellular assays

Human dermal fibroblasts (HDF, CC-2509) were purchase from Lonza, Basel, Switzerland. Dulbecco's Modified Eagle Medium (DMEM, Sigma Aldrich), Fetal bovine serum (Hyclone, Logan, UT), Penicillin/streptomycin (P/S, Sigma Aldrich), 0.25% trypsin-EDTA (Sigmka-Aldrich), 3-(4,5-dimethylthiazol-2-yl)-2,5-diphenyltetrazolium bromide (MTT, Promega, Fitchburg,WI), and Dulbecco's phosphate-buffered saline without calcium chloride and magnesium chloride (dPBS, Sigma Aldrich) were obtained as described.

4.3. Bacteria assays

Staphylococcus aureus (ATCC-12600) [American Type Culture Collection, Manassas, VA, USA], *Staphylococcus aureus* RiB1, *Staphylococcus aureus* (BEC9393), *Staphylococcus epidermidis, Pseudomonas aeruginosa* (ATCC 35984), *Pseudomonas aeruginosa* (ATCC 2785), *Pseudomonas aeruginosa 31NM*, and *Klebsiella pneumoniae KP230* were used in this study. Tryptic soy broth (TSB, 30 g L^{-1}, Sigma-Aldrich) and Agar (15 g L^{-1}, Sigma-Aldrich) were purchased as described.

4.4. Electrospinning and rotary jet spinning of PCL fibers

ES was performed using different concentrations of PCL (12%(w/t), 15%(w/t), 17%(w/t) and 20%(w/t)). The polymer solutions were dissolved in acetic acid. The solutions were magnetically stirred at room temperature. The solution was placed in a 5 mL plastic syringe with a metal needle tip and it was coupled to an infusion pump to control feed rates of the solution. A voltage was applied between the needle tip and the ground collector (Fig. 7A). ES conditions were established as follows: 16 kV, needle tip (gauge 23), 15 cm as needle-collector distance, 0.8 mL h^{-1}, controlled temperature (23 °C) and humidity (~30%). The fibers were randomly oriented and collected on an aluminum foil.

The system used for obtaining polymer fibers by rotary jet spinning in our laboratory is schematically shown in Fig. 7B. The system consisted of: (1) a perforated reservoir with an inner volume of 6 mL with two end holes 0.3 mm in diameter rotating on its vertical axis in the center of a disc with static collectors with two opposing holes in its walls coupled to a motor, (2) a motor (3000 to 30,000 rpm), (3) a collecting system, (4) a reservoir with a syringe and needle, and (5) a constant feed system of the polymer solution injected with a peristaltic pump system installed (controlled by potentiometer).

Different concentrations of PCL were used (15% and 20% wt) using chloroform as the solvent. The solutions were magnetically stirred at room temperature.

4.5. Characterization

Field Emission Electronic Microscopy (FE-SEM, ZEISS EVO-MA 10) was used to characterize the surface of the samples. To analyze, the samples were first coated with a thin layer of gold using a sputter-coat system. The voltage was 3.0 kV at a magnification of 5 K for all fibers. Differential scanning calorimetry (DSC, Q10, TA instruments) was used to evaluate the thermal parameters from the produced fibers. For that, the following parameters were used: a heating rate of 10 °C min^{-1}, temperature ranged from −150 to 250 °C, and an atmosphere of N_2 (at a flow rate of 50 mL min^{-1}). Sample weight ranged from 8 to 10 mg. In

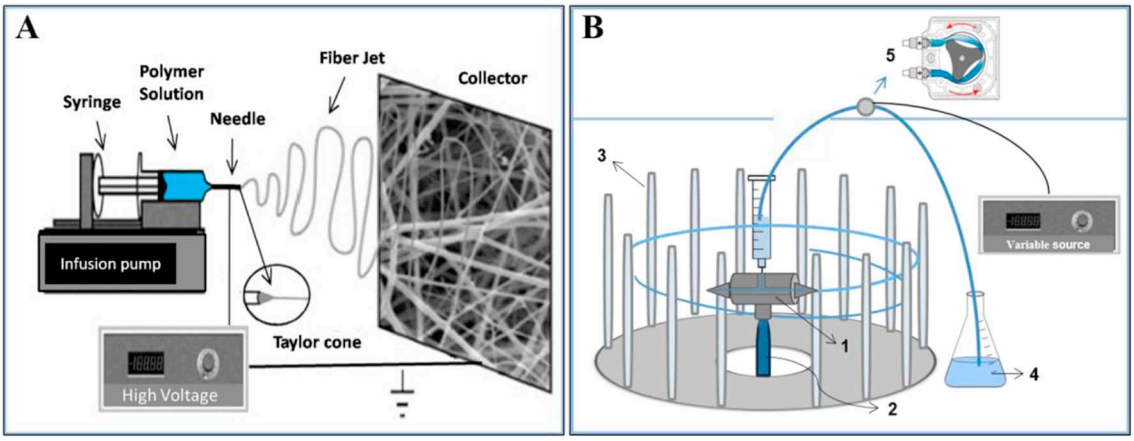

Fig. 7. The (A) electrospinning (ES) and (B) rotary jet spinning (RJS) process. Details of the parts used to set up the ES process are described in A. The numbers described at B correspond to the RJS apparatus: (1) reservoir, (2) motor, (3) collector, (4) system to deliver the solution and (5) details of the peristaltic pump.

order to determine the degree of crystallinity (Xc) of the samples, the following equation was used:

$$X_c = (\Delta H_m / \Delta H^\circ_m) \times 100\% \quad (1)$$

where ΔH_m corresponded to the heat of fusion of the endothermic peak of fusion and ΔH°_m was the heat of fusion for the 100% crystalline raw PCL.

The wettability of the samples was determined using a goniometer (DSA100, Krüss) and for measuring contact angles, single drops of deionized water and diiodomethane were dropped on the surface of the samples ($n = 3$) and advanced measurements (5 min) of the angle were taken from 5 to 3000 s at room temperature. The surface energy was calculated, and work of bacteria adhesion was also inserted (Supplementary data 1).

4.6. AFM analysis

An Atomic Force Microscope, NTEGRA *Spectra*, was used to obtain AFM images. The different areas were scanned using 0.3 Hz in non-contact mode. In all cases the image was composed with 512 × 512 pixels.

The NTMDT *Nova* program was used to perform the analysis. At the first stage, in the original image, a filter was applied to flatten the image. This first correction was necessary due to the piezoelectricity that controlled the scanner. The Root Mean Square (σ_{RMS}) Roughness was calculated through the following equation applied throughout the image:

$$\sigma_{RMS} = \sqrt{\frac{1}{N_y N_x}\left(\sum_{j=1}^{N_y}\sum_{i=1}^{N_x}(Z_{ij} - \overline{Z})^2\right)} \quad (2)$$

N_x is the number of pixels in the x direction and N_y in the y direction; $\overline{Z}$ is the mean height and Z_{ij} is the height at the ij pixel. In a second step, a High-Pass 3 × 3 filter was applied, allowing one to isolate the fibers from the rest of the image. From this processed image we obtain the Filtered Root Mean Square ($\sigma_{RMS\ FIL}$) Roughness, and finally, using the Dangwoo et al. expression [38], we obtained the Effective Root Mean Square $\sigma_{RMS\ EFF}$ Roughness.

4.7. Cellular assays

Human dermal fibroblasts were cultured in DMEM supplemented with 10% FBS and 1% antibiotics in an incubator at 37 °C in the presence of 5% CO_2. An MTS assay was used to determine the metabolic cell activity of the HDFs for all of the PCL fibers produced. The samples were cut into pieces (1 × 1 cm^2) and sterilized under ultraviolet light for 30 min on each side. HDFs were cultured to 90% confluence, rinsed with dPBS, and detached from the tissue culture plate by using 0.25% trypsin-EDTA. Cells were seeded at 20,000 cells/cm^2 and incubated for 24 h. Afterwards, the medium was removed from the sample and 1 ml of the 1:5 MTS dye with DMEM medium (*v*/v) was added to each well. Samples were placed back into the incubator for 4 h. After incubation, 100 μL of the 1 mL solution was transferred to a 96 well plate and read in a SpectraMaxM3 microplate reader (Molecular Devices, Sunnyvale, CA) at an absorbance wavelength of 490 nm. The absorbance values of the wells containing only DMEM medium without cells were subtracted from the absorbance values of the wells containing cells. Each data point is represented from three independent experiments ($N = 3$).

4.8. Bacterial cell activity and SEM

Bacterial strains described above were inoculated in 3% Tryptic soy broth (TSB) for 14 h. This bacteria solution was diluted in order to produce a working solution at concentrations of 10^4 cells/mL. Afterwards, the sterilized samples (1 × 1 cm^2) in triplicate were set into 24-well tissue culture plates and individually inoculated with 1000 μL of a bacteria working solution, and incubated for 24 h. Afterwards, the samples were lightly rinsed with PBS (x2) to remove any non-adherent bacteria, next the scaffolds were set into individual vials with PBS (1000 μL) then vortexed over 15 min to remove the strongly adherent bacteria. This bacterial solution suspension was diluted serially (10×; 100×; 1000×) and plated on tryptic soy agar plates as 10 μL aliquots, in triplicate, and incubated for 14 h at 37 °C. Afterwards, the colonies were counted to calculate the colony-forming units (CFUs).

For SEM analysis, the bacteria were fixed using 2.5% glutaraldehyde and 4% paraformaldehyde in PBS for 1 h. After, they were dehydrated in a series of acetone solutions until reaching 100%, followed by rinsing with acetone plus HMDS (1:1) and pure HMDS for 10 min each. The specimens were dried, platinum coated, and analyzed by SEM to observe bacterial morphology.

4.9. Statistical analysis

All experiments were conducted in triplicate and were repeated at least three different times with analysis of variance (ANOVA) followed by Student's *t*-tests to determine statistical differences between the mean values.

Declaration of competing interest

The authors declare that the research was conducted in the absence

of any commercial or financial relationships that could be construed as a potential conflict of interest.

Acknowledgements

The authors would like to thank the São Paulo Research Foundation (FAPESP: 2014/16295-2, 2011/17877-7, 2011/20345-7, 2015/08523-8, 2015/09697-0 and 2016/00576-1), the Coordination for the Improvement of Higher Education Personnel (CAPES, grant 88881.068048/2014-01), a scholarship from CAPES (88887.116351/2016-00), and Northeastern University for funding. This study was partially supported by the Brazilian National Council for Scientific and Technological Development (CNPq) (process number: 465572/2014-6), the São Paulo Research Foundation (FAPESP) (2014/50869-6), and CAPES (Education Ministry) (23038.000776/201754) via the projects of the National Institute for Science and Technology on Organic Electronics (INEO).

Appendix A. Supplementary data

Supplementary data to this article can be found online at https://doi.org/10.1016/j.msec.2020.110706.

References

[1] K.L. Christman, Science 363 (2019) 340–341.
[2] N.D. Evans, E. Gentleman, J.M. Polak, Mater. Today 9 (2006) 26–33.
[3] B. Seal, T. Otero, A. Panitch, Materials Science and Engineering: R: Reports 34 (2001) 147–230.
[4] G. Chan, D.J. Mooney, Trends Biotechnol. 26 (2008) 382–392.
[5] G. Vunjak-Novakovic, D.L. Kaplan, Tissue Eng. 12 (2006) 3261–3263.
[6] K. Rezwan, Q. Chen, J. Blaker, A.R. Boccaccini, Biomaterials 27 (2006) 3413–3431.
[7] E. Sachlos, J. Czernuszka, Eur Cell Mater 5 (2003) 39–40.
[8] C.P. Barnes, S.A. Sell, E.D. Boland, D.G. Simpson, G.L. Bowlin, Adv. Drug Deliv. Rev. 59 (2007) 1413–1433.
[9] T. Desai, Med. Eng. Phys. 22 (2000) 595–606.
[10] F. Asghari, M. Samiei, K. Adibkia, A. Akbarzadeh, S. Davaran, Artificial cells, nanomedicine, and biotechnology, 45 (2017) 185–192.
[11] E. Malikmammadov, T.E. Tanir, A. Kiziltay, V. Hasirci, N. Hasirci, Journal of Biomaterials Science, Polymer Edition 29 (2018) 863–893.
[12] Z.-M. Huang, Y.-Z. Zhang, M. Kotaki, S. Ramakrishna, Compos. Sci. Technol. 63 (2003) 2223–2253.
[13] S. Khorshidi, A. Solouk, H. Mirzadeh, S. Mazinani, J.M. Lagaron, S. Sharifi, S. Ramakrishna, J. Tissue Eng. Regen. Med. 10 (2016) 715–738.
[14] H. Hosseinkhani, P.-D. Hong, D.-S. Yu, Y.-R. Chen, D. Ickowicz, I.-Y. Farber, A.J. Domb, Int. J. Nanomedicine 7 (2012) 3035.
[15] A. Valizadeh, M. Bakhtiary, A. Akbarzadeh, R. Salehi, S.M. Frakhani, O. Ebrahimi, M. Rahmati-yamchi, S. Davaran, Artif Cells Nanomed Biotechnol 44 (2016) 504–509.
[16] S.S. Ray, S.-S. Chen, C.-W. Li, N.C. Nguyen, H.T. Nguyen, RSC Adv. 6 (2016) 85495–85514.
[17] M.R. Badrossamay, H.A. McIlwee, J.A. Goss, K.K. Parker, Nano Lett. 10 (2010) 2257–2261.
[18] E. Stojanovska, E. Canbay, E.S. Pampal, M.D. Calisir, O. Agma, Y. Polat, R. Simsek, N.A.S. Gundogdu, Y. Akgul, A. Kilic, RSC Adv. 6 (2016) 83783–83801.
[19] G.M. Gonzalez, L.A. MacQueen, J.U. Lind, S.A. Fitzgibbons, C.O. Chantre, I. Huggler, H.M. Golecki, J.A. Goss, K.K. Parker, Macromolecular Materials and Engineering 302 (2017) 1600365(-n/a).
[20] M.R. Badrossamay, K. Balachandran, A.K. Capulli, H.M. Golecki, A. Agarwal, J.A. Goss, H. Kim, K. Shin, K.K. Parker, Biomaterials 35 (2014) 3188–3197.
[21] P. Mellado, H.A. McIlwee, M.R. Badrossamay, J.A. Goss, L. Mahadevan, K. Kit Parker, Appl. Phys. Lett. 99 (2011) 203107.
[22] D. Teterycz, T. Ferry, D. Lew, R. Stern, M. Assal, P. Hoffmeyer, L. Bernard, I. Uçkay, Int. J. Infect. Dis. 14 (2010) e913–e918.
[23] J. Rodríguez-Hernández, Bacterial Infections: Few Concepts, Polymers Against Microorganisms, Springer, 2017, pp. 13–37.
[24] S.L. Percival, L. Suleman, C. Vuotto, G. Donelli, J. Med. Microbiol. 64 (2015) 323–334.
[25] B. Li, T.J. Webster, Journal of Orthopaedic Research® 36 (2018) 22–32.
[26] C.R. Arciola, D. Campoccia, G.D. Ehrlich, L. Montanaro, Biofilm-based Implant Infections in Orthopaedics, Biofilm-based Healthcare-associated Infections, Springer, 2015, pp. 29–46.
[27] M. Shakibaie, H. Forootanfar, Y. Golkari, T. Mohammadi-Khorsand, M.R. Shakibaie, J. Trace Elem. Med. Biol. 29 (2015) 235–241.
[28] E. Piacenza, A. Presentato, E. Zonaro, J.A. Lemire, M. Demeter, G. Vallini, R.J. Turner, S. Lampis, Microbial Biotechnology (2017) (n/a-n/a).
[29] N. Kaur, R. Prasad, A. Varma, Int. J. Pharm. Bio Sci. 4 (2013) 957–964.
[30] https://www.cdc.gov/.
[31] S. Singh, S.K. Singh, I. Chowdhury, R. Singh, The open microbiology journal 11 (2017) 53.
[32] C.W. Hall, T.-F. Mah, FEMS Microbiol. Rev. 41 (2017) 276–301.
[33] G.D. Bixler, B. Bhushan, Phil. Trans. R. Soc. A 370 (2012) 2381–2417.
[34] S. Nir, M. Reches, Curr. Opin. Biotechnol. 39 (2016) 48–55.
[35] Q. Xu, W. Zhang, C. Dong, T.S. Sreeprasad, Z. Xia, J. R. Soc. Interface 13 (2016) 20160300.
[36] I. Armentano, C.R. Arciola, E. Fortunati, D. Ferrari, S. Mattioli, C.F. Amoroso, J. Rizzo, J.M. Kenny, M. Imbriani, L. Visai, The Scientific World Journal 2014, (2014).
[37] F. Bobbert, A. Zadpoor, J. Mater. Chem. B (2017).
[38] D. Khang, S.Y. Kim, P. Liu-Snyder, G.T. Palmore, S.M. Durbin, T.J. Webster, Biomaterials 28 (2007) 4756–4768.
[39] B. Ercan, D. Khang, J. Carpenter, T.J. Webster, Int. J. Nanomedicine 8 (Suppl. 1) (2013) 75–81.
[40] X. Zhang, L. Wang, E. Levänen, RSC Adv. 3 (2013) 12003–12020.
[41] S. Nishimoto, B. Bhushan, RSC Adv. 3 (2013) 671–690.
[42] N.S. Kasalkova, P. Slepicka, Z. Kolska, V. Svorcik, Wettability and other surface properties of modified polymers, Wetting and Wettability, 2015.
[43] R.P. Schneider, J. Colloid Interface Sci. 182 (1996) 204–213.
[44] E. Kuzelova Kostakova, L. Meszaros, G. Maskova, L. Blazkova, T. Turcsan, D. Lukas, Journal of Nanomaterials 2017, (2017).
[45] K.K. Kar, J.K. Pandey, S. Rana, Handbook of Polymer Nanocomposites. Processing, Performance and Application: Volume B: Carbon Nanotube Based Polymer Composites, Springer Berlin Heidelberg, 2014.
[46] M.A. Woodruff, D.W. Hutmacher, Prog. Polym. Sci. 35 (2010) 1217–1256.
[47] M.M. Gentleman, E. Gentleman, Int. Mater. Rev. 59 (2014) 417–429.
[48] J. Wei, T. Igarashi, N. Okumori, T. Igarashi, T. Maetani, B. Liu, M. Yoshinari, Biomed. Mater. 4 (2009) 045002.
[49] S. Guo, X. Zhu, X.J. Loh, Mater. Sci. Eng. C 70 (2017) 1163–1175.
[50] N. Beyth, Y. Houri-Haddad, A. Domb, W. Khan, R. Hazan, Evidence-based Complementary and Alternative Medicine 2015, (2015).
[51] M.L. Carman, T.G. Estes, A.W. Feinberg, J.F. Schumacher, W. Wilkerson, L.H. Wilson, M.E. Callow, J.A. Callow, A.B. Brennan, Biofouling 22 (2006) 11–21.
[52] H. Gu, D. Ren, Front. Chem. Sci. Eng. 8 (2014) 20–33.
[53] V.B. Damodaran, N.S. Murthy, Biomaterials Research 20 (2016) 18.
[54] S. Pogodin, J. Hasan, V.A. Baulin, H.K. Webb, V.K. Truong, T.H.P. Nguyen, V. Boshkovikj, C.J. Fluke, G.S. Watson, J.A. Watson, Biophys. J. 104 (2013) 835–840.
[55] X. Pu, G. Li, H. Huang, Biology open 5 (2016) 389–396.
[56] E.E. Mann, D. Manna, M.R. Mettetal, R.M. May, E.M. Dannemiller, K.K. Chung, A.B. Brennan, S.T. Reddy, Antimicrob. Resist. Infect. Control 3 (2014) 28.
[57] M. Abrigo, P. Kingshott, S.L. McArthur, ACS Appl. Mater. Interfaces 7 (2015) 7644–7652.
[58] A. Scardino, J. Guenther, R. De Nys, Biofouling 24 (2008) 45–53.
[59] D.-H. Kim, P.P. Provenzano, C.L. Smith, A. Levchenko, J. Cell Biol. 197 (2012) 351–360.
[60] K. Anselme, A. Ponche, M. Bigerelle, Proc Inst Mech Eng H 224 (2010) 1487–1507.
[61] G. Seltmann, O. Holst, The Bacterial Cell Wall, Springer Science & Business Media, 2013.
[62] K. Hori, S. Matsumoto, Biochem. Eng. J. 48 (2010) 424–434.
[63] M. van de Lagemaat, A. Grotenhuis, B. van de Belt-Gritter, S. Roest, T.J. Loontjens, H.J. Busscher, H.C. van der Mei, Y. Ren, Acta Biomater. 59 (2017) 139–147.
[64] B. Li, B.E. Logan, Colloids Surf. B: Biointerfaces 36 (2004) 81–90.
[65] Y. Yuan, M.P. Hays, P.R. Hardwidge, J. Kim, RSC Adv. 7 (2017) 14254–14261.
[66] M. Van Loosdrecht, J. Lyklema, W. Norde, G. Schraa, A. Zehnder, Appl. Environ. Microbiol. 53 (1987) 1893–1897.
[67] V. Band, D. Weiss, Antibiotics 4 (2015) 18–41.

A comparison between electrospinning and rotary-jet spinning to produce PCL fibers with low bacteria colonization

M.M. Machado-Paula[1,2], M.A.F. Corat[3], M. Lancellotti[4], G. Mi[2], F.R. Marciano[2,5], M. L. Vega[6], A. A. Hidalgo[6], T.J. Webster[2*], and A.O. Lobo[2,7*]

Supplementary file 1

Fig. 1 show the drops of electrospun and rotary-jet spun fibers. **Fig 1a** and **1c** referred to drops collected from electrospun fibers using water and diiodomethane, respectively. **Fig. 1b** and **1d** referred to drops collected from rotary-jet spun fibers using water and diiodomethane, respectively. Independently of fibers, we produced superhydrophobic structures.

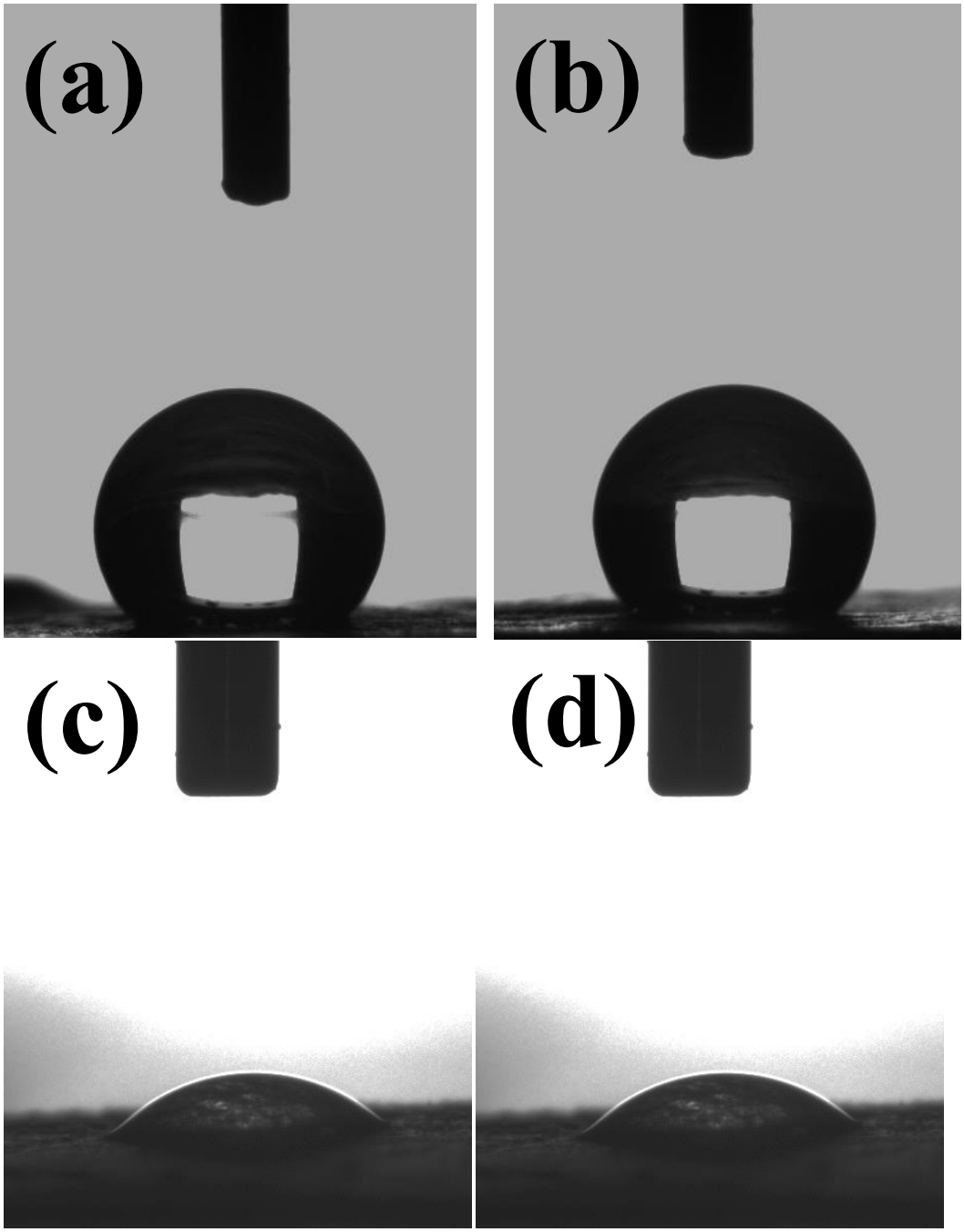

Figure SS1. Pictures taken from electrospun (a and c) and rotary-jet (b and d) spun fibers surfaces after drop water and diiodomethane, respectively.

Supplementary file 2

The surface energy composed of polar and dispersive components of the samples was evaluated by measuring contact angle. The interfacial tension between two condensed phases can be determined by Young' equation [1], according to which

$$cos\theta\gamma_{LV} = \gamma_{SV} - \gamma_{SL}, \quad (1)$$

where θ is the measured contact angle between liquid and solid, and γ_{LV}, γ_{SV}, and γ_{SL} are the interfacial energies of the liquid/vapor, solid/vapor, and solid/liquid interfaces, respectively. This equation can be rewritten as the Young-Duprè equation:

$$W_a = \gamma_{LV}(1 + cos\theta) = \gamma_{SV} - \gamma_{SL}, \quad (2)$$

where W_a is the adhesion energy per unit area of the solid and liquid surfaces. In the general form of equation (1), (2) then can be written:

$$\gamma_{LV}(1 + cos\theta) = 2\sqrt{\gamma_L^p \gamma_S^p} + 2\sqrt{\gamma_L^D \gamma_S^D}, \quad (3)$$

where γ^p_L and γ^p_S are the polar components of the surface energy of liquid and solid phases, respectively, and γ^D_L and γ^D_S are the dispersive component of the surface energy of the liquid and solid phases, respectively. Because γ^D_L and γ^p_L have been published for many liquids, it is possible to approximate γ^D_S and γ^p_S from a single measurement of θ by with equation (3). Therefore, by measuring the contact angles of two different liquids (distilled water and diiodomethane) with well-known polar and dispersive components of surface energy (Table 1), Eq. (3) can be solved to determine the polar and dispersive components of the surface energy of the materials [2-3]. The liquid was dropped automatically by a computer-controlled system. All measurements were carried out at room temperature.

Table 1. Test liquids and their surface tension components [2].

Surface tension data (mN/m)	γ^{D}_{L}	γ^{p}_{L}	γ_{LV}
Water	21.8	51.0	72.8
Diiodomethane	50.8	0.0	50.8

Thermodynamically, the process of adhesion and spreading of cells and bacteria from a liquid suspension onto solid substrata can be described by the following equation [4]:

$$\Delta F_{Adh} = \gamma_{BS} - \gamma_{BL} - \gamma_{SL}, \tag{4}$$

where ΔF_{Adh} is the interfacial free energy of adhesion, γ_{BS} is the bacteria-solid substratum interfacial free energy, γ_{BL} the bacteria-liquid interfacial free energy, and γ_{SL} is the solid-liquid interfacial free energy, respectively. They can be calculated by using contact angle data and the van Oss acid-base approach [5-7].

The following equation was used to determine the interfacial energy of cell adhesion to a solid surface [5-7]:

$$\Delta F_{Adh} = 2\begin{pmatrix} \sqrt{\gamma_S^{LW}\gamma_L^{LW}} + \sqrt{\gamma_S^{p}\gamma_L^{D}} + \sqrt{\gamma_S^{D}\gamma_L^{p}} \\ + \sqrt{\gamma_B^{LW}\gamma_L^{LW}} + \sqrt{\gamma_B^{p}\gamma_L^{D}} + \sqrt{\gamma_B^{D}\gamma_L^{p}} \\ - \sqrt{\gamma_S^{LW}\gamma_B^{LW}} - \sqrt{\gamma_S^{p}\gamma_B^{D}} - \sqrt{\gamma_S^{D}\gamma_B^{p}} - \gamma_L \end{pmatrix}. \tag{5}$$

According to thermodynamic theory, if ΔF_{Adh} is negative, bacteria spreading is energetically favorable; while if ΔF_{Adh} is positive, bacteria spreading is thermodynamically unfavorable.

References

1. Young, T., III. An essay on the cohesion of fluids. *Philosophical Transactions of the Royal Society of London* **1805,** *95*, 65-87.
2. Van Oss, C. J.; Good, R. J.; Chaudhury, M. K., The role of van der Waals forces and hydrogen bonds in "hydrophobic interactions" between biopolymers and low energy surfaces. *Journal of Colloid and Interface Science* **1986,** *111* (2), 378-390.
3. Flahaut, E.; Durrieu, M. C.; Remy-Zolghadri, M.; Bareille, R.; Baquey, C., Investigation of the cytotoxicity of CCVD carbon nanotubes towards human umbilical vein endothelial cells. *Carbon* **2006,** *44* (6), 1093-1099.
4. Schakenraad, J. M.; Busscher, H. J.; Wildevuur, C. R.; Arends, J., Thermodynamic aspects of cell spreading on solid substrata. *Cell biophysics* **1988,** *13* (1), 75-91.
5. Liu, C.; Zhao, Q.; Liu, Y.; Wang, S.; Abel, E. W., Reduction of bacterial adhesion on modified DLC coatings. *Colloids and Surfaces B: Biointerfaces* **2008,** *61* (2), 182-187.
6. Schneider, R. P., Conditioning Film-Induced Modification of Substratum Physicochemistry—Analysis by Contact Angles. *Journal of Colloid and Interface Science* **1996,** *182* (1), 204-213.
7. Wang, J.; Huang, N.; Pan, C. J.; Kwok, S. C. H.; Yang, P.; Leng, Y. X.; Chen, J. Y.; Sun, H.; Wan, G. J.; Liu, Z. Y.; Chu, P. K., Bacterial repellence from polyethylene terephthalate surface modified by acetylene plasma immersion ion implantation–deposition. *Surface and Coatings Technology* **2004,** *186* (1), 299-304.

ANNEX B – PAPER 2

Rotary jet spun polycaprolactone/hydroxyapatite and carbon nanotubes scaffolds seeded with bone marrow mesenchymal stem cells increased bone neoformation

Mirian M. Machado-Paula[1,2], Marcus A.F. Corat[3], Luana M.R. Vasconcellos[4], Juliani C.R. Araújo[4], Gujie Mi[2], Paria Ghannadian[2], Tatiane V. Toniato[1], Fernanda R. Marciano[5], Thomas J. Webster[2]* and Anderson O. Lobo[2,6]*

[1]Institute of Research and Development, University of Vale do Paraíba, São Jose dos Campos, SP, 12244 – 000, Brazil

[2]Nanomedicine Laboratory, Department of Chemical Engineering, Northeastern University, Boston, MA 02115, USA.

[3]Multidisciplinary Center for Biological Research, State University of Campinas, Campinas, SP, 13083-877, Brazil.

[4]Department of Bioscience and Oral Diagnosis, Institute of Science and Technology, Sao Paulo State University, Sao Jose dos Campos, Sao Paulo, Brazil.

[5]Department of Physics, UFPI - Federal University of Piaui, 64049-550 Teresina, PI, Brazil.

[6]LIMAV-Interdisciplinary Laboratory for Advanced Materials, BioMatLab, Department of Materials Engineering, UFPI - Federal University of Piaui, 64049-550 Teresina, PI, Brazil.

*Corresponding authors: Prof. Thomas Jay Webster. Email: th.webster@northeastern.edu and Prof. Dr. Anderson Oliveira Lobo. Email: lobo@ufpi.edu.br.

Abstract

Synthetic biomaterials are being explored as a promising alternative to address the limitations found in current treatments for the replacement or repair of bone tissue. Technologies based on well-defined combinations of osteoconductive nanomaterials, suitable scaffolds, and osteogenic cell populations, are desirable for bone reconstructive surgery. Herein, the efficacy of polycaprolactone (PCL) fibers with incorporated carbon nanotubes (CNT) and hydroxyapatite (nHap) nanoparticles, using two different methods for fabrication: Electrospinning (ES) and Rotary Jet spinning (RJS), were investigated. The morphology, thermal and mechanical features were characterized. PCL scaffold morphologies were dependent on the fabrication method used. RJS showed ultrathin fibers thickener and more porous than those that by produced by ES, and a slight difference in fibers diameters and morphology were observed after nanoparticles incorporated (ranging from 284 to 665 nm in ES fibers, and from 884 nm at 3 um in RJS fibers). Osteoblast viability within the scaffolds was assessed in vitro after 7, 14, and 21 days, through a combination of metabolic activity as cell viability, proliferation, alkaline phosphatase activity, and calcium deposition assays. The PCL:nHap:CNT fibers, at 14 days showed high enzymatic activity and calcium deposition compared with neat PCL, for both methods. Besides, bone marrow mesenchymal stem cells (BMMSCs) were seeded on and in the scaffolds and implanted in a rat model to assess their potential to heal critical bone defects in calvaria, compared to acellular scaffolds. Increased bone formation occurred through the combination of three characteristics: the presence of nHap:CNT nanoparticles, morphology surface evidenced by the RJS fibers, and scaffolds seeded with BMMSCs at 6 weeks of surgery. Our study showed the promising potential of well-defined combinations of suitable scaffolds seeded with BMMSCs for enhanced tissue engineering applications.

Keywords: Polycaprolactone; nanohydroxyapatite, carbon nanotubes, electrospinning; rotary jet spinning; osteoblast differentiation; bone marrow mesenchymal stem cells.

Introduction

The replacement or repair of bone tissue damaged from trauma or disease represents an important current clinical challenge. Among current treatments, bone grafting using autografts is still considered the gold standard method due to its greater osteogenic capacity. However, this approach is limited by the amount of bone graft harvest as well as it adds a degree of morbidity [1-3]. Other clinical available grafts are allografts and xenografts. Allografts are the second most used in orthopedic surgical as an alternative to autologous grafts. Nonetheless, they demonstrate a lower osteogenic capacity [1, 4]. Xenografts, i.e. animal bone-derived biological apatite, available in large quantities, are considered as a favorable biomaterial in bone tissue engineering [5-7]. Besides, allografts and xenografts show potential for infections and graft rejection presenting histocompatibility antigens different from those from the receptor [3, 6-8]. To address these limitations, natural and synthetic biomaterials have been explored as alternatives for bone replacements. Such materials must be capable of regenerating native bone tissue efficiently.

Numerous polymeric fibers have been extensively studied as a promising biomaterial for use as scaffolds for bone tissue engineering applications. They can be synthesized from various types of natural or synthetic polymers and can be tailored per specific need. Besides, they are largely similar to the native extracellular matrix [9, 10]. Poly (ε-caprolactone) (PCL) is a biodegradable hydrophobic synthetic polymer, with a semi-crystalline nature, and are less expensive. They are commonly used for the development of scaffolds in both bone and cartilage tissue engineering, and drug delivery devices [11]. Besides, PCL has been approved by the United States Food and Drug Administration (FDA) for certain applications [11, 12]. Further, the methods mostly used to design ultrathin and fibers are electrospinning (ES) and Rotary Jet Spinning (RJS). ES is a widely used and is a relatively cost-effective method as it uses an external electric field to create fibers, which depends on the conductivity of the solution and also has a low production rate [13-16]. In contrast, RJS is a simple method that provides higher production rates, uses a high-speed rotating disk to fabricate aligned fibers which depend on a highly volatile solution [16-18]. Despite the differences between the techniques, they both show promise as scaffolds for various biomedical applications [14, 19-21].

Strategies to improve the bioactivity, biomimetic and mechanical properties of biomaterials for bone tissue engineering have been widely studied. Technologies based on well-defined

combinations of osteoconductive biomaterial scaffolds, with osteogenic properties and suitable scaffolds, are very attractive for bone reconstructive surgery and have been shown successful in stimulating osteogenesis [22-24].

Incorporating carbon nanotubes (CNT) and hydroxyapatite (nHap) nanoparticles into polymeric matrices can be an alternative to improve the PCL fiber characteristics, offering greater potential in the tissue regeneration process. In addition, nHap has been extensively studied as an artificial bone substitute due to its similarity to the mineral component of natural bone, which offers an additional advantage as an osteoconductive material that can promote the rate of bone regeneration [25-27]. However, nHap has unsuitable mechanical properties restricting its use [28, 29]. Strategies to improve this problem without sacrificing its biocompatibility are to incorporate some reinforcement materials, such as zirconia [30], nanodiamond [31], alumina, carbon fibers [32], CNT and others [33-35]. CNTs have aroused intense interest due to their outstanding mechanical and physicochemical properties, and ability to mimic the nanoscale dimensions of HA and collagen fibers in natural bone [36, 37]. The superficial modification of CNT by exposure to oxygen plasma is a more effective way to introduce functional groups, thus changing its wettability and ability for incorporation into polymer composites [38, 39]. The hydrophilic characteristic facilitates the adsorption of proteins which are important in mediating cell adhesion, growth, and the formation of the extracellular matrix [40, 41]. Therefore, it is considered that a combination of CNTs with synthetic polymeric materials would be more effective for tissue engineering applications.

Further, there is a significant interest in the using implantable biomaterials in combination with stem cells (SCs) to minimize tissue damage and promote tissue healing [23, 42, 43]. SCs have attracted great interest due to their ability to differentiate into different cell lineages, paving the way for many studies based on stem cell therapies to fight various diseases and to repair tissue. Stem cells can be isolated from embryos, fetuses, or adults. Using adult stem cells (ASCs) is well accepted by society and does not involve the same ethical and religious considerations as seen with the use of stem cells from embryos or fetuses. Besides, ASCs can be isolated from several organs and tissues [44-46]. Particularly, bone marrow stem cells (BMSCs) remain the best source for obtaining these cells, as well as for use in cell therapies. The bone marrow comprises at least two kinds of stem cells, hematopoietic stem cells (HSC), which give rise to blood cells, and

mesenchymal stem cells (MSC), which is the best pluripotent cells among them, but make up a smaller proportion [45, 47, 48].

Although MSCs are easily obtained from many tissues, such as the umbilical cord, placenta, fat, lung, liver, and skin, those derived from adult bone marrow have been more intensively studied. BMMSCs have a self-renewal ability and multi-lineage differentiation capability, and they also have been reported to trans-differentiate into not only mesoderm lineages but also ectodermal and endodermal cells [47, 49-51]. Several studies have shown that BMMSCs can be effective in the repair or regeneration of myocardial tissues, bone tissue, tendon, cartilage, and meniscus [50-52]. Besides, pre-seeding scaffolds with BMMSCs have been considered as an approach for improving bone regeneration over acellular scaffolds. Many preclinical trials showed that this strategy enhances osteogenic capacity [23, 53-55]. Therefore, the combination of biomimetic scaffolds with the BMMSCs can provide a system to improve bone regeneration.

Due to the above, the focus of this in vitro and in in vivo study was to investigate the potential osteoconductive properties of PCL fibrous scaffolds with incorporated CNT and nHap nanoparticles, engineered from ES and RJS methods. After performing specific biological in vitro tests, BMMSCs were seeded on the engineered scaffolds and implanted in a rat model to assess their potential in the reconstruction of critical bone defects in the calvaria, compared to acellular scaffolds. As such, this study showed the promising potential of a well-defined combination of suitable nanocomposite scaffolds with seeded BMMSCs for improved bone tissue engineering applications.

Experimental Section

Materials

Polycaprolactone (PCL – M_w 80,000) was purchased from Sigma- Aldrich®. Chloroform (99%, Sigma- Aldrich®) and acetic acid (CH_3COOH, glacial – Synth) were used as solvents.

Cellular assays

Human osteoblasts (HOB - Promocell C-12720), Osteoblast Basal Medium (Promocell GmbH C27015), Penicillin/streptomycin (P/S; Hyclone), Supmix/Osteoblast (Promocell GmbH

C39615), MTS (CellTiter 96® AQueous One Solution Cell Proliferation Assay, G3581; Promega Corporation, Fitchburg, WI, USA), and Dulbecco's phosphate-buffered saline without calcium chloride and magnesium chloride (dPBS, Sigma Aldrich) were all used in this study.

Production of CNT:nHap nanoparticles and their incorporation into polymer fibers

Synthesis of superhydrophilic MWCNT

Multi-walled carbon nanotubes (MWCNT) were produced by a chemical vapor deposition method by a mixture of camphor ($C_{10}H_{16}O$, 84 wt.%) and ferrocene (Fe $(C_5H_5)_2$, 16%) as a catalyst and it was vaporized at 220 °C in an antechamber. The vapor was carried by an argon gas flow at atmospheric pressure to the chamber of a CVD furnace (850 °C), allowing for the deposition of MWCNT on the wall of the quartz tube. The purification process for the removal of Fe nanoparticles from the produced MWCNT was performed by a high-temperature annealing technique under an oxygen-free atmosphere (N_2) [56]. The functionalization of MWCNT was performed by incorporating oxygen-containing functional groups to provide them with superhydrophilic character. A direct pulsed current plasma reactor with a 1sccm rate oxygen flow, 85mTorr pressure, under -700 V and pulse frequency of 20 kHz at 50% of the duty cycle with 5-time intervals of 40 minutes each, were used for this process, as described elsewhere [57-59].

Synthesis of nHap

The nHap precipitation was completed using the following reagents: calcium nitrate tetrahydrate [Ca $(NO_3)_2.4H_2O$] and ammonium phosphate monobasic [(NH_4) H_2PO_4]. These concentrations were chosen so that Ca/P=1.67. Firstly, the solutions were prepared separately in which the powders were dissolved in 90 mL of deionized water. Then, the solutions were mixed simultaneously and 18 mL of ammonium hydroxide [NH_4OH] was added to the solution to fix the pH. Next, the mixture was sonicated using ultrasound (Ultrasonic Processor 500 W; 20 kHz; 13 mm probe; model: SO-VCX-500, SONICS) for 30 minutes. The resulting suspension was left for 72 hours in a 2,000 mL container and then washed with deionized water until the pH reached a constant value (~ 6). Then, the powder was placed in the oven for 48 h at 60°C and ground using an analytical mill (Model A11, IKA, with an engine speed of 28,000 rpm) to obtain the nHap powder.

Synthesis of MWCNT:nHap

Initially, the MWCNTs (1% m/v) were diluted in deionized water and then the salts for Hap: Ca $(NO_3)_2.4H_2O$ and (NH_4) H_2PO_4; (Ca/P=1.67) were added. The pH control was controlled with NH_4OH (pH ~10). The precipitations were subjected to ultrasound (Ultrasonic Processor 500 W; 20 kHz; 13 mm probe; model: SO-VCX-500, SONICS) for 30 minutes. The resulting suspension was left in the oven for 48 h at 60°C and ground using an analytical mill (Model A11, IKA, with an engine speed of 28,000 rpm) to obtain the MWCNT/nHap powder.

Electrospinning and rotary jet spinning of PCL fibers

The polymeric solutions were prepared with or without incorporation of nanoparticles, the material groups were PCL with CNT, nHap and nHap:CNT. ES was performed using PCL at 17% (w/t). The polymer solutions for this technique were dissolved in acetic acid. The solution was placed in a syringe (BD Yale, 5 mL) with a metal needle tip. ES was carried out at follows: 16 kV (Bertan 230®,), needle tip (Inbras, 23G), needle-collector distance of 10 cm, 0.8 mL h^{-1}, controlled temperature (23 ºC) and humidity (~ 30%). The fibers were randomly oriented and collected on an aluminum foil collector plate.

The RJS was performed using PCL at 15% (w/t) dissolved in chloroform. The system used for obtaining polymer fibers by rotary jet spinning was constructed consisting of a mounted rotatable nozzle, with an inner volume of 6 mL with two end holes 0.3 mm in diameter rotating on its vertical axis coupled to an MR– 115 Mini – Motor (speed of 3,000 rpm). The fibers were collected through static collectors. Extrusion was conducted at ambient temperature and a humidity at 30% – 45%.

Characterization

Scanning electron microscope (SEM)

Scanning electron microscopy (Hitachi S-4800) was used to characterize the surface of the samples. For this, the samples were prepared and coated with a thin layer of platinum using a sputter-coat system. The voltage was 3.0 kV.

Transmission electron microscopy (TEM)

TEM was performed using a JEM-1010, JEOL, Peabody, MA microscope operating at 80 kV. The fibers were electro and rotary-jet spun directly onto the copper TEM grids (300 mesh) for 10 seconds.

Differential scanning calorimetry (DSC)

Differential scanning calorimetry (DSC, Q10, TA instruments) was used to evaluate the thermal parameters from the produced fibers. For that, the following parameters were used: a heating rate of 10 ºC min^{-1}, the temperature ranged from -150 to 250 ºC, and an atmosphere of N_2 (at a flow rate of 50 mL min^{-1}). Sample weights ranged from 8 to 10 mg. To determine the degree of crystallinity (Xc) of the samples, the following equation was used:

Equation 1. Degree of crystallinity (%)

$$X_c = (\Delta H_m / \Delta H^o_m) \times 100\ \%$$

where ΔH_m corresponded to the heat of fusion of the endothermic peak of fusion and ΔH^o_m was the heat of fusion for the 100% crystalline raw PCL.

Fourier transform infrared spectrometry (FTIR)

FTIR measurements were made using a Perkin Elmer FTIR Imaging System, model Spotlight-400. The spectra were collected between 450 – 4000 cm^{-1}. The technique was used to analyze the functional groups on the polymeric fibers.

Mechanical tests

A mechanical tensile testing was conducted using TA Instruments RSA-G2. Samples were cut into 10×30x0.5 mm rectangular strips and fixed in the clamps of the machine. The clamps were moved apart at a rate of 0.1 mm/s at room temperature to simulate biological conditions. The

displacement rate was set to 10 mm/min at room temperature. From the stress-strain figures, Young's modulus and the strain at the break were calculated.

In vitro assays

Cell culture and sample sterilization

Human osteoblasts were cultured in Osteoblast Basal Medium supplemented with 1% Penicillin/Streptomycin (P/S) and Osteoblast Growth Medium SupplementMix in a 37 °C, humidified, 5% CO_2/95% air environment. Before all biological tests, all scaffolds (dimensions of 10 mm^2) were sterilized using UV irradiation for 30 minutes for each side. After that, the scaffolds were placed in 24-well tissue culture plates. Osteoblasts were seeded at a concentration according to the experiment carried out onto the samples of interest, described below.

Cell viability

MTS assays were used to determine cell viability. To evaluate the cytotoxicity of the cells, they were seeded at 20,000 cells/cm^2 onto the sterilized sample in each well of a 24-tissue culture well-plate and were then incubated under standard cell culture conditions. After 24 hours, the MTS reagent (1:5 ratio with cell culture media) was added to each well and incubated for 4 hours on the day of the measurement. Absorbance from each well was measured by a SpectraMax M3(MT05412) at 490 nm and a color change from pink to dark brown was seen. A standard curve was created with a known number of cells to correlate absorbance to cell numbers.

Cell proliferation

To determine cell proliferation, cells were analyzed after 7, 14 and 21 days of culture. For this, the cells were seeded at 5,000 cells/cm^2. For the proliferation assays, the media were changed every two days. The MTS reagent was added to each well and incubated for 4 hours on the day of the measurement. Absorbance from each well was measured.

Alkaline phosphatase assay

Alkaline phosphatase (ALP) is an enzyme produced by osteoblasts (bone-forming cells) to release phosphate groups for the formation of calcium phosphate in the bone. A BioAssay QuantiChrom™ Alkaline Phosphatase Assay Kit (DALP-250) was used for the colorimetric

kinetic determination of ALP activity. The working solution was prepared by mixing for each 96-well assay, 200 µL of the assay buffer, 5 µL of an acetate solution (final 5 mM), and 2 µL of the p-nitrophenylphosphate liquid substrate (10 mM). Two hundred microliters of distilled water and 200 µL of a calibrator solution were transferred into separate wells of a clear bottom 96-well plate. Then, 50 µL samples were carefully transferred into other wells, and 150 µL of the working solution was pipetted into the sample wells. The final reaction volume in the sample wells was 200 µL. The optical density was measured at 405 nm (t=0) and again after 4 minutes (t=4 minutes) on a plate reader. Results were normalized by subtracting the absorbance values of blank wells containing samples with no cells from those values measured for the samples with cells.

Calcium deposition

For the calcium deposition assay after 7, 14 and 21 days of cell culture, the cell-seeded scaffolds were washed three times using deionized water to remove calcium ions in the medium. Cells and the extracellular matrix were demineralized by adding 500 µm of 0.6M hydrochloric acid to each well and incubated at room temperature and shaken for 4 hours. Next, the resultant samples were collected after being centrifuged at 12,000 rpm at 4°C for 3 min and the supernatants were collected. Calcium concentrations were quantified using the Quanti-Chrom Calcium Assay Kit (BioAssay Systems) according to the manufacturer's instructions. Results were normalized by subtracting the absorbance values of blank wells containing samples with no cells from those values measured for the samples with cells.

Osteoblast cell characterization

In order to observe the osteoblast cell morphology along the polymeric scaffolds, scanning electron microscopy (SEM) was performed. Osteoblast cells were seeded at 20,000 cells cm^2 onto the sample for 24 hours. After the fibers were subjected to washing with PBS (x2), the PBS was removed and replaced by 1 mL of a fixative solution containing 2.5% of glutaraldehyde and 4% paraformaldehyde in PBS for 1 hour. After that, they were dehydrated in a series of acetone solutions (30%, 50%, 70%, 80%, 90%, and 100%), followed by rinsing with acetone plus HMDS (1: 1) and neat HMDS for 10 minutes each. The specimens were dried, platinum-coated and observed by Hitachi S-4800 SEM.

In vivo studies

Isolation and culture of BMMSCs

MSCs were obtained from the bone marrow of the femurs of 4 male Wistar rats. The tibia and femur bone were extracted and cleaned three times with a PBS solution, 2.5% chlorhexidine, and 70% alcohol. Subsequently, the ends of the bones (epiphyses) were extracted, and the bone marrow was washed with alpha minimum essential medium (a-MEM, Gibco-Invitrogen) with 10% fetal bovine serum (FBS) and 1% penicillin/streptomycin (Gibco, USA). The cells obtained were placed in a culture bottle and kept in an oven at 37ºC and 5% CO_2 until confluence. The culture medium was changed every four days of culture. Primary cells were used.

Before the surgery procedure, a part of the scaffolds group was seeded with BMMSCs. The $1x10^5$ BMMSCs were seeded onto the sterilized scaffolds and kept in an oven at 37ºC and 5% CO_2 for 24h before implanted.

Surgical procedures

Forty-eight male rats (100 days of age, Rattus norvegicus albinus; Wistar), weighing from 400 to 450 g were used. The experimental procedures were approved by the Animal Ethics Committee (CEUA, Protocol 07/2017) of the Institute of Science and Technology of the Campus of Sao Jose dos Campos/ UNESP. The animals were divided into four groups with six rats in each one: (I) group analyzed after 2 weeks, (II) group analyzed after 6 weeks, (III) the same as group I but seeded with BMMSCs, and (IV) the same as group II but seeded with BMMSCs. The animals were weighed and anesthetized with an intramuscular injection with a solution of xylazine hydrochloride 5 mg/kg (Anasedan®—Vetbrands, Jacareí—Brazil), and a Ketamine Hydrochloride 75-95 mg/kg (Dopalen®—Vetbrands, Jacaréi—Brazil) solution. After anesthesia, the surgical sites were submitted to trichotomy and antisepsis with an iodized alcohol solution. Access to the calvaria of the animal was made through the incision in the skin. A critical bone defect was made with a steel trephine drill (5 mm in diameter) under abundant and continuous irrigation with a physiological solution, aimed at avoiding overheating due to the friction of the drills with the bone. The bone defect was filled with the PCL and PCL: nHap: CNT material for both techniques without or with BMMSCs. Finally, the skin was sutured with silk thread #4 (Ethicon/Johnson & Johnson).

After surgery, an analgesic drug (sodium dipyrone monohydrate 150 mg/kg) was given subcutaneously every 8 h until 48 h after surgery. Euthanasia was carried out after 2 and 6 weeks using an anesthetic overdose administered intramuscularly.

Microtomography analyses (Micro-Ct)

The rat calvaria fragments were kept in 10% buffered formalin, pH 7.0. Before using microtomography, the fragments were washed and stored in 70% ethanol. The specimens then underwent three-dimensional (3D) microcomputer tomography analyses using SkyScan 1174 (SkyScan, Kontich, Belgium). Tomographic images were acquired at 70 keV and 702 μA, 360° rotation and images were reconstructed using NRecon software (Bruker-Skyscan) and Dataviewer® (Skycan 2011 Version 1.4.4 64 Bit) software was used for the quantification of the bone formation CT-Analyzer® software (2003-11SkyScan, 2012 Bruker MicroCt Version 1.12.4.0) and for the reconstruction of images. CT-Vol® software (SkyScan 7.0) was used. Thresholding was performed using a lower grey threshold limit of 50 and an upper grey threshold limit of 150. The following bone structural parameters were thus obtained: bone volume (BV), trabecular thickness (Tb.Th), trabecular number (Tb.N), and trabecular separation (Tb.Sp).

Histologic analysis

For all histology sections, the specimens were fixed in 10% buffered formaldehyde. Then the pieces were demineralized by immersion in an ethylenediaminetetraacetic acid solution (EDTA Titriplex III, Merck). After demineralization, the blocks were set in paraffin, and serial cross-sections of 5 μm thickness were obtained and stained with hematoxylin-eosin (HE). The histological sections were accessed blindly by a technician. The histomorphometric analysis was performed to quantify the area of new bone formation in three distinct regions of the defect: the lateral border and two in the center of the defect. Five sections containing the materials were digitized (5x) for each group, using Nikon Eclipse Ts2. After that, the new bone formation area was calculated using Image J (NIH) imaging software.

Statistical analysis

All experiments were conducted in triplicate and were repeated at least three different times. The statistical differences between the mean values and for comparison between the samples were determined using one-way ANOVA followed with a Tukey's multiple comparison test. Differences were considered statistically significant at $p < 0.05$.

Results and Discussion

Characterization

Fig. 1A shows the TEM micrographs of the nanoparticles. nHap has needle-like crystals and showed a diameter of ~20 nm **(Fig.1-A1)**. Multi-walled CNT is a well-crystalline bamboo-like structure. **Fig. 1-A2** shows details of the inner and outer diameters of ~10 and ~25 nm, respectively. **Fig 1-A3** exhibits both nanoparticles together (nHap:CNT). **Fig. 1B-C** shows the SEM micrographs of the surfaces of the PCL produced by ES and RJS with different nanoparticles incorporated and their correspondent histograms of the fiber diameter distribution. Furthermore, we can observe the success of the incorporation of nanoparticles in the polymeric fibers for both methods, as shown by TEM images. The ES fibers had diameters in the nanoscale with smooth characteristics. A slight difference in fiber diameter can be observed after the nanoparticles were incorporated **(Fig. 1B)**. Despite that, the surface morphology of the ES fibers remained similar. Regarding the RJS fibers at 15 % (wt), **Fig. 1C** shows thicker fibers at the microscale which presented visually more roughness (porous) than the ES fibers. After the incorporation of the nanoparticles, the diameters of the fibers decreased. Furthermore, it can be observed that the morphology of the fibers changed when the nanoparticles were incorporated for the PCL:nHap and the PCL:CNT in which they were visually more smooth than the rough fibers **(Fig.1-C2-3)**. However, the incorporation of both of the nanoparticles (PCL:nHap:CNT) exhibited the same morphology as the raw PCL (high roughness). The special roughness has been recognized to improve cell adhesion due to more exposed surface area [60].

Several additional material characterization studies were also conducted and are shown in supplementary file (Table S1, **Fig. S1-S2**).

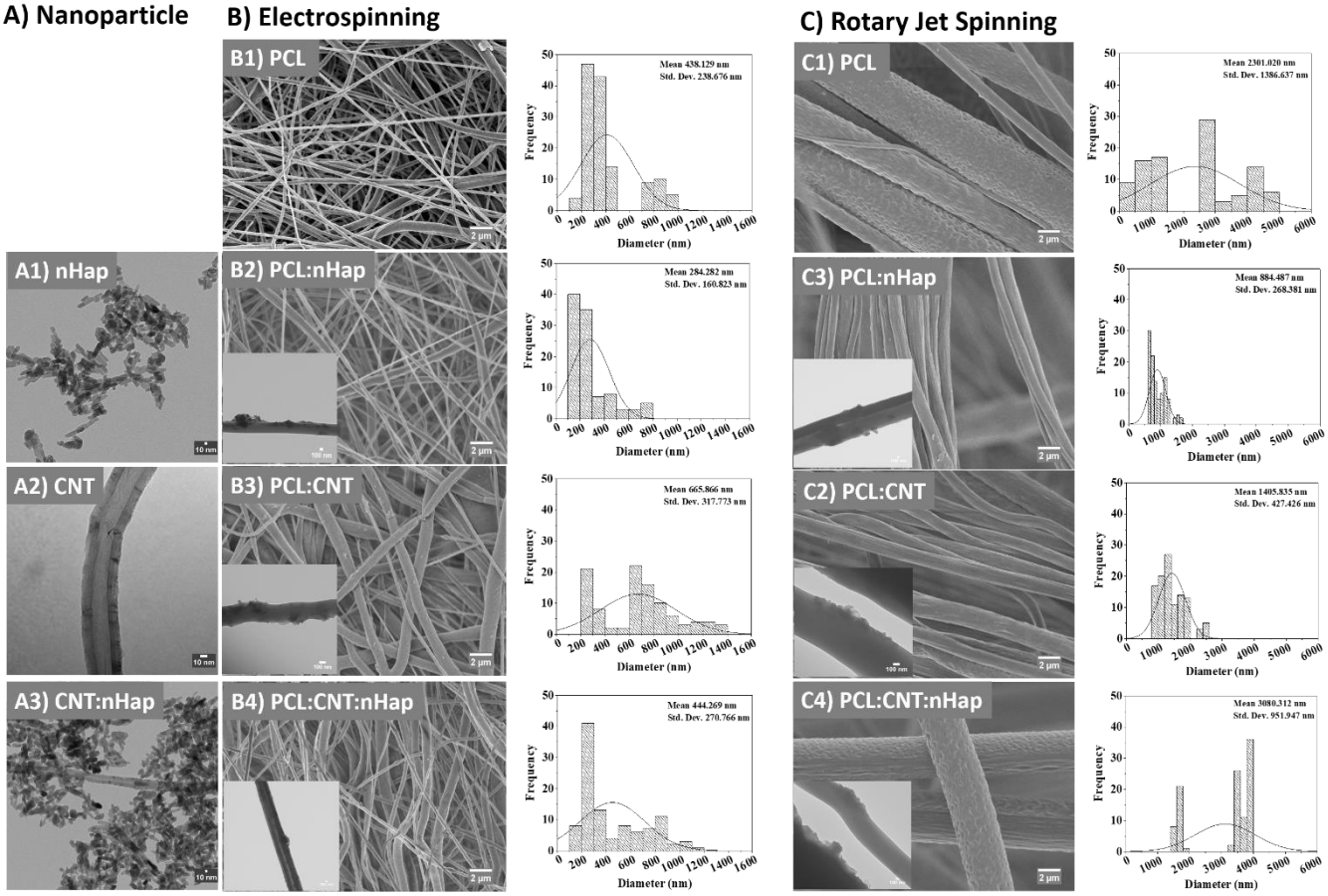

Figure 1. (A) Transmission electron micrographs (TEM) of the materials of interest to this study. **(A1)** nHap, **(A2)** multi-walled CNTs, and **(A3)** nHap:CNT composites. **(B and C**) Scanning electron micrographs (SEM), Transmission electron micrographs (TEM) and histograms of the fiber diameter distribution collected from the ES and RJS PCL fibers. **(B)** Micrographs obtained by electrospun fibers. **(B1)** PCL, **(B2)** PCL:nHap, **(B3)** PCL:CNT and **(B4)** PCL:nHap:CNT. **(C)** Micrographs obtained by rotary jet spun fibers. **(C1)** PCL, **(C2)** PCL:nHap, **(C3)** PCL:CNT and **(C4)** PCL:nHap:CNT. Distribution of PCL diameters as calculated by ImageJ. (Scale bars = 2 μm). Details of incorporation of nanoparticles in the polymeric fibers by ES and RJS by TEM. (Scale bars = 100 nm).

Osteoblast cell characterization

The geometry of a scaffold is able to control cell behavior and morphology and can be adapted according to tissue regeneration needs [61, 62]. Therefore, investigation of cellular morphology allowed us to directly observe cellular interactions dependent on the arrangement of the PCL scaffolds. **Fig. 2** shows the differences in cell shape and morphology according to the fabrication method used. It was observed that the cells colonized the intraporous space within the PCL scaffolds synthesized by RJS, unlike PCL fibers fabricated by ES in which the cells remained adherent to the surface. These data can be correlated with the greater distance between fibers as shown by the RJS fibers, forcing the cells to fill the spaces between them, creating a beneficial environment for cellular ingrowth into a 3D mesh. These characteristics were observed by Ura *et al* [62], which analyzed human osteoblast cell morphology on different surface architectures of electrospun PMMA. Also noted here was the significant number of cellular filopodia on the edges and the close interaction of the cells on all fibers produced by ES (arrows in **Fig. 2**). Whereas in fibers produced by RJS, the filopodia were observed only at the edges. Filopodia have an essential role in numerous biological processes, including sensing, migration, wound-healing, and cell-cell interactions [63]. Importantly, the protrusions of cell membranes via filopodia facilitate osteoblast adhesion and migration [62, 64].

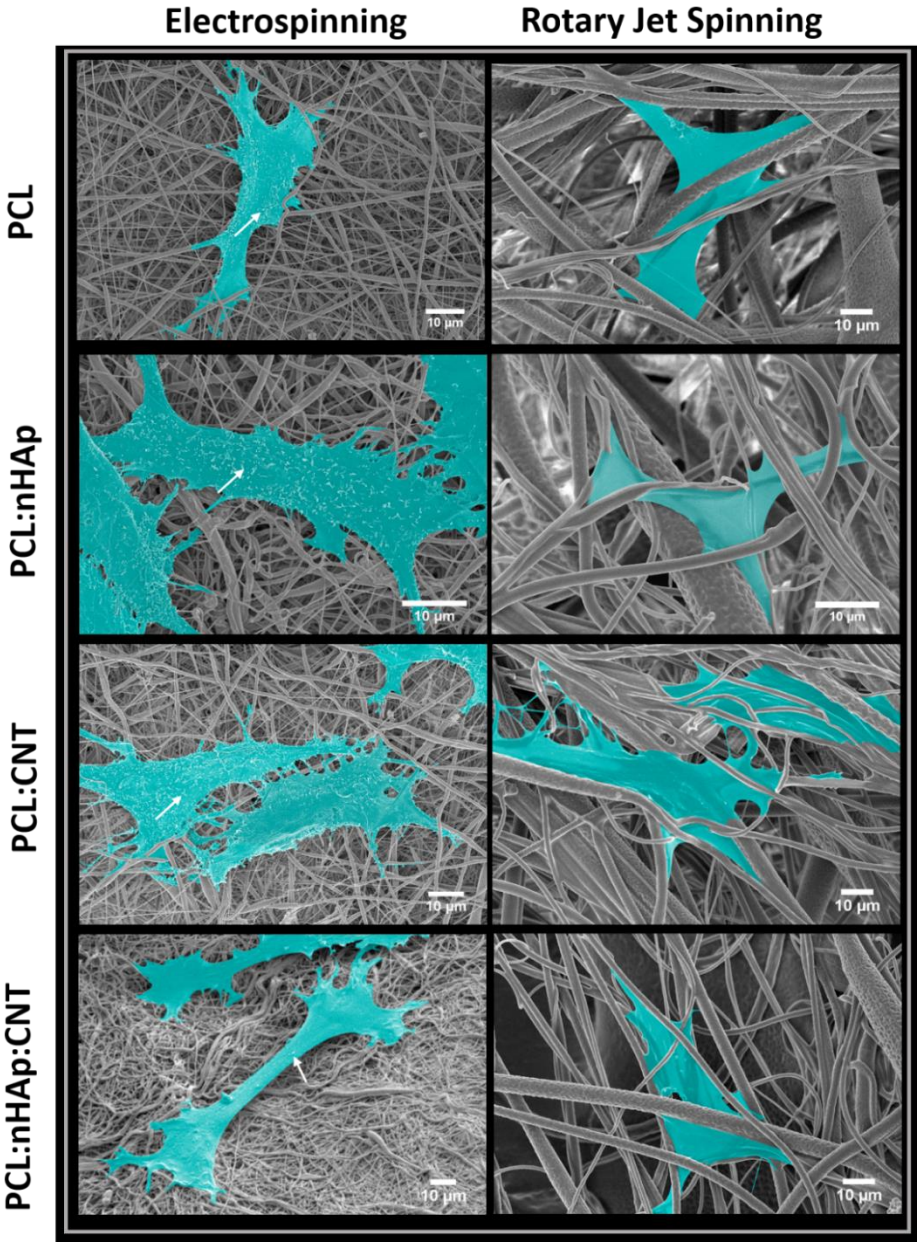

Figure 2. SEM images of osteoblast cells (colored in green) adherent to the fibrous mats. Micrographs on the left show HOB cells over the electrospun fibers (neat PCL; PCL:nHap; PCL:CNT and PCL:nHap:CNT), arrows indicate of filopodia in the edges and over the cell surface.

Micrographs on the right show HOB cells over the rotary jet spun fibers (neat PCL; PCL:nHap; PCL:CNT and PCL:nHap:CNT). (Scale bars = 10 μm.)

In vitro assays

HOB biological activity in contact with fiber structures was assessed as a means to determine their possible application in bone tissue regeneration **(Fig. 3A-F)**. All the scaffolds produced were analyzed (Supplementary File. **Fig. S3**). However, based on the results, two groups from each technique were highlighted: neat PCL as a control and the PCL:nHap:CNT, which both showed enhanced osteoblast activity for both fabrication methods. The cellular metabolic activity was monitored after 7 and 14 days of culture **(Fig. 3A-B)**. A gradual increase in cell proliferation was observed, independent of the scaffolds and each technique. For the ES method, the PCL fibers showed a 10% more cell density than PCL:nHap:CNT, whereas for the RJS fibers, there was no significant difference between the materials. Cell proliferation correlates with the wettability of a surface since that control initial protein adsorption important for cells to attach[65], and therefore, despite the hydrophobic feature of our materials, they showed great potential for each of the fibers to induce and maintain osteoblast proliferation, without presenting unwanted cytotoxicity.

ALP is a classical biomarker used to determine the potential of osteoblasts to deposit bone, and it is associated with early osteoblast differentiation (ECM mineralization) [66, 67]. **Fig. 3C-D** shows the ALP activity levels after 7 and 14 days of culture. On day 14, ALP expression increased significantly compared to day 7 for both fibers and methods (PCL and PCL:nHap:CNT by ES $p<0.0001$, and PCL and PCL:nHap:CNT by RJS $p<0.001$, $p<0.0001$, respectively). Besides, the fibers containing nanoparticles showed greater osteoblast ALP activity compared to the neat PCL fiber, precisely 55 % more for ES and 77% more for RJS on day 14.

Calcium deposition was similar to ALP **(Fig. 3E-F)**, showing an increase in calcium deposition after 7 and 14 days for all groups ($p<0.0001$). The groups with incorporated nanoparticles demonstrated higher calcium deposition compared to neat PCL for both methods, precisely 30% more in ES and 12% more in RJS on day 14. Although fibers with nanoparticles fabricated by ES on day 14 showed a 2-fold more expression of ALP and a 1-fold more calcium deposition than fibers from RJS, they both showed high enzymatic activity and calcium deposition. These data can be correlated with the presence of the nanoparticles. nHap is a classical bioceramic carrier of osteoinductive growth factors [68], confirming the crucial role of the nHap component

in the stimulation of osteoblasts. These findings agree well with data presented by Shitole et al. who showed that the PCL with nHa significantly improved ALP activity and mineral deposition after 10 days [69].

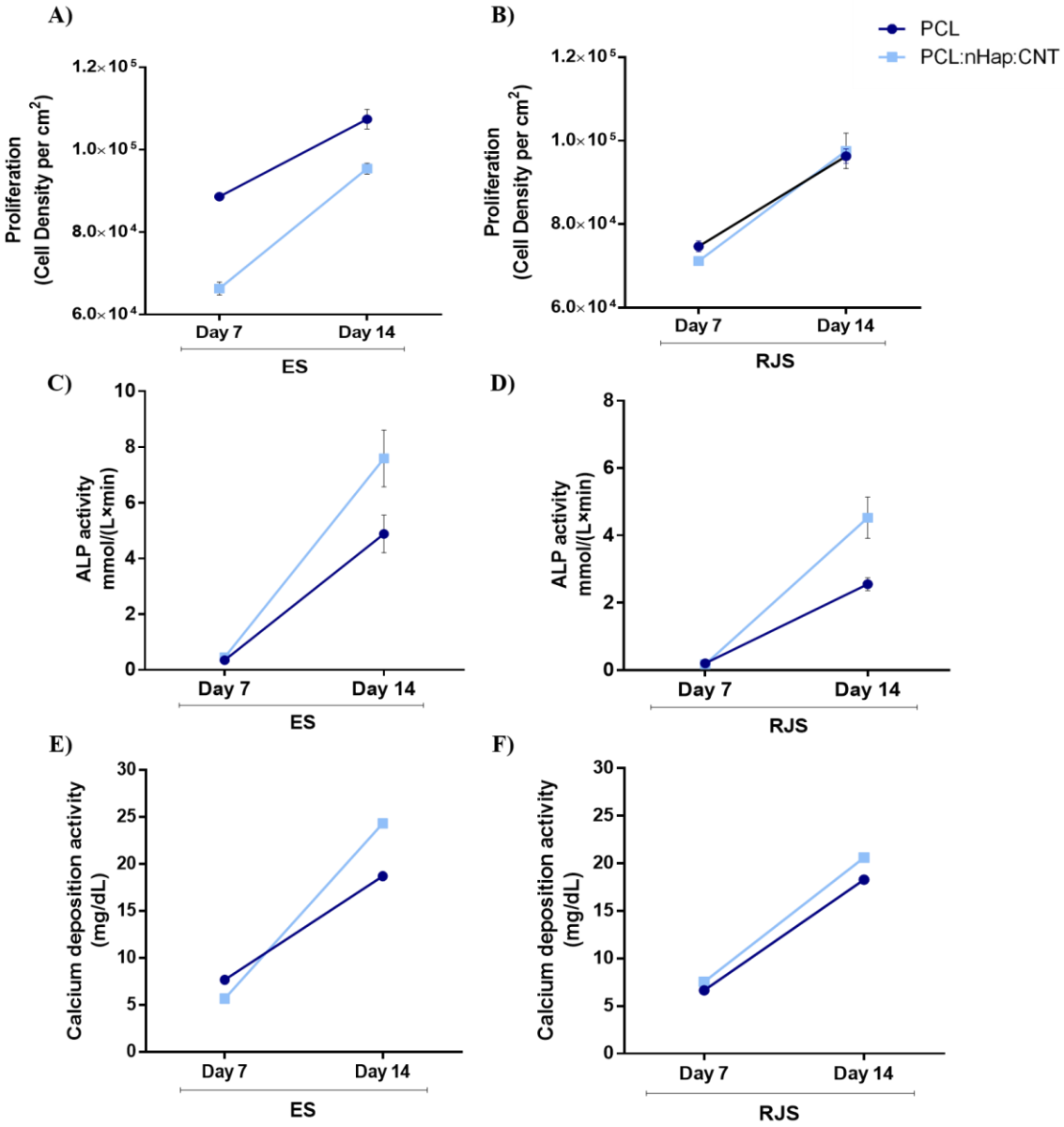

Figure 3. Osteoblast assays. **A-B)** Osteoblast proliferation on **(A)** ES fibers and **(B)** RJS fibers. **C-D)** Alkaline phosphatase (ALP) activity by osteoblasts on **(C)** ES fibers and **(D)** RJS fibers. **E-F)** Calcium deposition by osteoblasts on **(E)** ES fibers and **(F)** RJS fibers. Assays were performed after 7 and 14 days. Results were normalized by subtracting the absorbance values of blank wells containing samples without any cells from those values measured for the samples with cells. Values are mean ± SD, N=3, considered statistically significant at $p < 0.05$.

In vivo studies

For the in vivo analysis, **Fig. 4A** shows the 3D reconstruction of the rat calvaria defect (5mm). These images represent the 3D reconstruction 6-weeks after implantation of neat PCL and PCL:nHap:CNT for both methods without and with BMMSCs. The 3D reconstruction of the 2-week after implantation can be seen in the supplementary file (**Fig. S4A**). Based on the reconstructed 3D image, new bone regenerated in the peripheral and central parts of the defect and was noticed mainly on the material groups with nanoparticles incorporated and seeded with BMMSCs. This observation suggested the success of combining these cells with the biomaterial to improve bone regeneration. Likewise, all parameters of microtomography (Tb.Th, Tb.N, and Tb.Sp) are included in the supplementary file showing the same trends (**Fig. S4B**). The bone volume (BV) measurements for the groups after 2 and 6 weeks without and with BMMSCs are shown in **Fig. 4B-C**. The fibers containing nanoparticles by ES after 2 weeks exhibited enhanced BV at a statistical difference ($p < 0.01$) compared with neat PCL, whereas for the RJS fibers, the opposite was observed ($p<0.0001$). After 6 weeks, there was no significant difference between the fibers fabricated using the same method, however, comparing the methods, the ES fibers showed a greater BV than the RJS fibers (PCL: $p<0.0001$ and PCL:nHap:CNT: $p<0.05$) (**Fig. 4B)**. In the scaffolds seeded with BMMSCs **(Fig. 4C)**, the RJS fibers with nanoparticles showed a greater BV after 6-weeks, with a significant difference ($p<0.0001$) compared with PCL and PCL:nHap:CNT fabricated by ES.

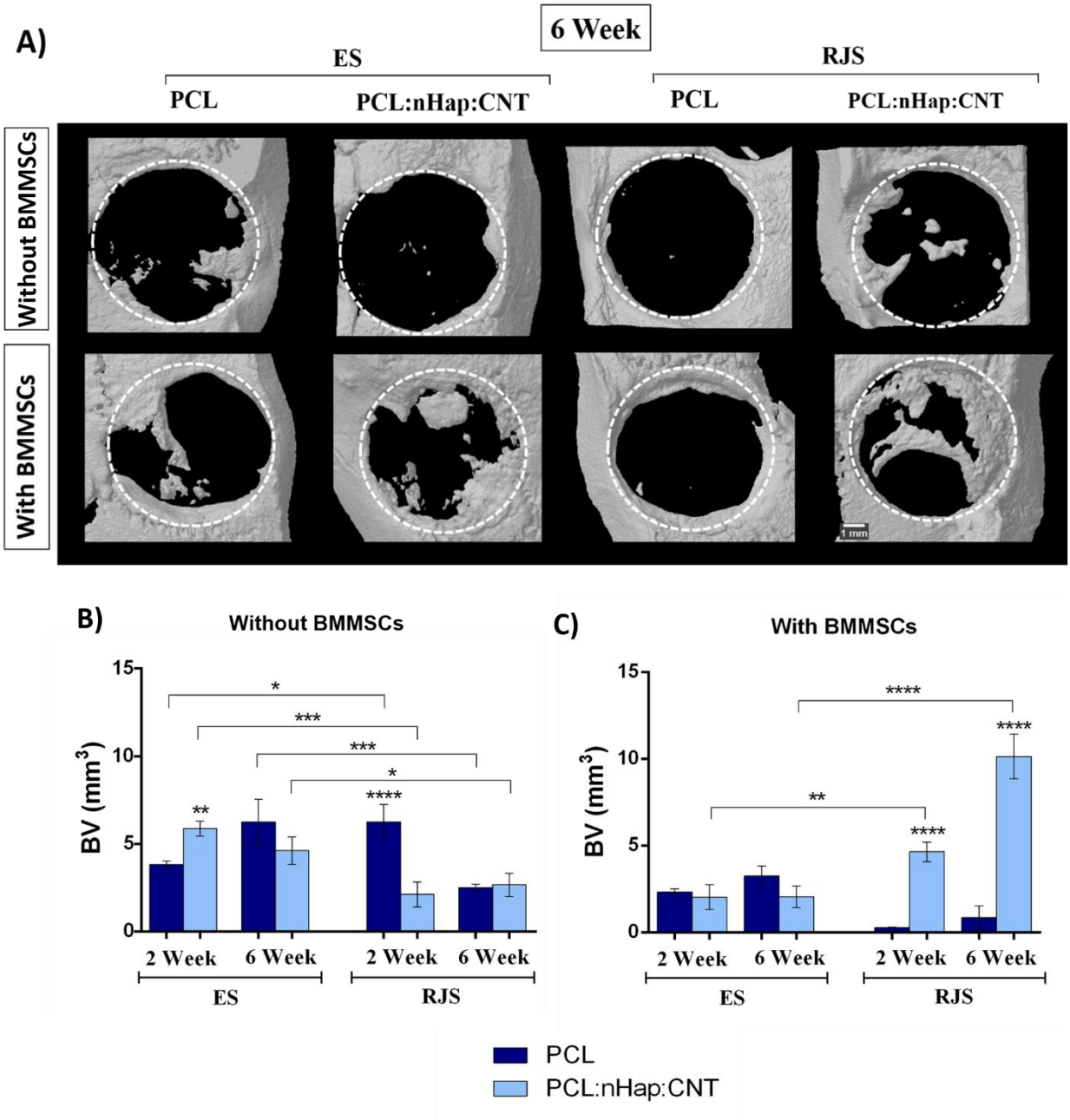

Figure 4. A) Reconstructed 3D micro-CT images of rat calvaria implanted with PCL and PCL:nHap:CNT by ES and RJS after 6 weeks without or with seeded BMMSCs. The dotted circles indicate the original defect. Scale bar: 1mm. **B)** Micro-CT assessment of bone volume (BV) in ES and RJS groups without cells. C) Micro-CT assessment of bone volume (BV) in ES and RJS groups with BMMSCs. All were analyzed at two time points: 2 and 6 weeks. Statistically significant (*

p< 0.05, ** p< 0.01, *** p<0.001 and **** p< 0.0001). Asterisk alone means comparison with the neat PCL as the same method.

Histology results were consistent with micro-CT results. The histology images (**Fig. 5A**) show the 6-week groups after implantation with PCL and PCL:nHap:CNT for both methods without and with BMMSCs. Active bone formation was observed in all analyzed scaffolds. Besides, bone neoformation occurred both in the peripheral and central parts of the defect, mainly in groups with incorporated nanoparticles seeded with BMMSCs, more details can be seen in the supplementary file **(Fig. S5A-B)**. The immature bone trabeculae presented osteocytes in lacunas (arrow), and osteoblasts around the trabecular bone (dashed arrow). The defect area is composed predominantly of vascularized repair tissue. The quantitative comparison between groups, obtained through histomorphometric analysis, is displayed in **Fig. 5B-C**. The incorporation of nanoparticles does not seem to have enhanced bone neoformation for both methods. The neat PCL fiber showed significantly more bone neoformation after 6-weeks compared with the PCL with nanoparticles ($p<0.01$) for both methods. Comparing the methods, the neat PCL fiber by ES has more bone neoformation than neat PCL fiber by RJS ($p<0.05$). The opposite behavior was observed in groups seeded with BMMSCs (**Fig. 5C**). The fibers with incorporated nanoparticles fabricated by RJS show greater bone neoformation than those from neat PCL ($p<0.001$) after 6-weeks. Therefore, iincreased bone formation occurred through the combination of three characteristics: the presence of nHap:CNT nanoparticles, morphology surface evidenced by the RJS fibers, and scaffolds seeded with BMMSCs at 6 weeks of surgery.

HAp has excellent osteoinductive properties and is considered an excellent bio-ceramic material to produce biocomposites to promote bone regeneration [41, 70]. Groppo et al. (2017) showed similar results to the ones observed here. They observed a significant improvement in bone healing in rat subcritical calvarial bone defects using micro-HAp added to a PCL membrane [25]. Furthermore, several additional researchers have reported benefits in its use [68, 71].

Besides,the RJS fibers had rough surface fibers compared to ES fibers that presented smooth fibers, which can be observed in **Fig. 1**, and has also been reported by previous studies [16]. Also, RJS fibers showed larger spaces between the fibers, allowing the cells to enter the scaffold, unlike ES, which allowed a culture only on the surface **Fig. 2**.Studies revealed that surface roughness and 3D dimensions of the scaffolds can affect cellular functions since *in vivo*, cells interact with an extracellular matrix (ECM) with nano and microscale features (e.g., protein complexes, focal

adhesion sites, etc.). Besides, several studies showed that a rough surface is advantageous to promote the osteogenic differentiation of BMSCs [72-75]. Banik et al. showed that macro-micro roughness of titanium is advantageous over smooth titanium and PEEK implants to regulate the early attachment, migration, and differentiation of human mesenchymal stem cells (hMSCs) [76]. Similar results have been shown by Yang et al. in which a high rough surface topography of HA promoted osteogenic differentiation of hBMSCs [77]. Besides, studies show that 3-D systems support a higher density of cells, promoting the formation of aggregates and better cell-cell interactions, which determine cellular functions [78]. Therefore, this property can be the reason for the greater bone growth result from this present study, although clearly more studies would be needed to prove this. However, a comparison of the same material without and with BMMSCs showed that the morphology of the material did not have a direct influence on improving bone neoformation, but with the combination with BMMSCs, such a difference was observed. Bone marrow MSCs are pluripotent stem cells with the potential to differentiate into multiple mesenchyme-lineage cell types, like osteoblasts, chondrocytes, and adipocytes, and are regarded as an excellent source of cells for cell therapy-based approaches [49, 79]. It has been reported that hydrogels with BMMSCs increase femoral bone formation compared with acellular hydrogels [80]. Additional research shows that the PVDF-TrFE/BT membrane combined with osteoblastic cells differentiated from MSC from bone marrow in a calvaria defect rat to increase bone formation [81]. Therefore, in this study, greater bone neoformation occurred through the combination of the three characteristics presented, specifically the presence of nHAp and CNT nanoparticles, morphology surfaces produced by RJS fibers, and BMMSCs.

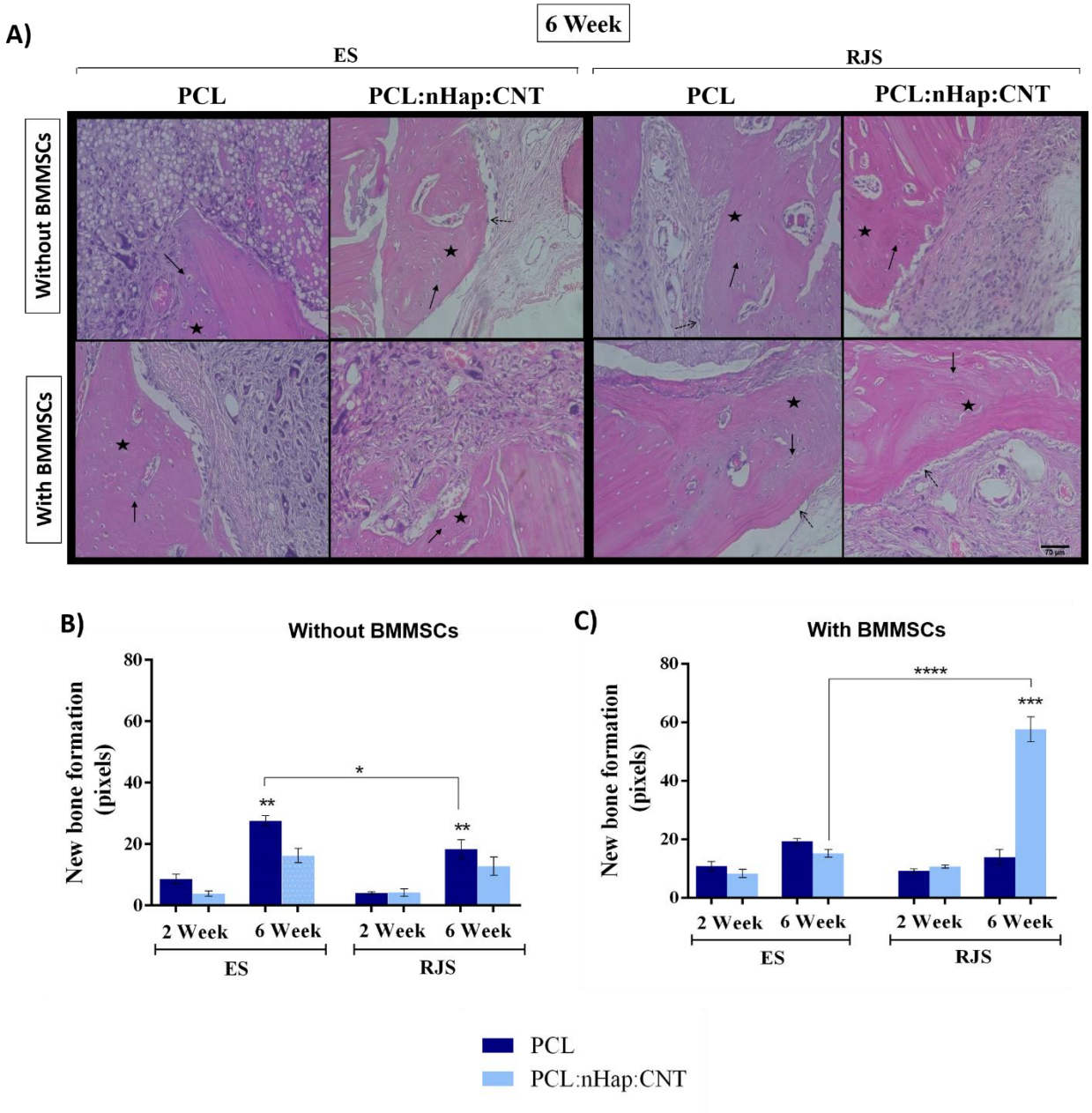

Figure 5. Histological and histomorphometric analysis. **A)** Histological images of rat calvaria defects filled with different materials at 6 weeks: Stars mark the active bone neoformation, the arrows show osteocytes in lacunas, and dashed arrows mark osteoblasts around the trabecular bone. All groups X20.0 magnification. **B)** Bone neoformation analysis in ES and RJS groups without cells. **C)** Bone neoformation analysis in ES and RJS groups with BMMSCs. All were analyzed at two timepoints: 2 and 6 weeks. Statistically significant (* $p < 0.05$, ** $p < 0.01$, ***

p<0.001 and **** p<0.0001). Asterisk alone means comparison with the neat PCL as the same method.

4. **Conclusions**

In conclusion, we have shown here that the choice of material and surface topography combined with cells are key factors that can favor influence bone neoformation. We have demonstrated that the combination of nHap and CNT nanoparticles with a rough surface as fabricated by RJS for the PCL fibers and BMMSCs favored the repair of a rat calvarial defect after 6 weeks. On the contrary, the individual use of these parameters did not show any significant difference between groups without nanoparticles, besides presenting low bone neoformation. These findings suggest that PCL:nHap:CNT by RJS scaffolds seeded with BMMSCs is a potentially advantageous material in the field of guided bone tissue regeneration.

Acknowledgements

This work was supported by the National Council for Scientific and Technological Development (CNPq, #303752/2017-3 and #404683/2018-5 to AOL and #304133/2017-5 and #424163/2016-0 to FRM). MMMP has received financial support from Fundação de Amparo à Pesquisa do Estado de São Paulo (FAPESP, 2014/16295-2) and Coordination for the Improvement of Higher Education Personnel (CAPES, 88887.116351/ 2016-00). The co-contributors from Northeastern University would like to thank Northeastern University for funding.

References

[1] Wang W, Yeung KWK. Bone grafts and biomaterials substitutes for bone defect repair: A review. Bioactive Materials. 2017;2:224-47.
[2] Nandi S, Roy S, Mukherjee P, Kundu B, De D, Basu D. Orthopaedic applications of bone graft & graft substitutes: a review. Indian Journal of Medical Reseach. 2010;132:15-30.
[3] Damien CJ, Parsons JR. Bone graft and bone graft substitutes: a review of current technology and applications. Journal of applied biomaterials : an official journal of the Society for Biomaterials. 1991;2:187-208.
[4] William Jr G, Einhorn TA, Koval K, McKee M, Smith W, Sanders R, et al. Bone Grafts and Bone Graft Substitutes in Orthopaedic Trauma Surgery: A Critical Analysis. JBJS. 2007;89:649-58.
[5] Qiao W, Liu R, Li Z, Luo X, Huang B, Liu Q, et al. Contribution of the in situ release of endogenous cations from xenograft bone driven by fluoride incorporation toward enhanced bone regeneration. Biomaterials Science. 2018;6:2951-64.
[6] Liu Q, Huang S, Matinlinna J, Chen Z, Pan H. Insight into Biological Apatite: Physiochemical Properties and Preparation Approaches. BioMed research international. 2013;2013:929748.
[7] Bracey DN, Seyler TM, Jinnah AH, Smith TL, Ornelles DA, Deora R, et al. A porcine xenograft-derived bone scaffold is a biocompatible bone graft substitute: An assessment of cytocompatibility and the alpha-Gal epitope. Xenotransplantation. 2019;26:e12534.
[8] Hsieh J-L, Shen P-C, Wu P-T, Jou IM, Wu C-L, Shiau A-L, et al. Knockdown of toll-like receptor 4 signaling pathways ameliorate bone graft rejection in a mouse model of allograft transplantation. Scientific Reports. 2017;7:46050.
[9] Zhang Y, Tong Y, Pan X, Cai H, Gao Y, Zhang W. Promoted Proliferation of Hematopoietic Stem Cells Enabled by a Hyaluronic Acid/Carbon Nanotubes Antioxidant Hydrogel. Macromolecular Materials and Engineering. 2019;304:1800630.
[10] Dhandayuthapani B, Yoshida Y, Maekawa T, Kumar DS. Polymeric scaffolds in tissue engineering application: a review. International journal of polymer science. 2011;2011.
[11] Asghari F, Samiei M, Adibkia K, Akbarzadeh A, Davaran S. Biodegradable and biocompatible polymers for tissue engineering application: a review. Artificial cells, nanomedicine, and biotechnology. 2017;45:185-92.
[12] Malikmammadov E, Tanir TE, Kiziltay A, Hasirci V, Hasirci N. PCL and PCL-based materials in biomedical applications. Journal of Biomaterials Science, Polymer Edition. 2018;29:863-93.
[13] Eatemadi A, Daraee H, Zarghami N, Melat Yar H, Akbarzadeh A. Nanofiber: Synthesis and biomedical applications. Artificial cells, nanomedicine, and biotechnology. 2016;44:111-21.
[14] Khorshidi S, Solouk A, Mirzadeh H, Mazinani S, Lagaron JM, Sharifi S, et al. A review of key challenges of electrospun scaffolds for tissue-engineering applications. Journal of tissue engineering and regenerative medicine. 2016;10:715-38.
[15] Stojanovska E, Canbay E, Pampal ES, Calisir MD, Agma O, Polat Y, et al. A review on non-electro nanofibre spinning techniques. RSC advances. 2016;6:83783-801.
[16] Machado-Paula MM, Corat MAF, Lancellotti M, Mi G, Marciano FR, Vega ML, et al. A comparison between electrospinning and rotary-jet spinning to produce PCL fibers with low bacteria colonization. Materials Science and Engineering: C. 2020;111:110706.
[17] Mellado P, McIlwee HA, Badrossamay MR, Goss JA, Mahadevan L, Kit Parker K. A simple model for nanofiber formation by rotary jet-spinning. Applied Physics Letters. 2011;99:203107.
[18] Badrossamay MR, McIlwee HA, Goss JA, Parker KK. Nanofiber assembly by rotary jet-spinning. Nano letters. 2010;10:2257-61.
[19] Huang Z-M, Zhang Y-Z, Kotaki M, Ramakrishna S. A review on polymer nanofibers by electrospinning and their applications in nanocomposites. Composites science and technology. 2003;63:2223-53.

[20] Badrossamay MR, Balachandran K, Capulli AK, Golecki HM, Agarwal A, Goss JA, et al. Engineering hybrid polymer-protein super-aligned nanofibers via rotary jet spinning. Biomaterials. 2014;35:3188-97.
[21] Rogalski JJ, Bastiaansen CW, Peijs T. Rotary jet spinning review–a potential high yield future for polymer nanofibers. Nanocomposites. 2017;3:97-121.
[22] Taraballi F, Bauza G, McCulloch P, Harris J, Tasciotti E. Concise Review: Biomimetic Functionalization of Biomaterials to Stimulate the Endogenous Healing Process of Cartilage and Bone Tissue. STEM CELLS Translational Medicine. 2017;6:2186-96.
[23] Yuan N, Rezzadeh KS, Lee JC. Biomimetic Scaffolds for Osteogenesis. Receptors Clin Investig. 2015;2:898.
[24] Caldwell K, Berg J. Nanoparticles as Interphase Modifi ers in Fiber Reinforced Polymeric Composites: A Critical Review. Reviews of Adhesion and Adhesives. 2017;5:1-54.
[25] Groppo MF, Caria PH, Freire AR, Figueroba SR, Ribeiro-Neto WA, Bretas RES, et al. The effect of a hydroxyapatite impregnated PCL membrane in rat subcritical calvarial bone defects. Archives of Oral Biology. 2017;82:209-15.
[26] Teotia AK, Raina DB, Singh C, Sinha N, Isaksson H, Tägil M, et al. Nano-hydroxyapatite bone substitute functionalized with bone active molecules for enhanced cranial bone regeneration. ACS Applied Materials & Interfaces. 2017;9:6816-28.
[27] Gomes D, Santos A, Neves G, Menezes R. A brief review on hydroxyapatite production and use in biomedicine. Cerâmica. 2019;65:282-302.
[28] Turon P, Del Valle LJ, Alemán C, Puiggalí J. Biodegradable and biocompatible systems based on hydroxyapatite nanoparticles. Applied Sciences. 2017;7:60.
[29] Zakaria SM, Sharif Zein SH, Othman MR, Yang F, Jansen JA. Nanophase hydroxyapatite as a biomaterial in advanced hard tissue engineering: a review. Tissue Engineering Part B: Reviews. 2013;19:431-41.
[30] Yugeswaran S, Yoganand C, Kobayashi A, Paraskevopoulos K, Subramanian B. Mechanical properties, electrochemical corrosion and in-vitro bioactivity of yttria stabilized zirconia reinforced hydroxyapatite coatings prepared by gas tunnel type plasma spraying. Journal of the mechanical behavior of biomedical materials. 2012;9:22-33.
[31] Chen X, Zhang B, Gong Y, Zhou P, Li H. Mechanical properties of nanodiamond-reinforced hydroxyapatite composite coatings deposited by suspension plasma spraying. Applied Surface Science. 2018;439:60-5.
[32] Zhao X, Zhang L, Wang X, Yang J, He F, Wang Y. Preparation and mechanical properties of controllable orthogonal arrangement of carbon fiber reinforced hydroxyapatite composites. Ceramics International. 2018;44:8322-33.
[33] White AA, Best SM, Kinloch IA. Hydroxyapatite–carbon nanotube composites for biomedical applications: a review. International Journal of Applied Ceramic Technology. 2007;4:1-13.
[34] Zhao X, Chen X, Zhang L, Liu Q, Wang Y, Zhang W, et al. Preparation of nano-hydroxyapatite coated carbon nanotube reinforced hydroxyapatite composites. Coatings. 2018;8:357.
[35] Lawton K, Le H, Tredwin C, Handy RD. Carbon Nanotube Reinforced Hydroxyapatite Nanocomposites As Bone Implants: Nanostructure, Mechanical Strength And Biocompatibility. International journal of nanomedicine. 2019;14:7947.
[36] Harrison BS, Atala A. Carbon nanotube applications for tissue engineering. Biomaterials. 2007;28:344-53.
[37] Mittal V. Polymer nanotubes nanocomposites: synthesis, properties and applications: John Wiley & Sons; 2014.
[38] Ajeesh G, Bhowmik S, Venugopal S, Varshney L, Baluch A, Park Y, et al. Influence of chemically and plasma-functionalized carbon nanotubes on high-performance polymeric nanocomposites. High Performance Polymers. 2016;28:570-80.

[39] Rodrigues BV, Silva AS, Melo GF, Vasconscellos LM, Marciano FR, Lobo AO. Influence of low contents of superhydrophilic MWCNT on the properties and cell viability of electrospun poly (butylene adipate-co-terephthalate) fibers. Materials Science and Engineering: C. 2016;59:782-91.
[40] Machado M, Lobo A, Marciano F, Corat E, Corat M. Analysis of cellular adhesion on superhydrophobic and superhydrophilic vertically aligned carbon nanotube scaffolds. Materials Science and Engineering: C. 2015;48:365-71.
[41] Wang P, Yu T, Lv Q, Li S, Ma X, Yang G, et al. Fabrication of hydroxyapatite/hydrophilic graphene composites and their modulation to cell behavior toward bone reconstruction engineering. Colloids and Surfaces B: Biointerfaces. 2019;173:512-20.
[42] Maglione M, Spano S, Ruaro ME, Salvador E, Zanconati F, Tromba G, et al. In vivo evaluation of chitosan-glycerol gel scaffolds seeded with stem cells for full-thickness mandibular bone regeneration. Journal of oral science. 2017;59:225-32.
[43] Stanovici J, Le Nail LR, Brennan MA, Vidal L, Trichet V, Rosset P, et al. Bone regeneration strategies with bone marrow stromal cells in orthopaedic surgery. Current Research in Translational Medicine. 2016;64:83-90.
[44] Khan WS, Rayan F, Dhinsa BS, Marsh D. An osteoconductive, osteoinductive, and osteogenic tissue-engineered product for trauma and orthopaedic surgery: how far are we? Stem cells international. 2012;2012:236231.
[45] Chiu RCJ. Bone-Marrow Stem Cells as a Source for Cell Therapy. Heart Failure Reviews. 2003;8:247-51.
[46] Squillaro T, Peluso G, Galderisi U. Clinical trials with mesenchymal stem cells: an update. Cell transplantation. 2016;25:829-48.
[47] Salem HK, Thiemermann C. Mesenchymal stromal cells: current understanding and clinical status. Stem cells. 2010;28:585-96.
[48] Méndez-Ferrer S, Scadden DT, Sánchez-Aguilera A. Bone marrow stem cells: current and emerging concepts. Annals of the New York Academy of Sciences. 2015;1335:32-44.
[49] Wei X, Yang X, Han Z-p, Qu F-f, Shao L, Shi Y-f. Mesenchymal stem cells: a new trend for cell therapy. Acta Pharmacologica Sinica. 2013;34:747-54.
[50] Caplan AI. Adult mesenchymal stem cells for tissue engineering versus regenerative medicine. Journal of cellular physiology. 2007;213:341-7.
[51] Han Y, Li X, Zhang Y, Han Y, Chang F, Ding J. Mesenchymal Stem Cells for Regenerative Medicine. Cells. 2019;8:886.
[52] Mistry AS, Mikos AG. Tissue engineering strategies for bone regeneration. Regenerative medicine II: Springer; 2005. p. 1-22.
[53] Kargozar S, Hashemian SJ, Soleimani M, Milan PB, Askari M, Khalaj V, et al. Acceleration of bone regeneration in bioactive glass/gelatin composite scaffolds seeded with bone marrow-derived mesenchymal stem cells over-expressing bone morphogenetic protein-7. Materials Science and Engineering: C. 2017;75:688-98.
[54] Westhauser F, Weis C, Prokscha M, Bittrich LA, Li W, Xiao K, et al. Three-dimensional polymer coated 45S5-type bioactive glass scaffolds seeded with human mesenchymal stem cells show bone formation in vivo. Journal of Materials Science: Materials in Medicine. 2016;27:119.
[55] Zhang R, Li X, Liu Y, Gao X, Zhu T, Lu L. Acceleration of bone regeneration in critical-size defect using BMP-9-loaded nHA/ColI/MWCNTs scaffolds seeded with bone marrow mesenchymal stem cells. BioMed research international. 2019;2019.
[56] Antunes E, Almeida E, Rosa C, de Medeiros L, Pardini L, Massi M, et al. Thermal annealing and electrochemical purification of multi-walled carbon nanotubes produced by camphor/ferrocene mixtures. Journal of nanoscience and nanotechnology. 2010;10:1296-303.

[57] Ramos S, Lobo A, de Vasconcelos G, Antunes E, Trava-Airoldi V, Corat E. Influence of polar groups on the wetting properties of vertically aligned multiwalled carbon nanotube surfaces. Theoretical Chemistry Accounts. 2011;130:1061-9.
[58] Ramos SC, Vasconcelos G, Antunes EF, Lobo AO, Trava-Airoldi VJ, Corat EJ. Wettability control on vertically-aligned multi-walled carbon nanotube surfaces with oxygen pulsed DC plasma and CO2 laser treatments. Diamond and Related Materials. 2010;19:752-5.
[59] Lobo AO, Marciano FR, Ramos SC, Machado MM, Corat EJ, Corat MAF. Increasing mouse embryonic fibroblast cells adhesion on superhydrophilic vertically aligned carbon nanotube films. Materials Science and Engineering: C. 2011;31:1505-11.
[60] Bobbert F, Zadpoor A. Effects of bone substitute architecture and surface properties on cell response, angiogenesis, and structure of new bone. Journal of Materials Chemistry B. 2017.
[61] Stachewicz U, Qiao T, Rawlinson SC, Almeida FV, Li W-Q, Cattell M, et al. 3D imaging of cell interactions with electrospun PLGA nanofiber membranes for bone regeneration. Acta biomaterialia. 2015;27:88-100.
[62] Ura DP, Karbowniczek JE, Szewczyk PK, Metwally S, Kopyściański M, Stachewicz U. Cell integration with electrospun PMMA nanofibers, microfibers, ribbons, and films: a microscopy study. Bioengineering. 2019;6:41.
[63] Mattila PK, Lappalainen P. Filopodia: molecular architecture and cellular functions. Nature reviews Molecular cell biology. 2008;9:446-54.
[64] Son S-R, Linh N-TB, Yang H-M, Lee B-T. In vitro and in vivo evaluation of electrospun PCL/PMMA fibrous scaffolds for bone regeneration. Science and technology of advanced materials. 2013;14:015009.
[65] Lampin M, Warocquier-Clérout R, Legris C, Degrange M, Sigot-Luizard M. Correlation between substratum roughness and wettability, cell adhesion, and cell migration. Journal of Biomedical Materials Research: An Official Journal of The Society for Biomaterials and The Japanese Society for Biomaterials. 1997;36:99-108.
[66] Barrère F, van Blitterswijk CA, de Groot K. Bone regeneration: molecular and cellular interactions with calcium phosphate ceramics. International Journal of Nanomedicine. 2006;1:317-32.
[67] Mizuno M, Kuboki Y. Osteoblast-related gene expression of bone marrow cells during the osteoblastic differentiation induced by type I collagen. Journal of biochemistry. 2001;129:133-8.
[68] Zhou M, Geng Y-m, Li S-y, Yang X-b, Che Y-j, Pathak JL, et al. Nanocrystalline hydroxyapatite-based scaffold adsorbs and gives sustained release of osteoinductive growth factor and facilitates bone regeneration in mice ectopic model. Journal of Nanomaterials. 2019;2019.
[69] Shitole AA, Raut PW, Sharma N, Giram P, Khandwekar AP, Garnaik B. Electrospun polycaprolactone/hydroxyapatite/ZnO nanofibers as potential biomaterials for bone tissue regeneration. Journal of Materials Science: Materials in Medicine. 2019;30:51.
[70] Ramesh N, Moratti SC, Dias GJ. Hydroxyapatite–polymer biocomposites for bone regeneration: A review of current trends. Journal of Biomedical Materials Research Part B: Applied Biomaterials. 2018;106:2046-57.
[71] Geng Z, Wang X, Zhao J, Li Z, Ma L, Zhu S, et al. The synergistic effect of strontium-substituted hydroxyapatite and microRNA-21 on improving bone remodeling and osseointegration. Biomaterials science. 2018;6:2694-703.
[72] Long EG, Buluk M, Gallagher MB, Schneider JM, Brown JL. Human mesenchymal stem cell morphology, migration, and differentiation on micro and nano-textured titanium. Bioactive Materials. 2019;4:249-55.
[73] Olivares-Navarrete R, Hyzy SL, Hutton DL, Erdman CP, Wieland M, Boyan BD, et al. Direct and indirect effects of microstructured titanium substrates on the induction of mesenchymal stem cell differentiation towards the osteoblast lineage. Biomaterials. 2010;31:2728-35.

[74] Moroni L, Licht R, de Boer J, de Wijn JR, van Blitterswijk CA. Fiber diameter and texture of electrospun PEOT/PBT scaffolds influence human mesenchymal stem cell proliferation and morphology, and the release of incorporated compounds. Biomaterials. 2006;27:4911-22.
[75] Ermis M, Antmen E, Hasirci V. Micro and Nanofabrication methods to control cell-substrate interactions and cell behavior: A review from the tissue engineering perspective. Bioactive Materials. 2018;3:355-69.
[76] Banik BL, Riley TR, Platt CJ, Brown JL. Human mesenchymal stem cell morphology and migration on microtextured titanium. Frontiers in Bioengineering and Biotechnology. 2016;4:41.
[77] Yang W, Han W, He W, Li J, Wang J, Feng H, et al. Surface topography of hydroxyapatite promotes osteogenic differentiation of human bone marrow mesenchymal stem cells. Materials Science and Engineering: C. 2016;60:45-53.
[78] Li Y, Yang S-T. Effects of three-dimensional scaffolds on cell organization and tissue development. Biotechnology and Bioprocess Engineering. 2001;6:311-25.
[79] Charbord P. Bone marrow mesenchymal stem cells: historical overview and concepts. Hum Gene Ther. 2010;21:1045-56.
[80] Dosier CR, Uhrig BA, Willett NJ, Krishnan L, Li M-TA, Stevens HY, et al. Effect of cell origin and timing of delivery for stem cell-based bone tissue engineering using biologically functionalized hydrogels. Tissue Eng Part A. 2015;21:156-65.
[81] Freitas GP, Lopes HB, Almeida ALG, Abuna RPF, Gimenes R, Souza LEB, et al. Potential of Osteoblastic Cells Derived from Bone Marrow and Adipose Tissue Associated with a Polymer/Ceramic Composite to Repair Bone Tissue. Calcified tissue international. 2017;101:312-20.

Rotary jet spun polycaprolactone/hydroxyapatite and carbon nanotubes scaffolds seeded with bone marrow mesenchymal stem cells increased bone neoformation

Mirian M. Machado-Paula[1,2], Marcus A.F. Corat[3], Luana M.R. Vasconcellos[4], Juliani C.R. Araújo[4], Gujie Mi[2], Paria Ghannadian[2], Tatiane V. Toniato[1], Fernanda R. Marciano[5], Thomas J. Webster[2]* and Anderson O. Lobo[2,6]*

Supplementary file

Thermogram analysis of the fibers produced by ES and RJS had glass transition temperatures (Tg) near -60 ºC and a melting temperature (Tm) around 60 ºC for all samples. These results are similar to those already reported, indicating that the methods used did not interfere with the results **(Fig.S 1)** [1].

The degree of crystallinity degree of the material is related to the degradation of the material. Furthermore, higher crystallinity means higher strength properties. This parameter is considered an essential criterion for biomedical applications since it determines the degradation time of the implanted material [2-4]. The influence of the technique on the crystallinity (X_c) of the fibers was minimal (7, 7, 0 and 1%, respectively). A slight variance of crystallinity was observed when the nanoparticles were incorporated.

Supplementary Table. S1. Thermograms analysis for all fibers produced by electro and rotary jet spinning. Tm – melting temperature; ΔHm – melting enthalpy; Tg – glass transition temperature; Xc – degree of crystallinity. DSC was recorded between -100°C and 200°C at a scan rate of 10°C/min.

	Tm (ºC)	**ΔH_m (J g^{-1})**	**Tg (ºC)**	**X_c (%)**
Electrospinning				
PCL	61.58	68.97	- 61.11	50.71
PCL + 1%nHAp	62.18	70.38	- 59.74	51.75

PCL + 1%CNT	61.26	63.60	- 60.27	46.76
PCL + 1% nHap:CNT	61.89	62.77	- 60.48	46.25
Rotary jet spinning				
PCL	62.27	63.07	- 61.31	46.70
PCL + 1%nHAp	64.66	61.72	- 59.81	44.68
PCL + 1%CNT	64.20	65.65	- 62.10	47.46
PCL + 1% nHap:CNT	56.67	38.14	- 62.58	44.48

Fig. S1 shows the FTIR spectra collected from PCL and PCL composites produced by ES and RJS. The characteristic peaks referred to PCL were identified as: 2942, 2890 and 2862 cm^{-1} (CH_2 stretching), 1725 cm^{-1} (C=O stretching), 1238 cm^{-1} (asymmetric C-O-C stretching), 1170 cm^{-1} (O-C-O stretching), 900 – 1000 cm^{-1} (symmetric C-O-C stretching), and 577 and 729 cm^{-1} (CH_2 rocking) [5, 6]. The collected vibrational bands referred to the fibers produced from ES and RJS were the same. The low content of CNT, nHAp, and nHap:CNT did not promote significant modification in the FTIR spectra. Peaks for the nanoparticles of CNT, nHAp, and nHAp:CNT incorporated using both techniques were observed in the positions:1725, 1238, and 1170 cm^{-1}. The stretching was a consequence of an increase in the functional groups.

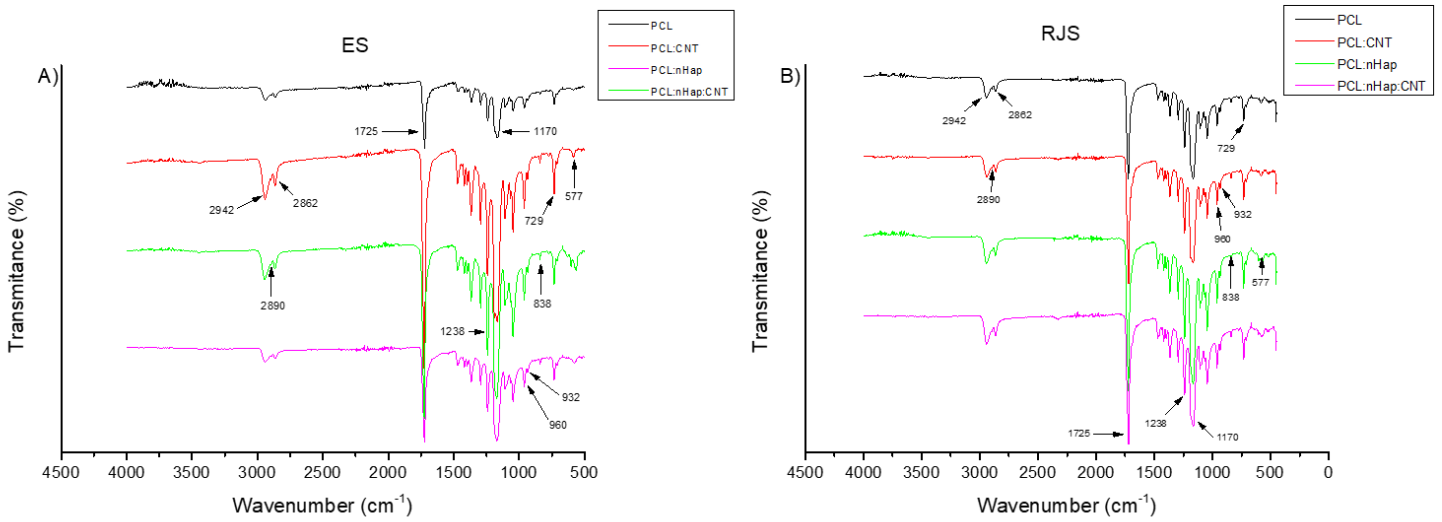

Supplementary Fig. S1. FTIR spectra of the fibers produced by (a) electrospinning and (b) rotary jet spinning.

The mechanical tensile tests showed two significantly improved properties for our materials: elastic modulus and elongation at break. A rigid and resistant material to deformation under a given load presents a high elastic modulus, while a flexible material presents a lower elastic modulus [7, 8]. Thus, the stiffest material observed was PCL:nHap:CNT synthesized by ES ($p<0.0001$), and more flexibility was shown for those with a lower elastic modulus **(Fig. S2A)**. Thus, materials produced by ES showed the most significant change in elastic modulus after incorporation of nanoparticles, mainly with nHap and nHap:CNT. Conversely, the RJS scaffolds demonstrated the smallest change in elastic modulus even after the addition of the nanoparticles. Relative to elongation at break or fracture strain, a scaffold with a higher elongation at break will be able to possess a higher resistance to deformation without cracking [9]. RJS materials demonstrated the highest elongation at break compared with ES materials ($p<0.01$), which presented considerably lower values **(Fig. S2B)**. A slight decrease in value was seen after the incorporation of nanoparticles for both of the synthesis methods.

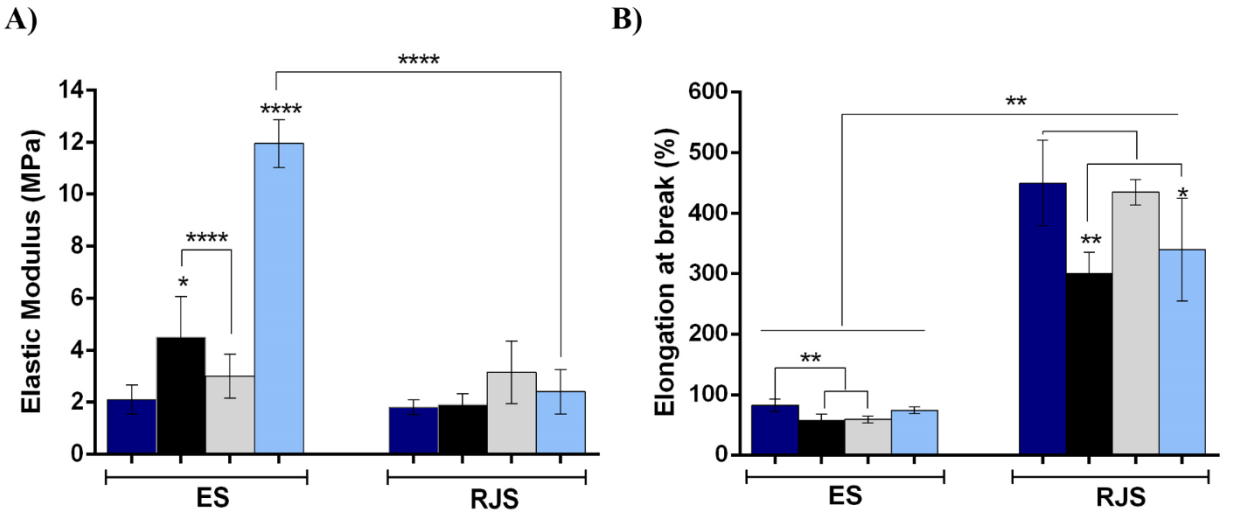

Supplementary Fig. S2. Mechanical tensile testing for all of the fibers produced. (A) Elastic modulus obtained from the dynamic mechanical analysis. (B) Elongation at break for the ES and RJS samples. Values are mean ± SD, N=3. Statistically significant (* $p < 0.05$, ** $p < 0.01$ and **** $p < 0.0001$). Asterisk alone means comparison with the neat PCL as the same method.

HOB biological activity in contact with fiber structures was performed for possible applications in bone tissue regeneration **(Fig. S3A-D)**. Cell viability results **(Fig. S3A)** demonstrated that all the polymeric scaffolds showed good biocompatibility despite being hydrophobic, confirming the potential of the produced scaffolds. Cell metabolic activity was monitored after 7, 14, and 21 days of culture **(Fig. S3B)**. All composites were compared to pure PCL fibers. A gradual increase in cell proliferation was observed, independent of the scaffolds and each technique. Comparing the techniques, the fibers by ES showed more osteoblast cell density than RJS fibers at 12 days mainly those with both nanoparticles incorporated (PCL:nHAp:CNT, $p<0.0001$). nHAp is an excellent carrier of osteoinductive growth factors [10]. Harikrishnan et al. showed the most significant proliferation of MG63 cells on the PCL-nHAp scaffolds for up to 10 days [11]. However, an

enhancement was observed for groups containing nHap:CNT compared to the other mats at 21 days.

ALP expression is associated with osteoblast differentiation. **Fig. S3C** shows the ALP activity levels after 7, 14, and 21 days. On day 14, the level of ALP increased significantly ($p<0.0001$) compared to day 7 for both techniques. The fibers containing both nanoparticles showed enzymatic activity greater to the other groups regardless of the technique, confirming the important effect of the nanoparticles on osteogenic differentiation. Comparing the PCL:nHap:CNT fabricated by both methods, the scaffolds produced by ES showed higher enzymatic activity than those by RJS ($p<0.001$). The ALP activity level at day 21 significantly decreased in all scaffolds produced, probably due to the increased synthesis of mineralization and the formation of a mineralized matrix, which is a marker for mature osteoblasts [12]. Our group demonstrated similar results where a core:shell:peptide (PCL:PEG:Gelatin:OGP) scaffold showed lower ALP activity and increased calcium deposition, an indication of the initial period of osteoblast maturation [13]. Such data are supported by quantitative assays of calcium deposition, as shown in **Fig. S3D**. Higher concentrations of calcium were showed by all scaffolds at day 14 and showed specific stability at day 21. The groups with both nanoparticles assessed high calcium deposition compared to the other groups within the same technique, showed a statistical difference of $p<0.0001$ for ES and $p<0.05$ for RJS fibers. Although fibers with nanoparticles produced by ES on day 14 showed a 2-fold more expression of ALP and 1-fold more calcium deposition than fibers from RJS, both showed high enzymatic activity and calcium deposition.

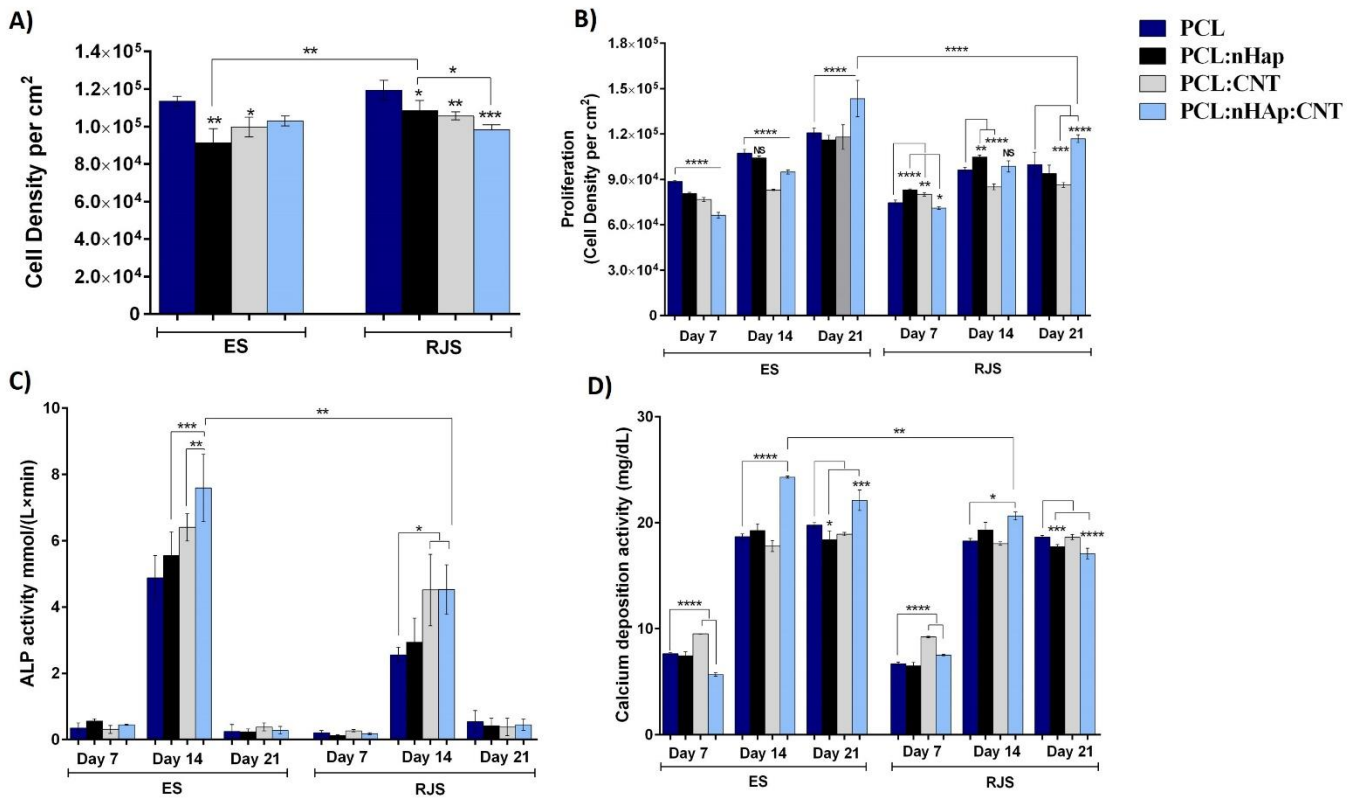

Supplementary Fig. S3. Cellular assays. **A)** Cell viability on the different fibers produced after 24 hours. **B)** Cell proliferation assay was performed after 7,14 and 21 days. **C)** Alkaline phosphatase (ALP) activity and **D)** Calcium deposition on the different fibers produced. Assays were performed after 7, 14 and 21days. Results were normalized by subtracting the absorbance values of blank wells containing samples without any cells from those values measured for the samples with cells. Values are mean ± SD, N=3. * $p< 0.05$, ** $p< 0.01$, *** $p<0.001$ and **** $p< 0.0001$. Asterisk alone means comparison with the neat PCL as the same method.

The 3D reconstruction of the rat calvaria defect (5mm) is shown in **Fig. S4A**. These images represent 3D reconstructions after 2 and 6-weeks of implantation of PCL and PCL:nHap:CNT for both methods without and with BMMSCs. Based on the reconstructed 3D image, new bone regenerated in the peripheral and central parts of the defect, and the groups with the nanoparticles

incorporated seeded with BMMSCs after 6 weeks. This observation suggested the success of combining these cells with the biomaterial to improve bone regeneration.

All parameters measured from microtomography (BV, Tb.Th, Tb.N, and Tb.Sp) are illustrated in **Fig. S4B-I**. The bone volume (BV) parameter has already been shown and discussed in the main article. The trabeculae thickness data (Tb.Th) was corroborated with the BV parameters, where the fibers containing nanoparticles by ES after 2 weeks exhibited high Tb.Th with a statistical difference ($p < 0.01$) compared with pure PCL, however, there was no significant difference ($p < 0.05$) observed between the RJS fibers **(Fig. S4D)**. In scaffolds seeded with BMMSCs **(Fig. S4E)**, the pure PCL RJS fibers showed a higher Tb.Th after 6-weeks, with a significant difference at ($p<0.05$) compared with pure PCL by ES, there was no significant difference between the fiber and nanoparticle produced using the same method.

The trabeculae number (Tb.N) was significant in the fibers with nanoparticles produced by ES compared with the same scaffold produced by RJS ($p<0.001$) **(Fig. S4F)**. In scaffolds seeded with BMMSCs **(Fig. S4G)**, the PCL:nHap:CNT in both time periods produced by the RJS method showed a more significant number of trabeculae compared with pure PCL ($p<0.01$ and $p<0.05$, respectively).

The trabeculae separation data (Tb.Sp) showed a significant difference between the groups after 2 weeks in both periods **(Fig. S4H-I)**. At 6 weeks, just the PCL:nHap:CNT by RJS showed low trabeculae separation, compared with the same material but produced by ES ($p<0.05$).

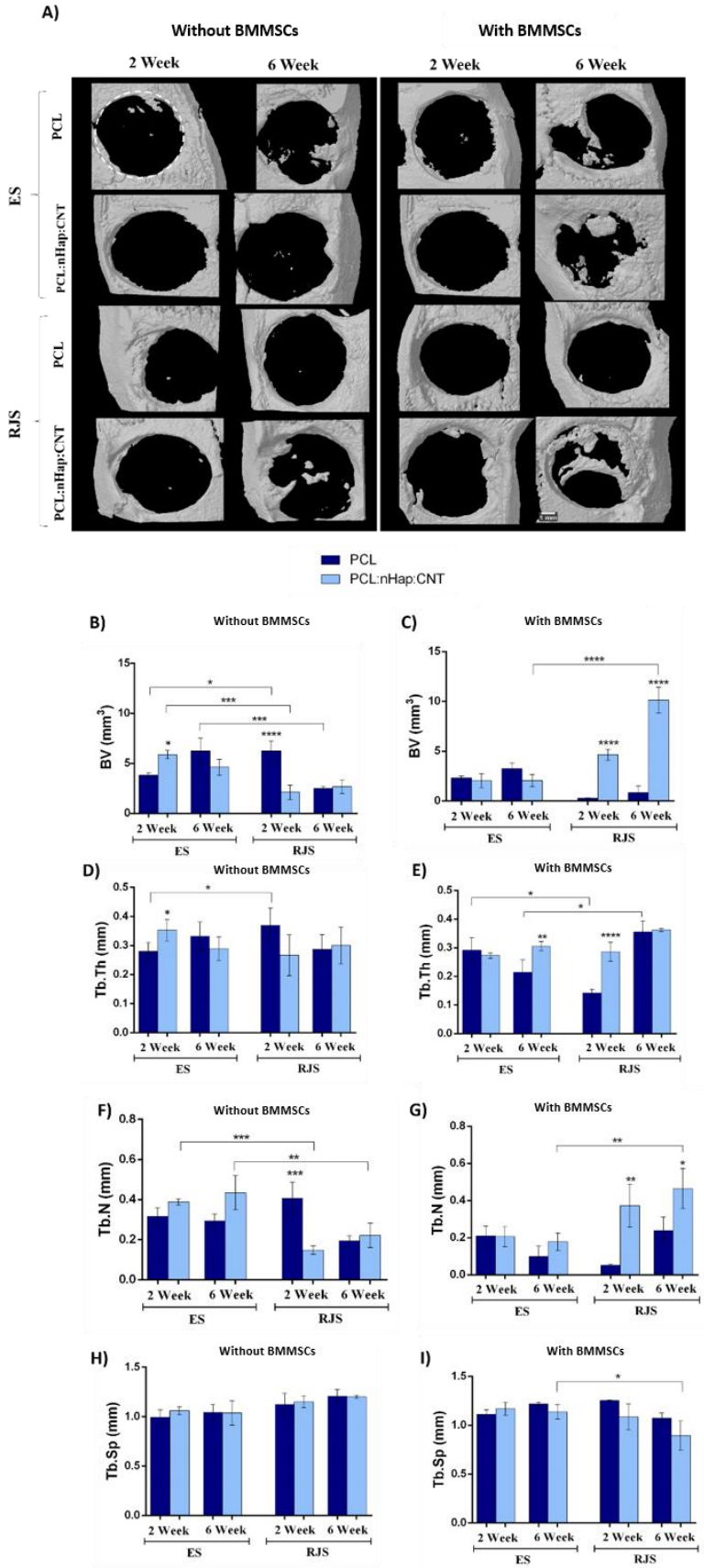
A)
Without BMMSCs
With BMMSCs
2 Week
6 Week
2 Week
6 Week
ES
RJS
PCL
PCL:nHap:CNT
PCL
PCL:nHap:CNT
PCL
PCL:nHap:CNT
B)
Without BMMSCs
C)
With BMMSCs
BV (mm³)
D)
Without BMMSCs
E)
With BMMSCs
Tb.Th (mm)
F)
Without BMMSCs
G)
With BMMSCs
Tb.N (mm)
H)
Without BMMSCs
I)
With BMMSCs
Tb.Sp (mm)
2 Week
6 Week
ES
RJS

Supplementary Fig. S4. A) Reconstructed 3D micro-CT images of rat calvaria implanted with PCL and PCL:nHap:CNT by ES and RJS after 2 and 6 weeks without or with seeded BMMSCs. The dotted circles indicate the original defect. Bar length: 1mm. **B-C)** Micro-CT assessment of bone volume (BV) in ES and RJS groups: (B) without cells and (C) with seeded BMMSCs. **D-E)** Micro-CT assessment of trabeculae thickness (Tb.Th) in ES and RJS groups: (D) without cells and (E) with seeded BMMSCs. **F-G)** Micro-CT assessment of trabeculae number (Tb.N) in ES and RJS groups: (F) without cells and (G) with seeded BMMSCs. **H-I)** Micro-CT assessment of trabeculae separation (Tb.Sp) in ES and RJS groups: (F) without cells and (G) with seeded BMMSCs. All were analyzed at two time points: 2 and 6 weeks. Statistically significant (* $p< 0.05$, ** $p< 0.01$, *** $p<0.001$ and $p<*0.0001$). Asterisk alone means comparison with the neat PCL as the same method.

The histology images are shown in **Fig. S5A-B** of the 2 and 6-week groups after implantation of PCL and PCL:nHap:CNT for both methods: (A) acellular scaffolds and (B) scaffolds seeded with BMMSCs. Active bone formation was observed in all scaffolds analyzed. Besides, bone neoformation occurred both in the peripheral and central parts of the defect, mainly in groups with incorporated nanoparticles seeded with BMMSCs. The immature bone trabeculae presented osteocytes in lacunae (arrows) and osteoblasts around the trabecular bone (dashed arrows). The defect area is composed predominantly of vascularized repair tissue.

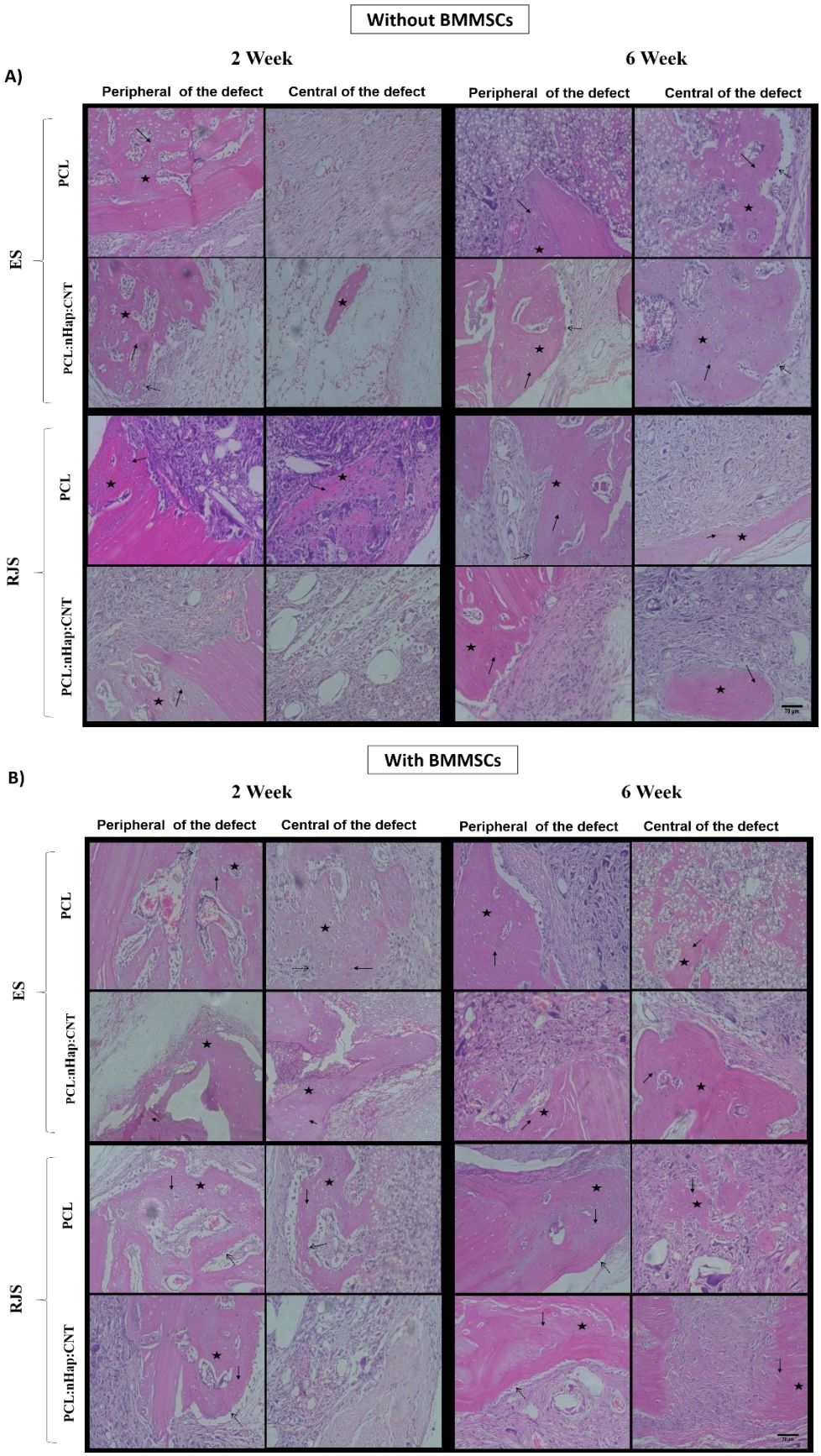
Without BMMSCs
A)
2 Week
6 Week
Peripheral of the defect
Central of the defect
Peripheral of the defect
Central of the defect
ES
PCL
PCL:nHap:CNT
RJS
PCL
PCL:nHap:CNT
With BMMSCs
B)
2 Week
6 Week
Peripheral of the defect
Central of the defect
Peripheral of the defect
Central of the defect
ES
PCL
PCL:nHap:CNT
RJS
PCL
PCL:nHap:CNT

Supplementary Fig. S5. Histological images of rat calvaria defects filled with different materials at 2 and 6 weeks. (A) Acellular scaffolds and (B) scaffolds seeded with BMMSCs. Stars mark the bone neoformation active, the arrows show the osteocytes in the lacunas, and dashed arrow mark osteoblasts around the trabecular bone. In all groups x20.0 magnification.

References

[1] Asghari F, Samiei M, Adibkia K, Akbarzadeh A, Davaran S. Biodegradable and biocompatible polymers for tissue engineering application: a review. Artificial cells, nanomedicine, and biotechnology. 2017;45:185-92.
[2] Kuzelova Kostakova E, Meszaros L, Maskova G, Blazkova L, Turcsan T, Lukas D. Crystallinity of Electrospun and Centrifugal Spun Polycaprolactone Fibers: A Comparative Study. Journal of Nanomaterials. 2017;2017.
[3] Kar KK, Pandey JK, Rana S. Handbook of Polymer Nanocomposites. Processing, Performance and Application: Volume B: Carbon Nanotube Based Polymer Composites: Springer Berlin Heidelberg; 2014.
[4] Woodruff MA, Hutmacher DW. The return of a forgotten polymer—Polycaprolactone in the 21st century. Progress in Polymer Science. 2010;35:1217-56.
[5] Lobo AO, Afewerki S, de Paula MMM, Ghannadian P, Marciano FR, Zhang YS, et al. Electrospun nanofiber blend with improved mechanical and biological performance. International journal of nanomedicine. 2018;13:7891.
[6] Yeh JT, Yang MC, Wu CJ, Wu CS. Preparation and characterization of biodegradable polycaprolactone/multiwalled carbon nanotubes nanocomposites. Journal of applied polymer science. 2009;112:660-8.
[7] Huebsch N, Lippens E, Lee K, Mehta M, Koshy ST, Darnell MC, et al. Matrix elasticity of void-forming hydrogels controls transplanted-stem-cell-mediated bone formation. Nature materials. 2015;14:1269.
[8] Ghannadian P, Moxley JW, Machado de Paula MM, Lobo AO, Webster TJ. Micro-Nanofibrillar Polycaprolactone Scaffolds as Translatable Osteoconductive Grafts for the Treatment of Musculoskeletal Defects without Infection. ACS Applied Bio Materials. 2018;1:1566-78.
[9] Petroudy SD. Physical and mechanical properties of natural fibers. Advanced High Strength Natural Fibre Composites in Construction: Elsevier; 2017. p. 59-83.
[10] Zhou M, Geng Y-m, Li S-y, Yang X-b, Che Y-j, Pathak JL, et al. Nanocrystalline hydroxyapatite-based scaffold adsorbs and gives sustained release of osteoinductive growth factor and facilitates bone regeneration in mice ectopic model. Journal of Nanomaterials. 2019;2019.
[11] Harikrishnan P, Islam H, Sivasamy A. Biocompatibility Studies of Nanoengineered Polycaprolactone and Nanohydroxyapatite Scaffold for Craniomaxillofacial Bone Regeneration. Journal of Craniofacial Surgery. 2019;30:265-9.
[12] Shao W, He J, Sang F, Ding B, Chen L, Cui S, et al. Coaxial electrospun aligned tussah silk fibroin nanostructured fiber scaffolds embedded with hydroxyapatite–tussah silk fibroin nanoparticles for bone tissue engineering. Materials Science and Engineering: C. 2016;58:342-51.
[13] De-Paula MMM, Afewerki S, Viana BC, Webster TJ, Lobo AO, Marciano FR. Dual effective core-shell electrospun scaffolds: Promoting osteoblast maturation and reducing bacteria activity. Materials Science and Engineering: C. 2019;103:109778.